An Investigation on Design and Analysis of Micro-Structured Surfaces with Application to Friction Reduction

A thesis submitted for the degree of Doctor of Philosophy

by

Samira Sayad Saravi

School of Engineering and Design, Brunel University

February 2014

Abstract

Drag reduction in wall-bounded flows can be achieved by the passive flow control technique using riblets and surface grooves aligned in the mean direction of an overlying turbulent flow. They were inspired by the skin of fast sharks covered with small longitudinal ribs on their skin surfaces. Although it was found that the drag reduction depends on the riblets' geometrical characteristics, their physical mechanisms have not yet been fully understood in the scientific terms.

Regarding riblets sizing, it has been critically explained in the literature how riblets with vanishing size interact with the turbulent flow and produce a change in the drag proportional to their size. Their shapes are focused upon because these are most significant from a technological perspective, and also less well understood. Different riblet shapes have been designed, some with complicated geometries, but except for the simple ones, such as U and V grooves, there has not been enough study regarding shape features. Therefore, special effort is undertaken to the design of an innovative type of ribleted surface, e.g. the Serrate-Semi-Circular shape, and its effect on the skin friction and drag reduction.

In this work, the possible physical mechanisms of riblets for turbulent drag reduction have been explored. The modelling and experiments concerning the relationship between the riblets features and the turbulent boundary layer structure have also been reviewed.

Moreover, numerical simulations on riblets with different shapes and sizes are presented and studied in detail. An accurate treatment based on k-ε turbulence model was adopted to investigate the flow alteration and the consequent drag reduction on ribleted surfaces. The interaction of the overlying turbulent flow with riblets and its impact on their drag reduction properties are further investigated. In addition, the experimental facilities, instrumentation (e.g. hotwires) and measurement techniques (e.g. time-averaged turbulence structure) have been employed to experimentally investigate the boundary layer velocity profiles and skin friction for smooth and micro-structured surfaces (the proposed riblet shape),

respectively and the presented new design of riblets with serration inside provides 7% drag reduction. The results do not show significant reduction in momentum transfer near the surface by riblets, in particular, around the outer region of the turbulent boundary layer.

Conclusions with respect to the holistic investigation on the drag reduction with Serrate-Semi-Circular riblets have been drawn based on the research objectives as achieved. Recommendations for future work have been put forward particularly for further future research in the research area.

Acknowledgements

First and foremost I would like to take this opportunity to express my gratitude to my supervisor, Professor Kai Cheng, for his enthusiastic scientific support, insightful guidance, and patience throughout the course of this research.

I would like to thank Brunel University and KIMM (Korea Institute of Machinery and Materials) for their financial support which made this research possible. Project partners including NPL (National Physics Laboratory), as well as Contour Fine Tooling Ltd, have also to be acknowledged for their support, assistance and constructive suggestions in this research project.

I thank the project consortium for providing me the opportunity to carry out this work and the many individuals who organised it. In particular, Dr Tze Pei Chong my second supervisor, Alexander Vathylakis, Paul Yates, Pieter Walsh, Fred Bryant, Seyed Hossein Madani, FeiFei Jiao, Dr Alireza Mousavi, Professor Richard Leach, Dr Jan Wissink, Dr Reza Mokhtarzdeh, Linda Hartley, Michael Low, Dr Benjamin Mckley, Andrew Cox and Dr Li.

Despite the hardship moments of I have been fortunate to have had around many individuals that helped in so many different ways in the process and to whom I am greatly indebted. Thank you to Rashidi, Mohammad Haron Kheir, Raphael, Tao Wu, Abdolreza Naji, Soheil, Fahimeh Nezhadi and Mahshid Yazdifar in particular.

Special thanks go to Saba Eshraghi and Asieh Bavarsad abdali for their invaluable support. Their friendship and encouragement have been a strong wind that helped leading this boat safely to the harbour.

Finally, a big thank you to my family: my parents, sister, brother and brother in law, for their support and love, especially to my parents whose strength and determination have always been a model for me.

Table of Contents

Abbreviation

AOA	Angle Of Attack
APG	Adverse Pressure Gradient
BL	Boundary Layer
CFD	Computational Fluid Dynamics
CVD	Chemical Vapour Deposition
DNS	Direct Numerical Simulation
DR	Drag Reduction
FFT	Fast Fourier Transform
FP	Flat Plate
HW	Single Hot-Wire
IB	Immersed Boundary
K-H	Kelvin-Helmholtz instability waves
LE	Leading Edge
LEBU	Large Eddy Breakup Devices
LES	Large Eddy Simulation
MIC	Microphone
PIV	Particle Image Velocimetry
PSD	Power Spectral Density
Q	Quasi
QSE	Quadratic Stochastic Estimation
QSWV	Quasi-Span-Wise-Vorticity
RANS	Reynolds-Averaged Navier Stokes
Re	Reynolds Number
RIB	Riblets
TBL	Turbulent Boundary Layer
TE	Trailing Edge
T-S	Tollmien-Schlichting instability waves
VS	Vortex Shedding
XW	Cross-Wire

Nomenclature

A	Inlet area [mm^2]
A_g	Riblets cross section [mm^2]
A_g^+	Dimensionless riblets cross section
$a_1 - a_{10}$	Cross hot wire calibration coefficients
$b_1 - b_{10}$	Cross hot wire calibration coefficients
$C_1, C_2, C_{3,}, C_4, C_5$	Single hot wire calibration coefficients
$C_{1\varepsilon}, C_{2\varepsilon}, C_\mu$	Constants in k - e Model
C_f	Skin friction coefficient, $C_f = \frac{\tau_w}{1/2\rho U_e^2}$
h^+	Dimensionless riblets height: $h^+ = hu_\tau/v$, u_τ is friction velocity
h, h_1, h_2	Riblets height [mm]
H_{12}	Shape factor, $H_{12} = \delta_1/\delta_2$
K	Turbulent kinetic energy [m^2/s^2]
k_{eq}	Sand grain roughness height
k_{eq}^+	Dimensionless sand grain roughness, $k_{eq}^+ = U_\tau k_{eq}/\nu$
L_x, L_y, L_z	Computational domain
L	Turbulence length scale
L_g^+	Dimensionless root mean square of riblets cross section, $A_g^{+1/2}$
M	Mach number, $M = U_\infty/c$
M	Mass flow, $M = \rho AV$
M_c	Mach number based on convection velocity, $M_c = U_c/c$
P	Static pressure [Pa]
P_{tot}	Total pressure [Pa]
p′	Fluctuating surface pressure [Pa]
< p′ >	Conditionally-averaged mean-removed surface

Nomenclature

	pressure [Pa]
p'_{rms}, p_{rms}	Root mean square of pressure fluctuations [Pa]
Re	Reynolds number, $Re = \rho u D/\mu$
Re_τ	Friction Reynolds number, $Re_\tau = \delta^+$
s^+	Dimensionless riblets spacing: $s^+ = su_\tau/v$, u_τ is friction velocity
s, s_1, s_2	Riblets spacing [mm]
t	Time [s]
U_{99}	The velocity at the position of the boundary layer thickness, $U_{99} = 0.99U_\infty$[m/s]
U_c	Convection velocity [m/s]
U_e	Velocity at the edge of the boundary layer [m/s]
U_∞ or U_o	Freestream velocity [m/s]
U_τ, u_τ	Friction velocity [m/s]
-u′v′	Reynolds shear stress [$(m/s)^2$]
V, U or u	Velocities [m/s]
$\tilde{V}, \tilde{U}$	Ensemble-averaged velocity perturbations [m/s]
v_{rms}, u_{rms}	Ensemble-averaged rms velocity fluctuations [m/s]
x,y,z	Cartesian Coordinate [mm]
x^+, y^+, z^+	Dimensionless Coordinate
α	Airfoil angle of attack and angle between the flow direction and each cross-wire element used for the XW calibration [deg.]
α_1, α_2	Angle of each wire element with the horizontal [deg.]
δ or δ_{99}	Boundary layer thickness [mm]
δ_1	Boundary layer displacement thickness [mm]
δ_2	Boundary layer momentum thickness [mm]
ε	Dissipation of turbulent kinetic energy
σ_ε	Constant in k - e model (turbulent Prandtl numbers for ε)
σ_k	Constant in k - e model (turbulent Prandtl numbers

	for k)
γ	Wall pressure normalised cross-spectra [Pa]
$\gamma^2(G_{p_i p_j})$	Wall pressure coherence
μ	Dynamic viscosity [kg/ms]
ν	Kinematic viscosity [m^2/s]
$\emptyset$	Phase angle between the signals of two surface pressure sensors or microphones in this case [rad]
$\emptyset_{uu}$	Velocity spectra, $u'^2 = \int_0^\infty \emptyset_{uu} df$, [$(m/s)^2$/Hz]
$\emptyset_{ii}$	Pressure spectrum [$(m/s)^2$/Hz]
$\Phi_{p_i p_j}$	Cross-spectra between surface pressure fluctuations from microphones p_i and p_j [Pa^2/HZ]
$\Phi_{p_i p_i}$	Surface pressure autospectra or power spectral density from microphone p_i [Pa^2/HZ]
$\Phi, \Phi(w), \Phi(f)$	Surface pressure power spectral density [pa^2/HZ]
ρ	Density [kg/m^3]
τ	Time delay [ms]
τ_w	Wall shear stress [Pa]

List of Figures

List of Tables

List of Tables

Chapter 1

Introduction

1.1 Research Background

The role of surface topographic μ-features in improving performance is a matter of research that has grown significantly since μ-manufacturing technologies have been developed. It has been known that the functional performance of tools, work-pieces, solar cells, implants, prosthesis and components for many industrial sectors can vary depending on what surface features are present or dominate. It has been identified that controlled porosity on a tribological surface can contribute to friction reduction at sliding contact interfaces. For example, one of the effects of surface texturing under boundary lubrication conditions is that μ-dimples can act as fluid reservoirs and play a role in promoting the retention of a lubrication of thin film (Appendix A). The identified applications of micro-structures functional surfaces, as shown in Figure 1.1, for instance, include:

- Aerospace: micro-structured surfaces on wings and foils.
- Moulds: less friction and wear, tool life increased.
- Automotive: injector for reduced energy consumption, increasing safety and comfort.
- Energy: increasing efficiency of solar cells and fuel cells.
- Household: haptic effects, anti-dirtiness and the lotus-effect.
- Medical sector: enhancing prosthesis and dental implants as well as tissue, bone and cell growing.
- Optics: less reflectivity and filtering of UV rays.

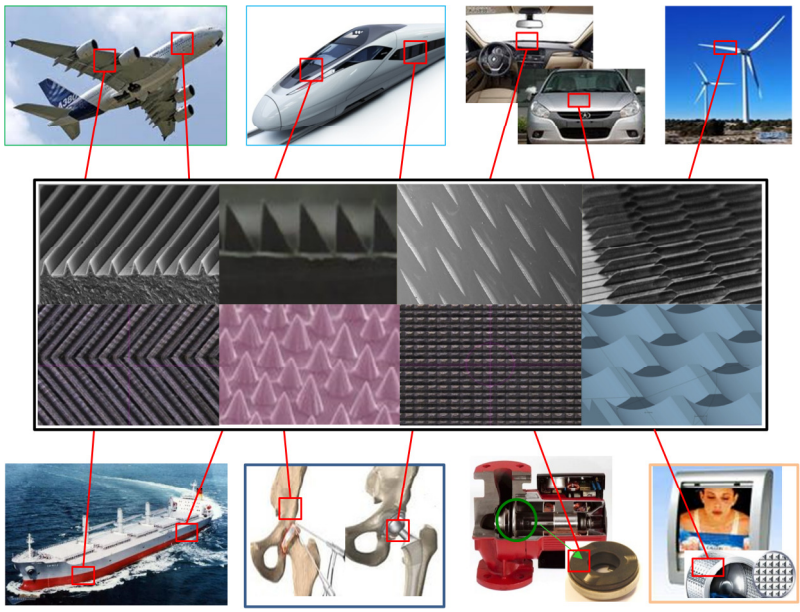

Figure 1.1: Typical applications of µ-textured and structured functional surfaces

In recent years, turbulent boundary layer drag reduction has become an important area of fluid dynamics research. Specifically, rising fuel costs have greatly emphasized the usefulness and necessity of developing efficient viscous drag reduction methods. Therefore, this study explores the concepts for control of turbulent boundary layers leading to skin friction reduction by micro-structured surfaces.

1.2 Turbulent flow structure

Most flows which occur in the practical applications of Fluid Mechanics are turbulent. This term denotes a motion which is unsteady (even if the mean flow is steady), three-dimensional (even if the mean flow is only two-dimensional), rotational, strongly diffusive, dissipative and highly irregular in space and time. Although the details of the fluctuating motion superimposed on the turbulence main motion are highly complex, the resulting mixing motion is of great importance for the course of the flow and for the balance of the forces.

The fluid elements which carry out fluctuations both in the direction of main flow and at right angles to this direction are not individual molecules, as assumed in kinematic gas theory, but rather are macroscopic eddies. At high Reynolds numbers, energy constantly flows from the basic flow to the large eddies, which

are associated with low frequency fluctuations and are responsible for most of the momentum transport. On the other hand, the dissipation of the energy mainly takes place in the small eddies, in the boundary layer near the wall. The flow within the boundary layer becomes turbulent when the local Reynolds number becomes sufficiently large. The simplest case of a turbulent boundary layer occurs on a flat plate at zero angle of incidence referred to as a canonical zero-pressure turbulent gradient. This type of motion is a practical matter for the friction drag encountered by industrial and environmental flow applications (i.e. ships and airplanes, and the losses in turbines and turbo-compressors) (Prandtl, 1954; White, 1974).

The essential feature of the structure of a turbulent boundary layer as presented by Head and Bandyopadhyay (1981), is the existence of a large number of vortex pairs, or hairpin vortices, which appear to be inclined at a more or less constant characteristic angle to the surface. These vortex pairs may be (and very often are) greatly distorted, and at high Reynolds numbers may be enormously elongated. The cross-stream dimensions of these hairpins approximately scale with the wall variables u_τ and ν, while their length appears to be limited only by the thickness of the layer (Schlichting and Gersten, 2000). Figure 1.2 demonstrates a schematic showing the growth of a two-dimensional turbulent boundary layer on a smooth flat plate. The boundary layer thickness $\delta(x)$ (where x is the stream-wise coordinate) is considered to be the location above the surface at which the local mean velocity is 99% of the free-stream value, U_e. There are two other relevant length scales apart from the boundary layer thickness, the displacement thickness, δ_1, and momentum thickness, δ_2:

$$\delta_1 U_e = \int_{y=0}^{\infty} (U_e - u)dy \tag{1.1}$$

$$\delta_2 U_e^2 = \int_{y=0}^{\infty} u(U_e - u)dy \tag{1.2}$$

The displacement thickness is the distance by which the wall would have to be displaced outwards in a hypothetical frictionless flow so as to maintain the same mass flux as in the actual flow, whereas the momentum thickness is related to the momentum loss due to the skin friction drag.

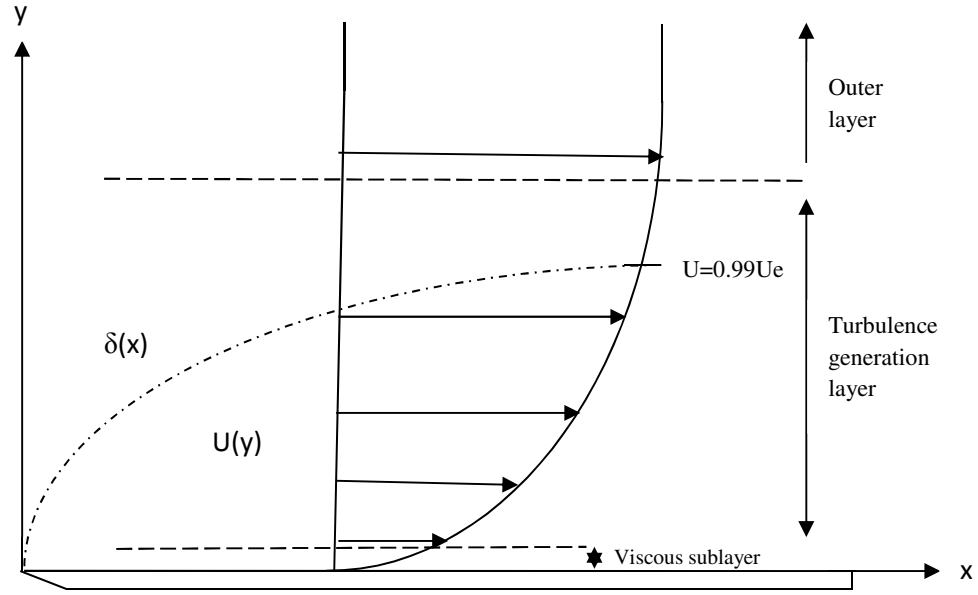

Figure 1.2: Turbulence Boundary Layer

The mean velocity profiles for a fully turbulent flow are usually termed as the "Law of Wall". The boundary layer can be basically partitioned into three layers. "Viscous sub-layer" being defined in $y^+ < 5$, where the viscosity dominates and as a result the flow is almost laminar. In this layer, the normalized velocity, u^+ is proportional to the distance from the wall in terms of the "wall units", $u+ = y+$. However, the structure of the boundary layer can be divided in terms of both wall units and the turbulent boundary layer thickness (δ), the "outer layer" and "inner layer" (Townsend, 1956). In the inner layer ($y/\delta < 0.1$), the flow is presumed to depend only on the wall shear,τ_w, the fluid properties, ρ and μ , and the distance from the wall, y. The "inner scaling" defines velocity and length as follows:

$$u^+ = \frac{u}{u_\tau} \tag{1.3}$$

$$y^+ = \frac{y}{\delta_v} = \frac{yu_\tau}{v} = \eta Re_\tau \tag{1.4}$$

$$u_\tau = \sqrt{\frac{\tau_w}{\rho}} \tag{1.5}$$

The viscosity and turbulent momentum play equally significant roles in the second layer called the “buffer layer”, which is $5< y^+ < 30$. In the region $y^+ > 30$, called the “outer layer” or “log-layer”, momentum plays a dominant role and the normalized mean velocity has a log relation with the distances.

$$u^+ = \frac{1}{k}\ln(y^+) + B \tag{1.6}$$

The log law has proven very effective as a universal curve for the inner region of the flat plate turbulent boundary layer and only recently have doubts begun to arise about its validity. What is in question is whether the log law is really Reynolds number independent, and whether a power law with Reynolds number dependence would be more correct.

In addition, turbulence dependency on the Reynolds Number has been discussed by Gad-el-Hak and Bandyopadhyay (1994), who reported that the peak production of turbulent kinetic energy occurs at $y^+ \approx 15$, independent of the Reynolds number and they concluded that this number has an effect on the turbulent shear stress even in the inner layer.

1.3 Turbulent drag reduction techniques

Flow control is classified in two categories: active and passive. Active control essentially requires the addition of energy and/or the presence of feedback, for example, for the use of compliant walls and active wave control of boundary layer transition, boundary layer suction or wall heating to delay transition, modification of the fluid viscosity by injection of polymers and for changing the fluid temperature. Passive control is self-regulatory without needing additional energy, and includes for example: modification of outer flow structures with devices such as "Large Eddy Breakup Devices" (LEBUs) and natural laminar flow control (pressure-gradient/wall shaping). One of the discovered techniques is the shear stress reduction method involving the use of "riblets". That is, understanding the drag mechanisms requires the knowledge of flow drag generation and its interaction with the surface roughness.

The most basic forms of fluid drag are pressure or form drag and friction or viscous drag. Pressure drag is associated with the energy required to move fluid out from in front of an object in the flow, and then back in place behind the object. Creating streamlined shapes can reduce the magnitude of this drag. Friction drag is created by the interactions between the fluid and a surface, as well as the attraction between the molecules of the fluid. The early experiments by Prandtle (1954) produced observable decreases in the shear stress at the wall.

Experimental results as well as more recent numerical studies suggest that there are two important activities for near-wall turbulence in the boundary layer, called the sweeps and ejections in which 80% of the turbulence energy is produced (Lu and Willmarth, 1973) (Figure 2.1). The ejections are associated with events accompanying the negative u-component velocity and the positive v-component velocity; the sweeps are turbulence events associated with the positive u-component velocity and the negative v-component velocity. The sweep events are particularly important for drag reduction, because they are responsible for the generation of turbulent wall-shear stress (Karniadakis and Choi, 2012). Ejection of vortices out of the viscous sub-layer, and chaotic flow in the outer layers of the turbulent boundary layer flow are all forms of momentum transfer and are large factors in fluid drag. Schoppa and Hussain (2002) studied the close association between vortex formation and streak instability. They elicited that vortex generation does not involve stream-wise vorticity generation at the wall by the no-slip condition or the vorticity roll-up, but instead, stretching of near-wall stream-wise vorticity sheets leads to stream-wise vortex collapse. In the following, first surface roughness is described, and subsequently the effects of riblets on vorticity and drag reduction are discussed.

The wall surface conditions, such as surface roughness, play an important role in influencing the characteristics of turbulence structure in the near-wall region of the flow. According to Perry et al. (1969), roughness elements, depending on the flow characteristics, can be subdivided into k-type and d-type. For instance, when the cavities between the roughness elements are narrow, and the roughness shift

depends on an outer scale (e.g. pipe diameter), it is called d-type, while for a k-type flow the roughness shift depends on the roughness height.

Based on the physical geometry of the wall, experimental evidence has shown that three flow regimes exist for turbulent flow over rough surfaces, (hydraulically smooth, transitionally rough and fully rough flows), primarily depending on the size of the roughness elements relative to the viscous sub-layer (Akinlade, 2005). Following Schlichting (1968), Nikuradse (1932) showed that, for k-type roughness, the equivalent sand grain roughness Reynolds number $k_{eq}^{+} = U_{\tau}k_{eq}/\nu$ (where U_{τ} is the friction velocity, $k_{eq}$is the equivalent sand grain roughness height, and ν is the kinematic viscosity) can be used as an indicator of the rough wall turbulence regime as follows: hydraulically smooth wall for $0 < k_{eq}^{+} \leq 5$, transitionally rough regime for $5 < k_{eq}^{+} < 70$, and completely rough regime for $k_{eq}^{+} \geq 70$. The scaling of the surface has been studied by many researchers (George and Castillo, 1997; Seo et al., 2004; Tachie et al., 2003; Antonia and Krogstad, 2001; DeGraaff and Eaton, 2000). Regarding which, the use of the friction velocity, U_{τ} as the scaling parameter for assessing the effect of surface roughness on the mean velocity and turbulence fields is often adopted in the literature. Ribleted surfaces, which are used for drag reduction, can be considered as transitionally rough (Tani, 1988) (Figure 1.3).

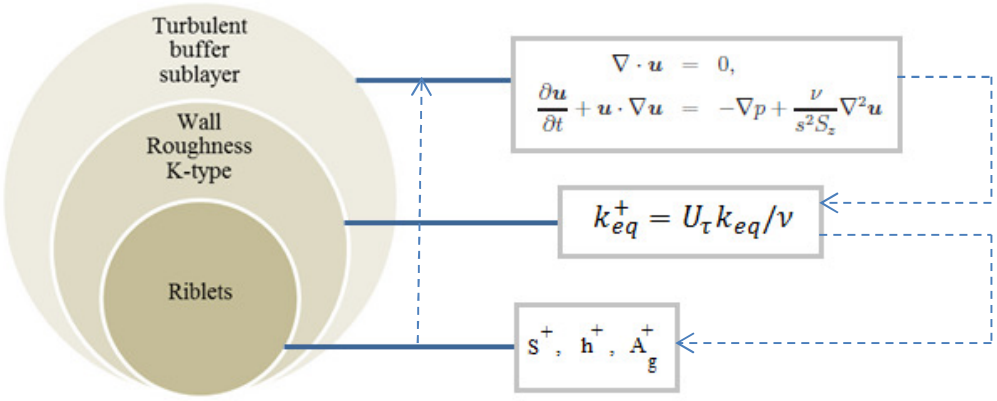

Figure 1.3: Riblets present the transitional roughness located in transition sub-layer of turbulent flow

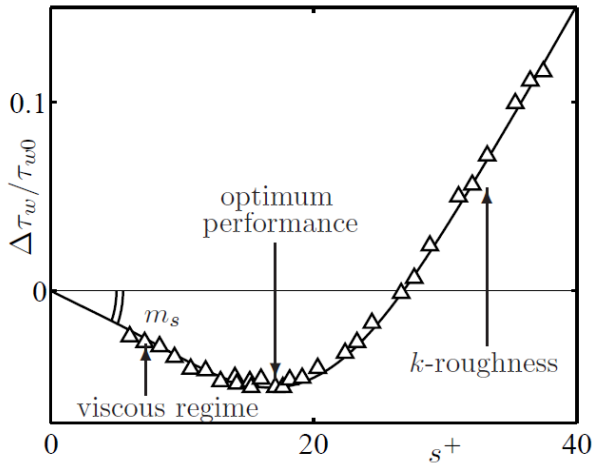

Figure 1.4: Effect of the peak-to-peak distance (S^+) on the skin friction of a triangular riblet with 60^0 peak sharpness (Bechert et al., 1997)

Riblets as a passive method reduce drag approximately 6-8% in turbulent flow. The small riblets that cover the skin of fast swimming sharks work by decreasing the total shear stress across the surface and by impeding the cross-stream translation of the stream-wise vortices in the viscous sub-layer. In the turbulent flow regime, fluid drag typically increases dramatically with an increase in surface area due to the shear stresses at the surface acting across the new, larger surface area. However, as vortices form above a riblet surface, they remain above the riblets, interacting with the tips only and rarely causing any high-velocity flow in their valleys. Since the higher velocity vortices interact only with a small surface area at the riblet tips, only this localized area experiences high shear stresses. Moreover, the low velocity fluid flow in their valleys produces very low shear stresses across the majority of the surface of the riblet. By keeping the vortices above their tips, the cross-stream velocity fluctuations inside the valleys are much lower than the cross-stream velocity fluctuations above a flat plate (Lee and Lee, 2001). This difference in cross-stream velocity fluctuations is evidence of a reduction in shear stress and momentum transfer near the surface, which minimizes the effect of the increased surface area. Although the vortices remain above the riblet tips, some secondary vortex formations do occur that enter their valleys transiently and the flow velocities of these transient secondary vortices are such that the increase in shear stress caused by their interaction with the surface of the riblet valleys is small (Dean, 2011).

Protruding into the flow without greatly increasing fluid drag allows the riblets to interact with the vortices so as to reduce the cross-stream translation and related effects. As the riblets protrude into the flow field, they raise the effective flow origin by some distance and the amount by which the height of the riblets is greater than the apparent vertical shift of the flow origin is referred to as the effective protrusion height (Figure 1.4). By calculating the average stream-wise velocity in laminar flow at heights over the riblet surfaces and comparing them to the average stream-wise velocities in laminar flow at heights over a flat plate, the effective stream-wise protrusion height is found for laminar flow. The effective cross-stream protrusion height is similarly found for this type of flow by comparing the cross-stream velocities over a riblet surface with those over a flat plate. The difference between the vertical shifts in the stream-wise and cross-stream origin, for any riblet geometry has been proposed to be the degree to which that this will reduce vortex translation for low Re flows (Bechert et al., 1997). As Re increases, the degree to which increased surface area affects the overall fluid drag increases, and the drag reduction correlation to these laminar flow theories deteriorates.

The second mechanism of drag reduction which riblets are known to provide is a reduction in non-stream-wise momentum transfer. Although the underlying mechanisms are not completely understood, the riblets which protrude into the flow cause an increase in cross-flow shear stress (Bechert et al., 1997). This in turn causes a reduction in cross-flow vortex translation, which decreases vortex interaction, ejection, and outer layer turbulence. The momentum carried in ejection vortices and transferred in non-stream-wise directions is purely wasteful to the efficiency of the flow, and by reducing the translation and ejection of vortices on the surface, large gains in energy efficiency can be made. More discussion about riblets drag reduction mechanisms is presented in the next chapter.

Based on this evidence, the focus in this study is on controlling locally individual stream-wise vortices using sophisticated, but often rather complex riblets' and textures' geometry control strategies (e.g. shapes, sizes, density and configuration).

1.4 Motivation for rough wall turbulence research

Non-random-roughness technologies have been used in diverse engineering and industrial applications. In many of these (e.g. heat exchangers, turbine blades, ship and submarine hulls, high performance aircraft, and piping systems) surface roughness can significantly affect the skin friction and heat transfer characteristics (Hosni et al., 1993). For instance, experimental application of a scratching technique to the inside surface of pipes has created a riblet-like roughness that has provided more than 5% drag reduction benefit (Weiss, 1997). Usually, a large portion of the total drag on long objects with relatively flat sides comes from turbulence at the wall, so riblets can have an appreciable effect.

In addition, understanding the extent of the roughness effect arising from a variety of textured types would improve predictive capabilities for drag reduction. Close to the wall itself, the effects of the featured surface on the velocity field depend on the specific geometry of the roughness elements. Therefore, this study concentrates on transverse modifications of the flow that can be accomplished by geometry (e.g. riblets and micro-structure).

Also, a review of the literature on controlling near-wall turbulence by riblets demonstrates that the reason why these give only about 10% reduction in skin friction is due to their inefficient interaction with QSWV (Quasi-Span-Wise-Vorticity). Therefore, the key to decreasing skin friction is to prohibit them from approaching the wall. To reach this aim, surface texturing may be a solution as a passive method due to its variety in terms of sizes and shapes (Pollard, 1998). In addition, some researchers have tried to simulate the flow over three-dimensional riblets experimentally in order to understand why their structure leads to the reduction of viscous drag in turbulent flow. However, the difficulty of such research has become clear due to the variety of variables and the complexity of the accompanying three-dimensional flow. Consequently, most of the CFD research is performed on a two-dimensional representation of the riblets, thereby decreasing the complexity of the problem. However, because unlike riblets, textures are three dimensional, the need for three dimensional modelling arises.

In recent years, CFD based complex closures (i.e. K-ε) allow for significant progress towards predicting near-wall turbulent flows, especially for engineering applications. However, the present capability for direct numerical simulation of textured wall flows is substantially deficient for high Reynolds number applications. Even the application of DNS to two-dimensional ribleted wall turbulence research has been minimal, which could be because of the complexity and computational burden arising from the roughness geometry and this issue provokes the mesh generation complication.

1.5 Aim and objectives of the research

The aim of this research is twofold: firstly, to re-examine the riblets shapes and sizes, in order to reduce skin friction for a turbulent boundary layer; and secondly, to generate a computational method for studying three-dimensionally structured surfaces better. The overarching goal is to improve the drag reduction techniques by investigating the different surfaces. The distinct objectives of this research are:

- To design a new micro-structured surface, based on the integration of existing methods in order to study changes on turbulent boundary layer and to apply and assess its suitability for manufacture.

- To develop CFD-based simulations on micro-structured/-featured surfaces to calculate, via RANS, turbulent channel flows for ribleted walls (the study aims to compute the effects of riblets' shapes and sizes on wall shear stress and the prediction of flow fields.).

- To assess and investigate the functional effect of the smooth and ribleted surfaces through well-designed experimental trials (using wind-tunnel, tribo-meter equipment and profile fitting techniques etc). Different parameters, such as the friction velocity and free-stream velocity, are used to assess the surface roughness effects on both the mean velocity and turbulence fields.

- To undertake further analysis and optimization of the modelling and simulation on selected industrial application cases.

It is hoped therefore, that the modelling as well as the flow field data thus generated and the analysis of them, collectively, will provide further improved scientific understanding of the skin friction and wall shear stress mechanisms for drag reduction applications.

1.6 Organization of the thesis

In addition to this introduction chapter, the present thesis contains another six more as shown in Figure 1.5. A review of the literature concerning this study is provided in Chapter 2 which there first being a general introduction to the theoretical models and computational flow modelling, that is followed by consideration of experimental measurement techniques. A further review of the previous research relevant to the current investigation is included in the results chapters, Chapters 5 and 6.

Numerical results of mean velocity profiles on smooth and designed ribleted walls using near-wall turbulence models are presented in Chapter 3. That is, this chapter includes fully turbulent simulations for different riblet sizes and shapes (new proposed design) covering drag reducing regimes and the overlying turbulent flow.

In Chapter 4, the experimental facilities, instrumentation and measurement techniques employed have been summarised. Whilst, in Chapter 5, the boundary layer velocity profiles (mean velocity, rms and friction velocity) and skin friction for smooth and micro-structured surface (the proposed riblet shape) are discussed. In addition, velocity spectra are analysed.

More specifically, this chapter provides a complete study of mean velocity profiles, root-mean-square (rms) velocity profiles and integral parameters by single hot wire. Furthermore in Chapter 6, the wall pressure spectra and the coherence functions (which are related to the span-wise correlation length) on flat plate (which is considered as smooth surface) and riblets plate are investigated by cross-wire and microphones.

The final chapter contains a summary and the main conclusion. In addition, the novel contributions of this thesis to the understanding of the physics of riblet bounded turbulent flows contained in Chapters 3, 5 and 6 have been published in Euspen (2013) and ESJ (2013).

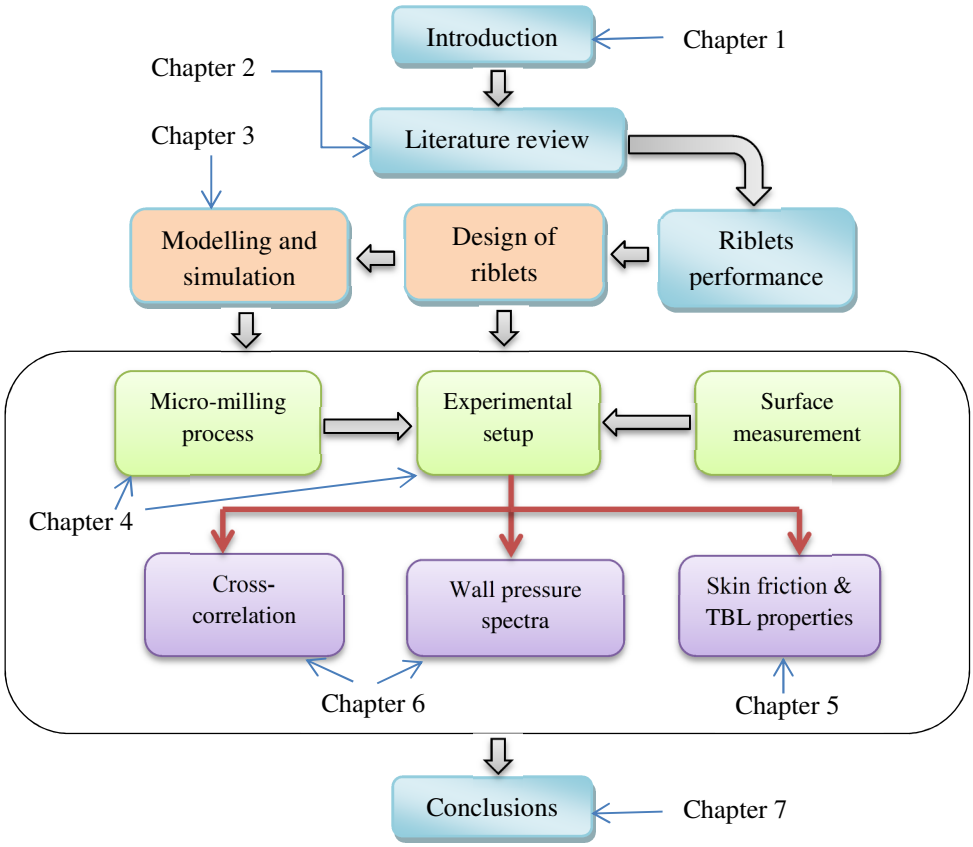

Figure 1.5: Chapter plan of the thesis

Chapter 2

Literature review

2.1 Introduction

In this chapter, a review of the previous research of concern to the current study has been summarised. In the first sections, a discussion about theoretical models associated with turbulent boundary layers has also been presented. In particular, focus has been placed on the Navier-Stokes and numerical method. The modelling and experiments concerning the relationship between the riblets features and the turbulent boundary layer structure has also been reviewed. Furthermore, the characteristics of the skin friction correlation have also been reviewed and a special emphasis has been placed on the turbulence boundary layer scaling. Note that the literature review of some of the sections, especially section 2.3, has only been outlined here since it has been included in the results chapters. It was judged more appropriate to do it in this way when the information from the literature was needed to support the results. In an effort to narrow the field, only statistics relevant for a comparison with the present work will be shown.

2.2 Theoretical analysis on the riblets mechanisms

The physical mechanism of the drag reduction by riblets has been investigated in detail by many researchers, such as Wilkinson et al. (1987), Savill (1989), Walsh (1990), and Coustols and Savill (1992), although some aspects remain controversial. It has been demonstrated that riblets can delay the transition to turbulence of an excited laminar boundary layer (viscous sub-layer) (Starling and Choi, 1997). Therefore, studies of the mechanism of drag reduction by riblets focus on creating a viscosity dominated region in the base of the riblets valleys where the wall shear stress is very low. In other words, the growth rate of the momentum thickness during the non-linear stage of the transition over smooth surface is

greater than over the ribleted surface; additionally the turbulence intensity is reduced by riblets, supporting the fact that the transition to turbulence has been delayed (Tullis, 1992). Kramer (1937) presented the first hypothesis on drag reducing surfaces, although he did not provide a satisfactory explanation of the influence of riblets (Granola, Murcsy-Milian and Tamasch, 1991).

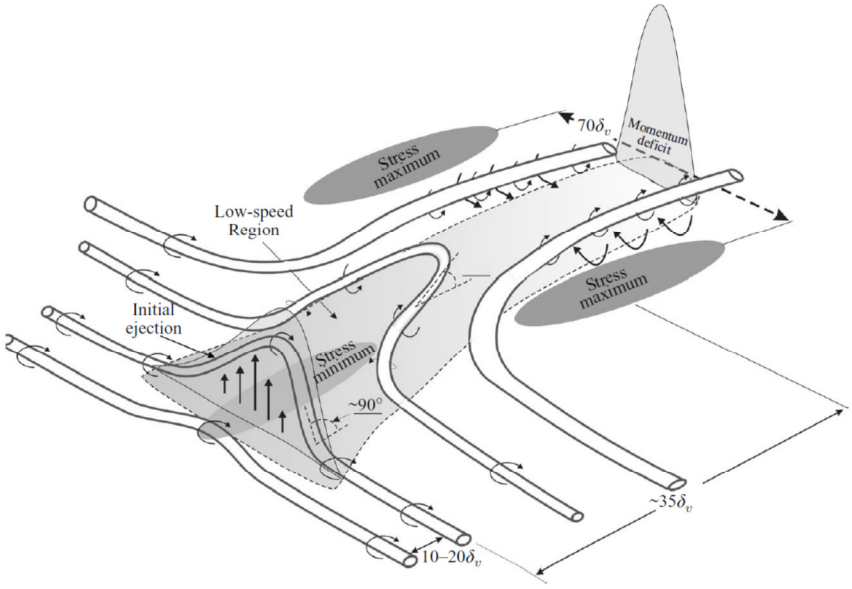

Figure 2.1: A conceptual model illustrating the process of span-wise vortex lifting and the resulting formation of a counter-rotating vortex pair, regions with wall stress extremes and low-momentum region on smooth surface (Sheng, Malkieland and Katz, 2009)

There are few theories proposed in the literature for the performance of riblets whereas most of them focus on the behaviour of the cross-flow. The first theory suggests that the generation of secondary vortices with the riblets valleys weakens the stream-wise vortices immediately above the riblets (Bacher and Smith, 1985). Robinson (1988) and Smith et al. (1989) suggested that riblets interfere with the span-wise motion of the low speed streaks at the wall. Similarly, Choi (1989, 1987) and Crawford (1996) confirmed that riblets reduce the skin-friction drag by impeding the span-wise movement of longitudinal vortices during the sweep events. Karniadakis and Choi (2003) concluded that the paired vortices over the riblets surface tend to be shorter compared to their counterpart over a smooth surface; and the span-wise spacing between them is wider, supporting the above

findings that skin friction is reduced by passive span-wise forcing. Also more recently, Goldstein and Tuan (1998) and Goldstein, Handler and Sirovich (1995) proposed that the deterioration is due to the generation of secondary stream-wise vorticity over the riblets, as the unsteady cross-flow separates and sheds small-scale vortices that create extra dissipation. Although this theory has been supported by many researchers as mentioned above, evidence by span- wise oscillations of the wall weaken the acceptance of it (Jung et al., 1992; Jimenez, 1992; Jimenez and Pinelli, 1999). They found that introducing small-scale stream-wise vorticity near the wall decreases drag by damping the larger stream-wise vortices of the buffer layer, and that inertial cross-flow effect need not be detrimental to drag reduction (García-Mayoral, 2011).

The other theory emphasizes the scale of the turbulent structures in the unperturbed turbulent wall region to optimize spacing (Choi et al., 1993; Suzuki and Kasagi, 1994; Lee and Lee, 2001). Although they showed that the stream-wise turbulent vortices embed within the grooves for riblet in the early drag-deterioration regime, their suggestions suffer from persuasive arguments for a drag increase above break down region (García-Mayoral, 2011).

Besides the mentioned theories, techniques proposed for theoretical analysis is worthy of review. Bechert and Bartnwerfer (1989) determined an effective location for the origin of the velocity profile and a “protrusion height” which is the distance between this effective velocity profile origin and the tips of the riblet peaks (Figure 2.2). This technique can provide a wall shear stress distribution by averaging wall shear stress value; but cannot obtain any drag reduction predictions. With this technique, Bechert et al. (1997) concluded that the fluctuating cross-flow component is reduced, the turbulent momentum transfer will also reduce; therefore, the shear stress will be decreased.

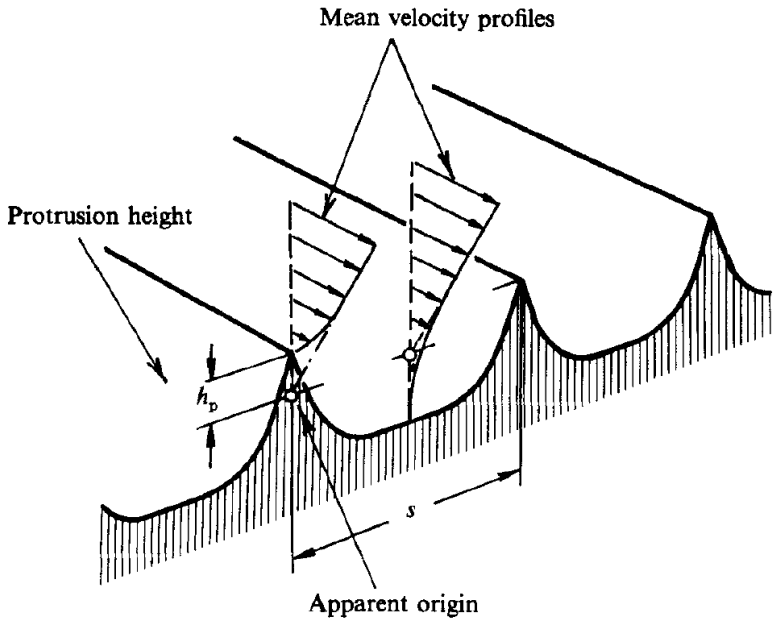

Figure 2.2: Apparent origin of a riblet surface (Bechert and Bartnwerfer, 1989)

The work of Bechert and Batenwerfer has been continued and elaborated upon by a group of researchers at the University of Milan (Luchini et al., 1991; Luchini and Trombetta, 1995; Luchini and Pozzi, 1997). They proposed that the drag reduction can be optimised by maximising the difference between the protrusion height of riblets for the longitudinal flow and that for the cross flow. In addition, Luchini studied the effects of riblets on the boundary layer stability using the e^N method. His investigation demonstrated that the Tollmien-Schlichting (T-S) waves over the triangular riblet surface are found to be excited at a lower critical Reynolds number. Another group, who followed Bechert and Batenwerfer, defined the concept that the drag reduction of riblets could be related to the difference between the normal (stream-wise) protrusion heights and the cross-flow protrusion height (Baron et al., 1993).

Most recently, García-Mayoral and Jiménez (2012) suggested that the existing experiments for the location of the breakdown collapse better with a new length scale, based on the groove area, than with the riblet spacing or depth (Figure 2.3). They claim that “the degradation for large riblets of the linear regime of drag reduction is not connected with the breakdown of the Stokes behaviour of the longitudinal velocity along the riblet grooves”. (This technique fails to provide convincing physical arguments when a three-dimensional flow perturbation occurs

at a certain height above the surface, where the shear stresses in the stream-wise and in the cross-flow directions will be different.)

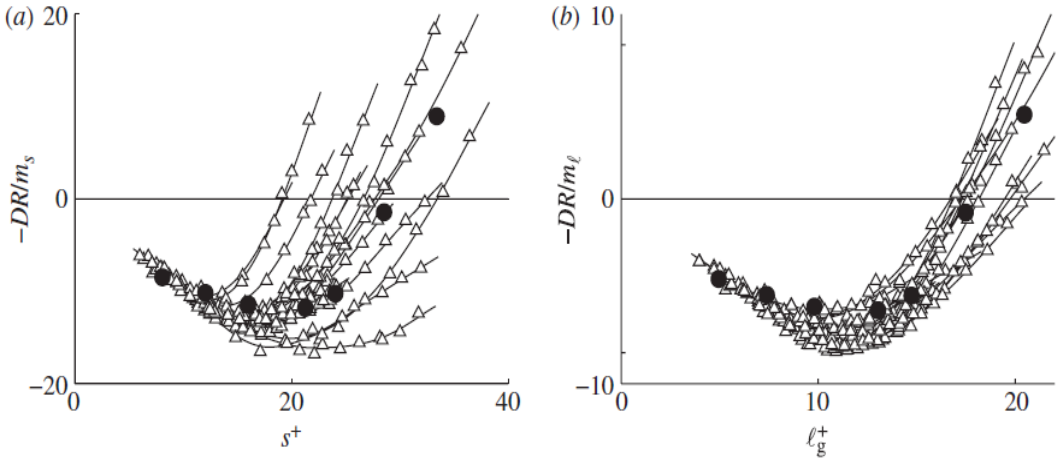

Figure 2.3: Drag-reduction curves of diverse riblets, reduced to a common viscous slope. Drag reduction (a) as a function of the spacing s+ and (b) as a function of the square root of the groove cross section, $L_g^+ = A_g^{+1/2}$. Open triangles, experimental results from Bechert et al. (1997); filled circles, direct numerical simulation results from García-Mayoral & Jiménez (2011)

2.3 Computational fluid dynamics (CFD) modelling on riblets

Similar to the most turbulent flow simulations, CFD over riblets can be classified in three groups: Reynolds-Averaged Equation (RANS), Large Eddy Simulation (LES) and Direct Numerical Simulation (DNS). Figure 2.4 demonestrates modelling challenges over riblets and micro structured surfaces.

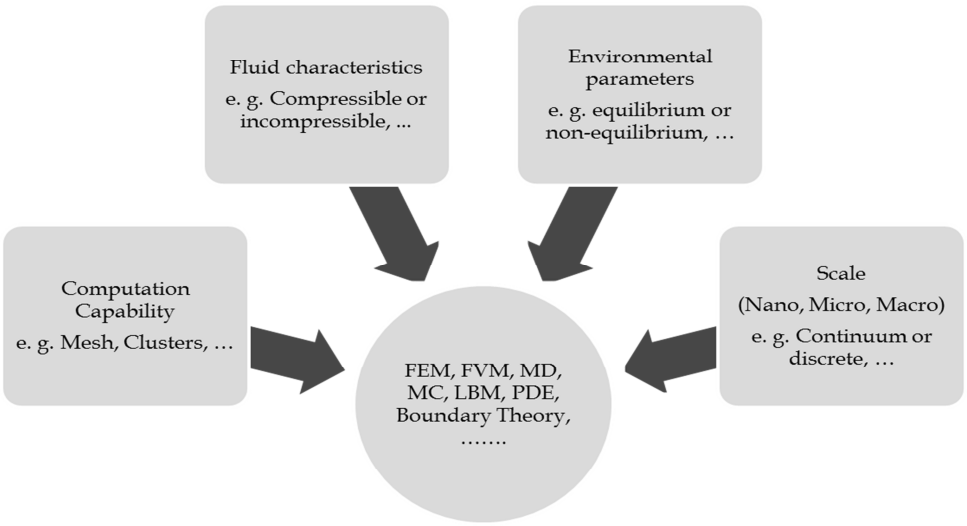

Figure 2.4: Modelling and simulation challenges over riblets and micro textures

RANS is average of NS equation over time. Although it has been extensively used in industry to provide flow statistic, it cannot provide any detailed time-dependent information. Therefore, RANS has been used mostly for simple engineering applications, and it has been historically used as commercial CFD packages. There are many flow studies over riblets that used averaged equation. For instance, Beibei et al. (2011) modelled triangular riblets with k-ε turbulence model. In addition, two attempts have been made to model the flow over riblets using low Reynolds number K-e turbulence models (Djenidi, 1991; Launder and Li, 1991). They used curvilinear grids acquired by conformal mapping which provide curved grid lines parallel to the riblets surfaces. Launder and Li obtained the results which occurred at riblets sizes 2-3 times larger than the optimum experimental size (Figure 2.5). The reason for their controversial results is because of the use of both mixing length and low Reynolds number k-e turbulence models related to the critical near wall damping assumptions.

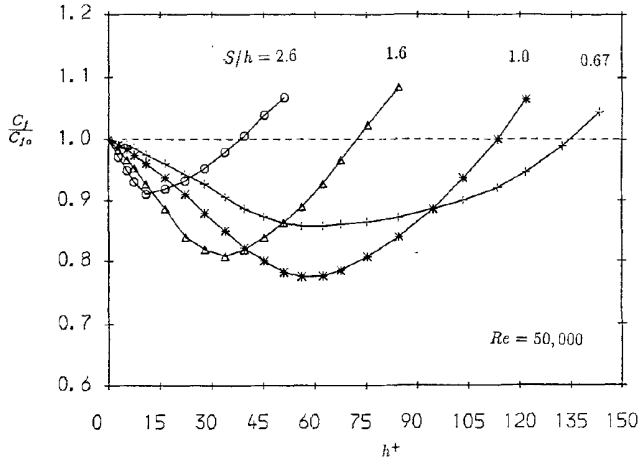

(a)

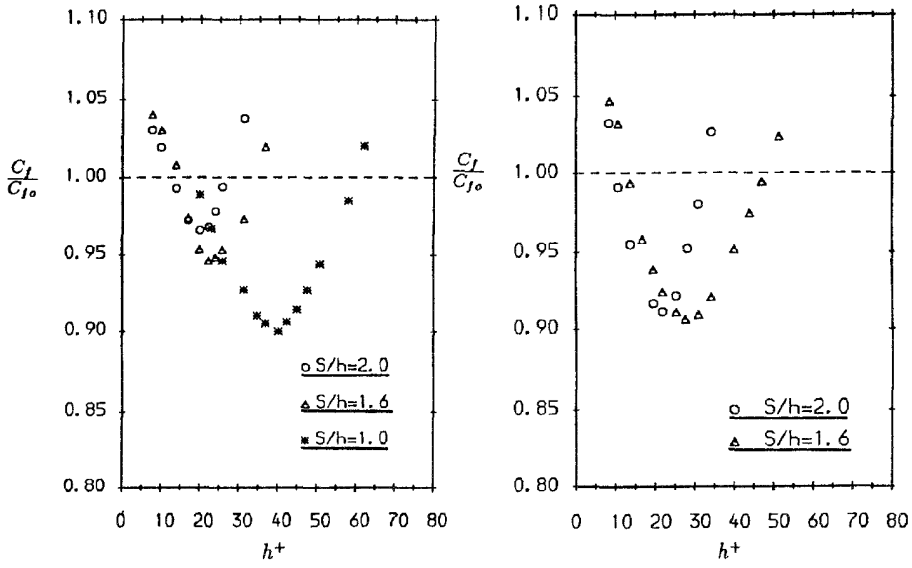

(b) (c)

Figure 2.5: Drag reduction behaviour for (a) L-shaped riblets (b) V-shaped riblets (c) U-shaped riblets (Launder and Li, 1993)

The other type of modelling is LES which separates velocity into large scale and small scale components. This is due to the fact that small scale motions play a less important role in the process of transport of mass, energy and other scalar properties. Therefore, the large eddies are more accurate than the small ones. In this method, the large scale is obtained by filtering, and small scales are represented by sub-filter model. The disadvantage of this modelling is that it does not consider all scales, omitting the very smallest ones. There are few researchers who considered this approach for flow over riblets. For instance, Peet et al. (2009)

documented Large Eddy Simulation (LES) study of turbulent flow in a channel, one wall of which is covered with riblets. Their code is second-order and unstructured finite volume solver with collocated arrangement of variables; and it solves incompressible Navier-Stokes equations using the fractional step method. Another type of eddy driven model is viscous wall region modelling. In this method, only the region between the wall and the outer edge of the viscous wall region has been considered to be simulated (Hanratty et al., 1977; Tullis and Pollard, 1994).

The most advanced method is DNS, which can solve NS equation without any averaging closure and need for a subgrid-scale model. Direct Numerical Simulation can be viewed as a numerical experiment producing a series of non-empirical solutions. Therefore, it is appropriate for addressing basic research questions regarding turbulence physics. The only disadvantage is its computational cost, which prevents DNS from being used as a general-purpose design tool. Also, this drawback leads to a severe limitation on the maximum Reynolds number that can be considered. Corrsin (1961) discussed that the number of grid points required for DNS of fully developed turbulent flow increases as $Re^{9/4}$ per time step, and a full simulation requires a large number of time steps proportional to $Re^{3/4}$. Consequently, DNS is inapplicable to solve practical industrial problems (i.e. full-scale aeronautical flows) with current computer capabilities. Many researches, such as Goldstein et al. (1995), Goldstein and Tuan (1998) and El-Samni et al. (2007), have used DNS for modelling flow over riblets.

Khan (1986) performed a direct numerical simulation of a turbulent channel flow. He used a unidirectional algebraic stress model for modelling turbulent flows. His results have been criticized by Djenidi et al. (1990) who drew attention to the low grid resolution used, and Wilkinson et al. (1987), who doubted the existence of the calculated counter-rotating vortices within the riblets valleys. Another one of the earliest attempts at DNS modelling the flow over riblets was performed by Kim et al. (1987). In 1991, Jimenez and Moin also performed direct numerical simulations of unsteady channel flow at low to moderate Reynolds numbers. In order to reduce the channel size, they could demonstrate that the near wall turbulence statistics and presumable flow mechanisms in the minimal channel are in good agreement with

the natural channel. In general, DNS for riblets can be separated into two categories: spectral methods and finite methods. Chu and Karnidakis (1993) has modelled three-dimensional incompressible Navier-Stokes equations integrated via a spectral element-Fourier method to compute the flow over riblet. For time discretization of governing equations, a high-order splitting algorithm has been employed based on mixed explicit-implicit stiffly stable schemes (Karniadakis, Israeli and Orszag 1991; Tomboulides, Israeli and Karniadakis 1989; Crawford, 1996). Table 2.1 illustrates the details of computational patameters in Crawford modelling. In this algorithm, first the nonlinear terms obtained for each Fourier component are considered. Then, the pressure equation is incorporated, and the incompressibility constraint is enforced. At the end the viscous corrections and the imposition of the boundary conditions included. Periodic conditions were assumed on the upstream and downstream domain boundaries. In addition, for the spectral element discretization, they broke up the computational domain into several quadrilaterals in two dimensions, which are mapped isoparametrically to canonical squares. Karniadakis and his group claimed that turbulence is sustained with as little as 4 Fourier-modes in the stream wise direction, but the full spectrum of scales certainly cannot be resolved with this number of modes. They also paid attention to the resolution requirements around the riblet peaks, although the grid spacing seems a little large in the stream-wise direction (Pollard, 1998).

Case	h^+	s^+	Re	Re_τ	$Drag$
A	17.70	20.41	4280	181 (u), 177 (r)	-5%
B	31.01	35.66	3280	148 (u), 155 (r)	+10%
C	18.57	21.42	3280	144 (u), 143 (r)	-2%

(a)

Case	L_{x_1}	L_{x_2}	L_{x_3}	$L^+_{x_1}$	$L^+_{x_2}$	$L^+_{x_3}$
A	5.61	2.05	1.15	1018	372	209
B	5.61	2.1	2.3	830	311	340
C	5.61	2.065	1.5	808	297	216

(b)

Table 2.1: (a) Reynolds number for the upper channel wall (u) and riblet surface (r), - presents drag reduction and + shows drag increasing (b) computational domain parameters in global and wall units (Crawford, 1996)

Duan and Choudhari (2012) simulated the boundary layer flow over riblets with the compressible Navier-Stokes equations, solved in generalized curvilinear coordinates. They assumed the fluid is an ideal gas with a linear (i.e. Newtonian) stress-strain relation; and to compute the heat flux terms, the Fourier law has been used.

The most important advantages of spectral methods is the fact that the magnitude of the expansion coefficients goes to zero when the basis-function variations correctly 'fit' the dependent-variable variations (in terms of smoothness, boundary conditions, and regions of most rapid spatial change); therefore, the error decreases faster and the model converges with exponential or 'infinite-order' accuracy. Another attractive feature of this method, specifically Fourier- and Chebyshev-based methods, is the ability to employ fast transformations when computing and when using the collocation/pseudo-spectral procedure to calculate, both of which must be done at each time step. In addition, when Fourier spectral methods have been employed in directions where the turbulence is statistically homogeneous, this automatically produces conditions whose history and spatial structure fully satisfy the governing equations. As a disadvantage of this method, it is not able to consider complex geometries; and the special treatments required to enforce inflow/outflow boundary conditions. In addition, the need to access the entire domain in each direction and employing global basis functions leads not to perform well on large distributed memory parallel systems (Coleman and Sandberg, 2010).

Finite methods are another type of DNS technique for flow over riblets which include mostly finite volume and finite different methods. Choi et al. (1993) have performed a DNS study on one wall of a plane channel using the finite volume method. The computational box is chosen to be a minimal flow unit (Jimenez and Moin, 1991). Table 2.2 demonstrates the computational parameters over sawtooth riblets. A uniform mesh is used in the stream-wise direction and the stream-wise spacing is rather coarse. A non-uniform mesh with hyperbolic tangent distribution is used in the wall normal direction. In span-wise, a non-uniform orthogonal mesh is employed with concentrations of the grid around the riblets peaks. For advancement, a fully implicit method has been used which approximates the spatial derivatives using information at the new time step. Figure 2.6 shows the coordinate transformation in this DNS.

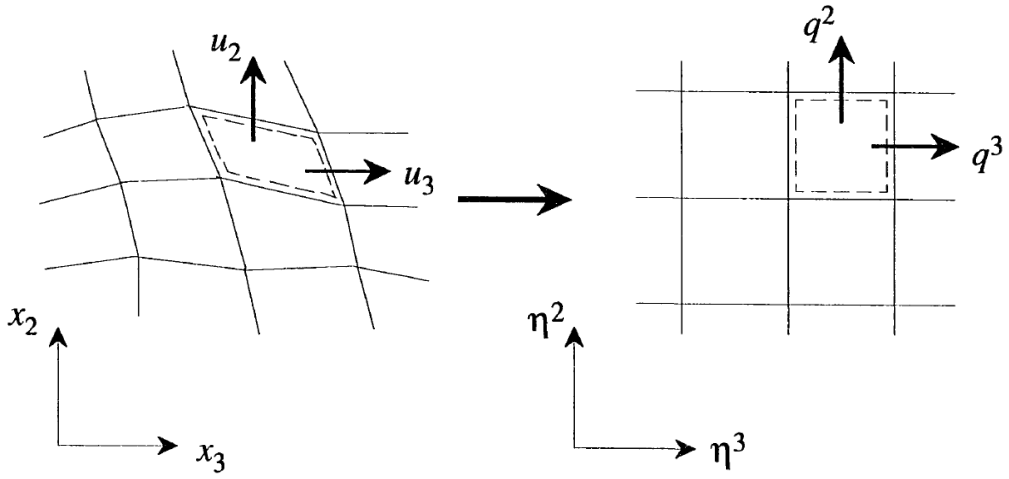

Figure 2.6: Coordinate transformation (Choi et al., 1993)

Case	s/δ	s^+	h^+	α	$N_{x_1} \times N_{x_2} \times N_{x_3}^+$	Δx_3^+
A	0.2270	40	20.0	45^o	$16 \times 129 \times 128$	1.28
B	0.2270	40	34.6	60^o	$16 \times 129 \times 128$	1.28
C	0.1135	20	10.0	45^o	$16 \times 129 \times 256$	0.64
D	0.1135	20	17.3	60^o	$16 \times 129 \times 256$	0.64

Table 2.2: Parameters for the simulation over sawtooth riblets, 6 % drag reduction achieved by Case D (Choi et al., 1993)

The finite methods are generally suitable to parallelization, easy to implement with high-order accuracy; and their high-order finite nature can provide an excellent compromise between accuracy and flexibility for flows involving realistic geometries, such as riblets. Moreover, curvilinear coordinates and grid stretching is routinely used to obtain accurate results with less computational cost (Coleman and Sandberg, 2010). Recently, Garcıa-Mayoral and Jimenez (2012) have modelled riblets with direct numerical simulations at Reτ ≈ 550. They used a pseudo-spectral, multi-block, immersed-boundary, fractional-step, constant-flow-rate, Runge-Kutta Navier-Stokes solver that enforces incompressibility in a weak sense. Also the results have been compared with Reτ ≈ 180. They found that the differences between the results for different Reτ are small, therefore the Immersed boundary method can be considered as another accurate method for simulating flows over riblets and micro-textures (Figure 2.7).

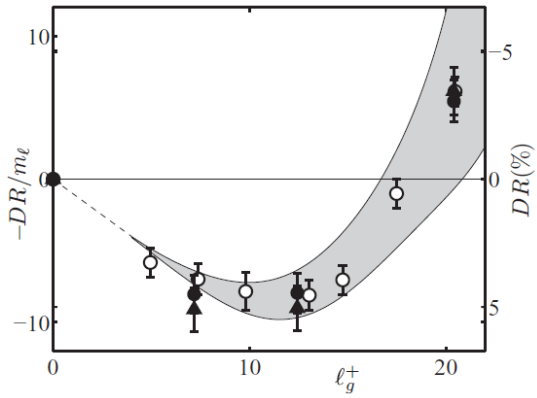

Figure 2.7: Friction-reduction for DNSs of channels with rectangular riblets at Reτ ≈ 180 and 550. O, *DR* and DR/m_l at Reτ≈ 180; ●, *DR* at Reτ ≈ 550; ▲, DR/m_lat Reτ ≈ 550. Error bars have been estimated from the time-history of C_f.The shaded area envelopes results for several experimental riblets (Garcıa-Mayoral and Jimenez, 2012)

2.4 Experimental measurement

2.4.1 Scaling of mean velocity in turbulent boundary layers (TBL)

The interpretation of experimental measurements of the mean velocity depends on the choice of appropriate scaling laws. As has been mentioned in the previous chapter, a turbulent boundary layer can be classified into three regions: the inner (viscous sub-layer), overlap (buffer layer), and outer regions (Millikan, 1938), as shown in Figure 2.8. (Figure 2.1) In the following, the explanation of the scaling laws for the inner and outer regions, as well as the overlap region, is provided.

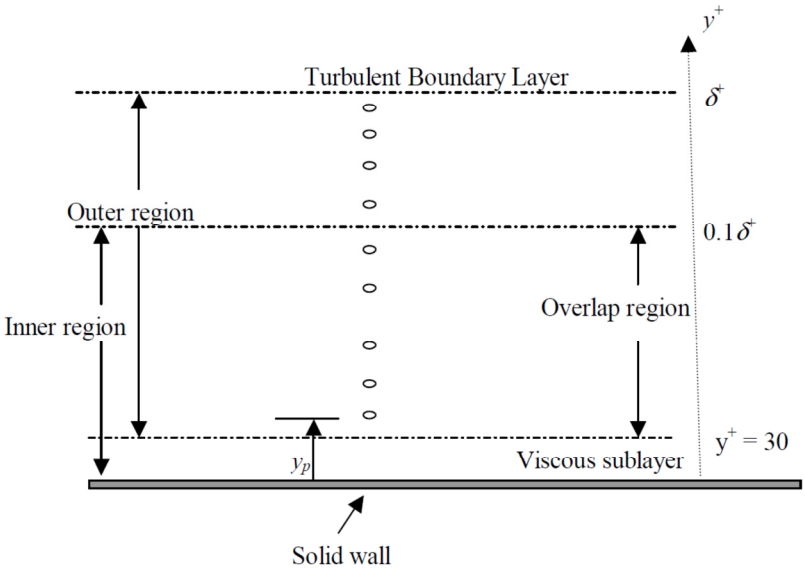

Figure 2.8: Turbulent boundary layers regions

According to Prandtl (1932) and Rotta (1962), viscosity and wall shear stress are the significant parameters which influence the mean velocity profile in the inner region; also, at sufficiently high Reynolds numbers, in the outer region, the energy-containing motions are independent of viscosity:

$$U = f_i(y, \tau_w, \nu, \rho) \tag{2.1}$$

$$U_e - U = f_0(y, \delta, u_0) \tag{2.2}$$

where u_0 is the velocity scale in the outer region. Consequently, dimensional analysis of Equations 2.1 and 2.2 leads to the following scaling of the mean velocity profile in the inner and the outer regions, respectively:

$$U^+ = f_i(y^+) \tag{2.3}$$

$$\frac{U_e - U}{u_0} = f_0(\eta) \tag{2.4}$$

where f_i and f_0 are the dimensionless functional parameters in the inner and outer functions, respectively, and $\eta = y/\delta$. Equation 2.3 is also known as the "Defect Law", and Equation 2.4 is the classical "Law of the Wall", which implies complete similarity in the inner region. According to George and Castillo (1997), the outer velocity scale is proportional to the free-stream velocity, U_e. Also, Zagarola and

Smits (1998) proposed the following outer velocity scale for a smooth wall turbulent boundary layer which is proportional to the mass flux deficit:

$$u_0 = U_e \int_0^1 \left(1 - \frac{U}{U_e}\right) d\left(\frac{y}{\delta}\right) = U_e \frac{\delta^*}{\delta} \tag{2.5}$$

This outer velocity scale has been used to successfully collapse the mean velocity defect profiles on both smooth (Castillo and Walker, 2002) and rough surfaces (Seo, 2003).

Although, the inner and outer regions have been investigated thoroughly, describing the mean velocity profile in the overlap region continues to be a subject of controversy. The importance of finding accurate way to scale this region raise since the effective surface roughness for drag reduction is in this region. Since the inner length scale (ν/U_τ) and the outer length scale (δ) are presumably too small and too large, respectively, the dynamics of the flow in the overlap region is independent of all length scales, except the distance from the wall (Tennekes and Lumley, 1972). Millikan (1938), Clauser (1954) and Panton (1990) propose a logarithmic law for both ducts and turbulent boundary layers in the overlap region. In addition, several researchers such as Barenblatt (1993), George and Castillo (1997), Afzal (2001), have investigated alternatives due to inconsistencies in fitting the experimental data to log law relations. They suggested power laws as an alternative formulation for the overlap region in the limit of finite Reynolds numbers.

Theoretical and experimental arguments continue to consider both the power law and log law. For example, Zagarola et al. (1997) studied turbulent pipe flow over a range of Reynolds numbers. They concluded that the mean velocity consists of two distinct regions: a power law region for $50 \leq y^+ \leq 500$ or $0.1R^+$ ($=U_\tau R/\nu$, where R is the pipe radius, the upper limit being dependent on Reynolds number), and a log law region for $500 < y^+ < 0.1R^+$. In an attempt to resolve the log law versus power law issue, Panton (2000) proposed in his study that the log law and the power law apply to different regions of the boundary layer; more specifically, that a power law extends into the inner part of the wake region whereas a log law does not. Panton (2002) also evaluated the Barenblatt-Chorin-Prostokinshin power law for turbulent boundary layers and found that the method is very sensitive, and can

produce profiles that do not closely match the data. Also, the boundary layer measurements reported by Österlund et al. (2000) provide evidence in support of a log law; however, reconsideration of the same data by Barenblatt et al. (2000) suggests that they are better described by a power law. Buschmann and Gad-el-Hak (2003) investigated the extent to which logarithmic and power law profiles describe the mean velocity profile in the overlap region of a smooth wall boundary layer. They concluded that there exists a region in the overlap layer that can be described by both power law and logarithmic profiles. (Akinlade, 2005)

In spite of the fact that a power law was originally proposed by Nikuradse (1932) about seven decades ago, many researchers have preferred the use of a logarithmic law to model the velocity profile in wall-bounded turbulent shear flows. The range of y^+ for which the power law fits the velocity profile has been noted to be different from that of the logarithmic law (Buschmann and Meniert, cited in Akinlade 2005, p. 22; Panton, 2000). More specifically, the power law allows the lower edge of the wake zone to be fitted, while a small region in the lower part of the logarithmic region is not represented (Akinlade, 2005). Therefore, in this study the Logarithmic low has been chosen for scaling of mean velocity in turbulent boundary layers.

According to classical theories, the mean velocity profile in the overlap region is best described by the logarithmic law. Millikan (1938), followed by Clauser (1954), matched the Law of the Wall and Defect Law to obtain a logarithmic velocity profile for a smooth wall to describe the outer part of the inner region as follows:

$$U^+ = \frac{1}{k} ln y^+ + B \tag{2.6}$$

Also the inner part of the outer region:

$$\frac{U_e - U}{U_\tau} = -\frac{1}{k} \ln\left(\frac{y}{\delta}\right) + A \tag{2.7}$$

where k=0.41 (the von Karman constant), A=2.5 and B=5.0 are the universal constants and independent of Reynolds number. In another attempt, Coles (1956) incorporated the wake function into the logarithmic law with the aim of describing both the overlap and outer regions of a smooth wall boundary layer:

$$U^+ = \frac{1}{k} ln y^+ + B + \frac{2\Pi}{k} w(\eta) \quad (2.8)$$

where Π is the Coles wake parameter and w(η) is the wake function. Based on a curve fit approximation to experimental data, the wake function is expressed as:

$$w(\eta) \approx 2sin^2(\frac{\pi}{2}\frac{y}{\delta}) \quad (2.9)$$

The investigation of logarithmic low on the rough wall turbulent boundary layer by Krogstad et al. (1992) suggests the following; the mean stream-wise velocity distribution across both the overlap and outer regions:

$$U^+ = \frac{1}{k} ln \frac{(y+y_0)U_\tau}{\nu} + B - \Delta U^+ + \frac{2\Pi}{k} w(\frac{(y+y_0)}{\delta}) \quad (2.10)$$

where y_0 is the virtual origin, which represents the virtual location of the wall relative to the nominal top of the roughness elements, and $\Delta U^+ = \Delta U / U_\tau$ is the roughness function, which represents the downward shift of the linear portion of the velocity profile plotted on a logarithmic plot (Akinlade, 2005).

2.4.2 Determination and correlation of skin friction

Experimental and theoretical study of drag reduction can be accurate with a precise method to determine the skin friction on smooth and rough surfaces. Many reliable techniques for estimating the skin friction (or wall shear stress) have been developed for a smooth wall turbulent boundary layer including use of correlations based on total pressure measurements at the surface (i.e. using a Preston tube), oil-film interferometry, the momentum integral equation and indirect methods based on fitting data to the mean velocity profile. This indirect method which has been used most for riblets includes the 'classical' Clauser technique, and fitting profiles based on either a defect law or power law. Beside the type of used methods, many researchers, such as Schultz-Grunow (1941), Coles, (1962), Osaka et al. (1998), Tachie et al. (2001), investigated the prediction of skin friction on a smooth surface for practical applications. Before review of the correlations, an investigation into how skin friction determination is needed.

Hama's formulation, as an alternative to the Clauser technique, is a commonly used defect form for the velocity distribution in zero pressure-gradient boundary

layers on smooth and rough surfaces (Akinlade, 2005). For small values of y/δ, the defect profile is dominated by the logarithmic term and is written as:

$$\frac{U_e-U}{U_\tau} = -\frac{1}{k}\ln\left(\frac{yU_\tau}{\delta^* U_e}\right) - 0.6, \qquad \text{where} \quad \left(\frac{yU_\tau}{\delta^* U_e} \leq 0.045\right) \tag{2.11}$$

For larger values of y/δ, the wake contribution dominates and Hama proposed the function:

$$\frac{U_e-U}{U_\tau} = 9.6\left(1 - \left(\frac{10yU_\tau}{3\delta^* U_e}\right)\right)^2, \qquad \text{where} \quad \left(\frac{yU_\tau}{\delta^* U_e} > 0.045\right) \tag{2.12}$$

In the presented formulation, the displacement thickness δ^* is used as the reference length scale. Bandyopadhyay (1987) suggests that the Hama profile could be fitted to obtain a reliable estimate of friction velocity irrespective of surface condition. The benefit of Hama's formulation over the Clauser technique is that the profile covers virtually the entire boundary layer region.

The experimental evidence from some studies of the near-wall turbulent flows demonstrated that the friction velocity gained from the Hama formulation is consistently higher than that obtained from either a momentum balance or by extrapolating the Reynolds stress to the wall (Bandyopadhyay, 1987; Perry et al., 1987; Krogstad et al., 1992). Bradshaw (1987) showed that this may be due to the lower value of the strength of the wake prescribed in the Hama formulation. Further experimental investigations have shown that the strength of the wake depends on roughness effects, Reynolds number, and stream-wise turbulence level.

Another alternative to Clauser technique and Hama's formulation has been presented by Finley et al. (1996). The first attempt to develop this method was by Granville (1976) and Krogstad et al. (1992). Finley et al. suggested the use of the velocity defect law in terms of a formulation that does not implicitly fix the strength of the wake, but rather allows its value to be optimized while ensuring a reliable determination of the friction velocity. Therefore, the mean defect profile is going to be as follows:

$$\frac{U_e-U}{U_\tau} = \frac{2\Pi}{k}\left(w(1) - w\left(\frac{y}{\delta}\right)\right) - \frac{1}{k}\ln\left(\frac{y}{\delta}\right) \tag{2.13}$$

The only advantage of using the defect profile is that velocity data outside the inner layer can be included, especially for high Reynolds number flows (Akinlade, 2005).

All the mentioned methods use the Defect law or Logarithmic law to determine skin friction. In addition, three separate researchers have followed the power law formulation by Barenblatt (1993), George and Castillo (1997) and Djenidi et al. (1997). Barenblatt obtained the following skin friction relation:

$$C_f = 2(\frac{U_\tau}{U_e})^2 = 2\left(\frac{1}{\exp(3/2)}(\frac{\exp(3/2\alpha)}{C})\right)^2 \quad (2.14)$$

And the skin friction relation gained by George and Castillo is expressed as:

$$C_f = 2(\frac{U_\tau}{U_e})^2 = 2\left(\left(\frac{C_0}{C_i}\right)^{1/1+\gamma}\left(\frac{U_e\delta}{\nu}\right)^{-\gamma/1+\gamma}\right)^2 \quad (2.15)$$

The values of the skin friction obtained from these formulations have been shown to be comparable to the values obtained by other reliable techniques (Tachie et al., 2001). The following is a review of the skin friction correlation.

The skin friction correlation is generally defined as the empirical relationships between C_f and Re_θ. Fernholz and Finley (1996) discussed that many empirical correlations were curve fits to measurements without theoretical justification. In one of the early attempts to define the correlation, White (1974) gained a power law approximation for C_f on a smooth wall turbulent boundary layer, given by:

$$C_f \approx 0.012{Re_\theta}^{-1/6} \approx 0.018{Re_\delta}^{-1/6} \approx 0.0128{Re_{\delta^*}}^{-1/6} \approx \frac{0.455}{ln^2(0.06Re_x)} \quad (2.16)$$

Fernholz et al. (1995) suggested a correlation for the skin friction on a smooth wall as:

$$C_f = 0.32(1.77 + \ln(Re_\theta))^{-2} \quad (2.17)$$

Also, Osaka et al. (1998) proposed an empirical expression for the skin friction as follows:

$$\frac{1}{C_f} = 20.03(logRe_\theta)^2 + 17.24(logRe_\theta) + 3.17 \quad (2.18)$$

In more recent investigation, Tachie et al. (2001) obtained a skin friction correlation for smooth wall in an open channel flow:

$$C_f = 4.13x10^{-2} - 2.687x10^{-2}(logRe_\theta) + 6.528x10^{-3}(logRe_\theta)^2 - 5.54x10^{-4}(logRe_\theta)^3 \quad (2.19)$$

The mentioned studies considered smooth walls for investigation; the following is a review of finding correlation on the rough surfaces and featured surfaces with riblets.

For a rough-wall turbulent boundary layer, Schlichting (1979) developed a skin friction correlation based on the experimental data of Nikuradse (1932) for sand-roughened plates, given by:

$$C_f = (2.87 + 1.58log_{10}(x/k))^{-2.5} \quad (2.20)$$

Acharya et al. (1986) suggested a skin friction correlation, given by:

$$\sqrt{\frac{2}{C_f}} = \frac{1}{k} ln\left(\frac{\delta^*}{k}\sqrt{\frac{2}{C_f}}\right) + A \quad (2.21)$$

where A is a constant. Also, Seo (2003) proposed a skin friction correlation:

$$C_f = 2\left(\frac{C_{0\infty}(1+C_{0k})(1+C_{ik})}{C_{i\infty}}\right)^2 \delta^{+-(\gamma_\infty+\gamma_k)} exp\left(\frac{2A}{(\ln(\delta^+))^\alpha}\right) \quad (2.22)$$

where $C_{0k} = 0.00576k^{+0.517}$, $C_{ik} = 0.03551k^{+0.55647}$, and $\gamma_k = 0.0065k^{+0.60126}$.

For ribleted surfaces, based on the experimental data of the drag and velocity profile measurements of Sawyer and Winter (1987), Gaudet (1987) proposed a skin friction correlation. He used thickness parameters for equilibrium flow, known as the defect thickness (Δ), defined by Clauser (1954):

$$\Delta = \int_0^\infty \frac{U_e - U}{U_\tau} dy = \delta^* \lambda \quad (2.23)$$

where $\lambda = \sqrt{2/C_f}$ is related to the local skin friction. An integral shape factor, G, which remains constant in an equilibrium boundary layer, was defined as follows:

$$G = \frac{1}{\Delta}\int_0^{\infty}(\frac{U_e - U}{U_\tau})^2 dy \tag{2.24}$$

where G is related to the ordinary Kármán-type shape factor, H, by the following expression:

$$H = \frac{\delta^*}{\theta} = \left(1 - \frac{G}{\lambda}\right)^{-1} \tag{2.25}$$

and θ is the momentum thickness. Gaudet proposed a skin friction correlation as follows:

$$C_F = \frac{2\alpha A h}{\lambda x}\left(1 - \frac{G}{\lambda}\right) e^{k\lambda} \tag{2.26}$$

Where

$$A = e^{-k(g(h^+) - \emptyset(0))} = 0.0443 \tag{2.27}$$

2.4.3 Experimental investigation over riblets

This section will briefly discuss some of experimental measurement techniques, such as Hot-Wire, VITA and visualization, which have been used on the flows over riblets. The advantages of using riblets in many engineering applications have been notified. For instance, the flight testing of aircraft with riblets by Boeing (McLean et al., 1987), Airbus (Coustols and savill, 1992) and NASA (Walsh et al. 1989) demonstrated the importance of the effect of riblets. Robert (1992) summarized some tests on airfoils by researchers, such as Szodruch (1991), who estimated an overall 2% drag reduction on the flight tests of a commercial aeroplane (Airbus 320) with riblets over 70% of its surface. Sareen (2012) employed different size of sawtooth riblets applied to DU 96-W-180 airfoil for wind turbine. An average drag reduction of 2-4% was observed for a range of riblet sizes and Reynolds numbers. The optimal V-shape riblet size was found to be 62 μm (Figure 2.9). Also, Lee and Jang (2005) reported reduction of the overall drag of airfoils by riblets with

optimum spacing of 30-70 µm. Similar results on aircraft have been obtained by Viswanath (2002).

Re	Percentage Drag Reduction			
	44 μm	62 μm	100 μm	150 μm
1,000,000	0–1%	2–4%	2–4%	+
1,500,000	1–2%	4–5%	2–4%	++
1,850,000	0–1%	1–2%	++	++

(a)

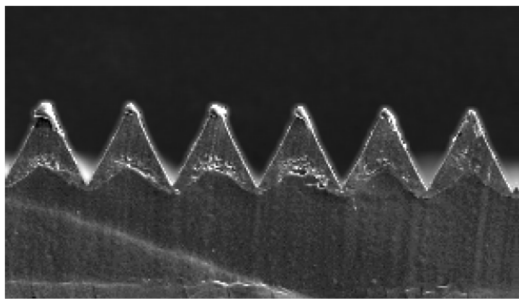

(b)

Figure 2.9: (a) Measured Percentage Drag Reduction with Riblets on the DU 96-W-180 Airfoil, (b) 62 µm riblets (`+' symbol indicates a drag increase of less than 4% and a `++' symbol indicates a drag increase of more than 4%) (Sareen, 2012)

Not only the aeronautical application but other industrial applications such as high speed trains have shown an interest in the use of riblets (GEC Alsthom, 1991). Biological surfaces are another type of applications with geometrically complex textures (Hahn et al., 2002; Kong and Schetz, 1982; Jimenez et al., 2001). Itoh et al. (2006) investigated the flow over seal fur with a dependence on mean hair separation similar to that of riblets. They could obtain drag reductions of up to 12%.

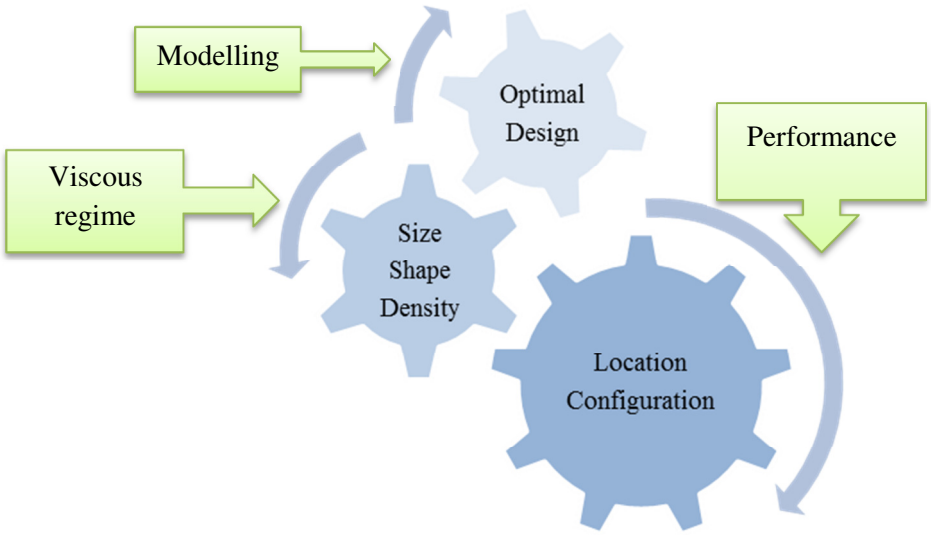

Figure 2.10: Groove spacing, depth and cross section (s, h, A_g) expressed in wall units has been considered as riblets' scaling. Location and configuration rise challenges for geometrically complex areas

A broad review of the effect of riblets with different geometries in wind tunnel was that of Walsh (1990), Choi (2000), Bushnell (2003), Vukoslavcevic et al. (1992), Park and Wallace (1994), Walsh & Lindemann (1984), and Lee and Lee (2001).

The initial drag reduction studies with riblets were those of Walsh and Weinstein (1978) and Walsh (1980, 1982) at NASA Langley. They used a direct drag balance in a wind tunnel to examine the drag reduction behaviour of various riblets shapes with sizes of approximately $s^+, h^+ = 10 - 15$. They could reach a drag reduction of up to 7-8% for V, U and L groove riblets which appeared to be the most effective shapes due to the sharper peaks. The results demonstrated that the aspect ratio h/s of the riblets appears to have a major effect on the drag reduction. As shown in Figure 2.10, Groove spacing and depth expressed in wall units has been considered as riblets' scaling. Dubief et al. (1997) have measured the statistics of $\partial u/\partial y$ over a smooth wall and a riblet surface using parallel hot wires. They observed that the mean square value of $\partial u/\partial y$ over the riblets is smaller than over the smooth wall; also, they conclude, on the basis that $\partial u/\partial y$ is a major contributor to the span-wise vorticity, the results demonstrate that the mean square span-wise vorticity is reduced near a riblet surface.

Generally in experimental study of the flow over riblets, the law of the wall relationship can be applied. The normal law of the wall (Coles, 1956) gives the mean stream-wise velocity profile over a flat wall as:

$$u^+ = \frac{1}{k} lny^+ + C - F \tag{2.28}$$

where k~0.41 is von Karman's constant, C~5.0 is the smooth wall constant and F is roughness factor. Some researchers, such as Tani (1988), Sawyer and Winter (1987) and Choi (1989), considered the effect of riblets as an "upward" shift of the profile corresponding to negative values of the F term. Choi found that the fluctuation intensity of the wall shear stress was considerably lower in the riblets valleys than over flat walls and contained numerous periods of very low "quiescent" fluctuation intensities.

Among all the experimental measurements which have been taken over riblets walls, only two groups, Vukoslavcevie et al. (1987) and Benhalilou et al. (1991), considered the measurements within riblets valleys (Table 2.3). Vukoslavcevie et al. measured riblets with dimension of $s^+ = 2h^+ = 35$; and the second group considered riblets sizes of $s^+ = 2h^+ = 30$. In the riblet valleys, both groups measured very low speed flows in the riblet valleys with the wall shear stress dropping nearly to zero at the base of the valleys. In contrast, the wall shear stress was reported to increase by 85-100% over the riblet peaks. Benhalilou et al., using the laser Doppler velocimetry, measured the span-wise as well as the stream-wise velocity fluctuations while Vukoslavcevie et al used a hot-wire probe only to measure the stream-wise velocity fluctuations. They results appear to be confirmed by the hot-film measured wall shear stresses in the valleys of similarly sized L groove riblets by Choi (1989). Other researchers, including Sawyer and Winter (1987), measured drag reduction for approximately the same riblets geometry and found that these sizes were too large to produce drag reduction and were drag neutral. However, the measurements by Vukoslavcevie et al. (1987) and Benhalilou et al. (1991) are considerably more detailed than other studies which were only able to measure above the riblets peaks.

Study	s^+	h^+	Methods
Vukoslavcevie et al. (1987)	35	17.5	Laser Doppler Velocimetry
Benhalilou et al. (1991)	30	15	Hot-Film

Table 2.3: Measurements within riblets valleys

In particular, mean and local velocity profiles and turbulent statistics within and above the riblet grooves have been reported for experiments in water and oil channels (Bechert et al., 1992, 1997; Bruse, 1993; Bechert et al., 1997; Suzuki and Kasagi, 1994). Bechert and his colleagues at DLR Berlin have tested a combination of blade riblets and ejection slits to increase the amount of drag reduction with an accuracy of ±0.3%. With this combination, a maximum drag reduction of nearly 9% was achieved. Figures 2.11 and 2.12 illustrate the measurements with sawtooth and semi-circular scalloped rib lets.

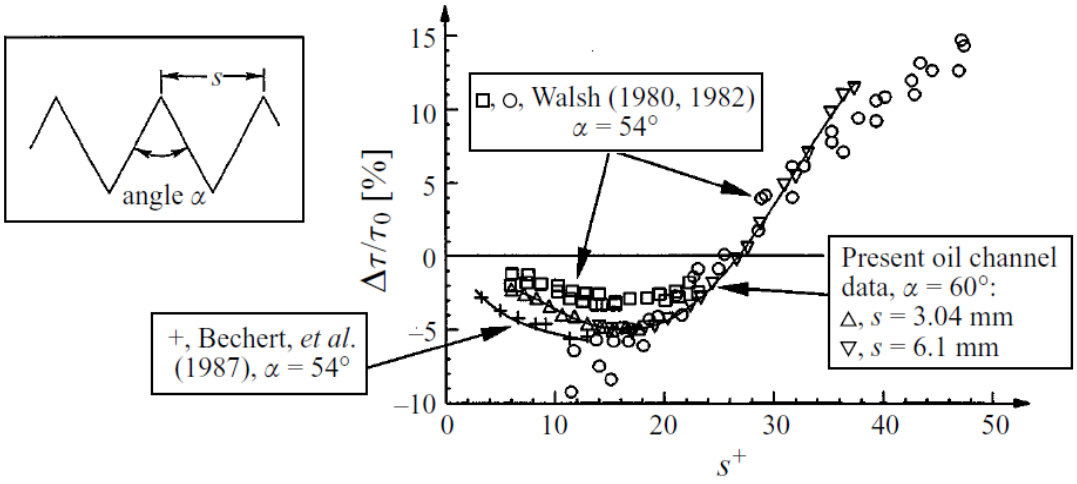

Figure 2.11: Measurements with sawtooth riblets (Bechert et al. 1997)

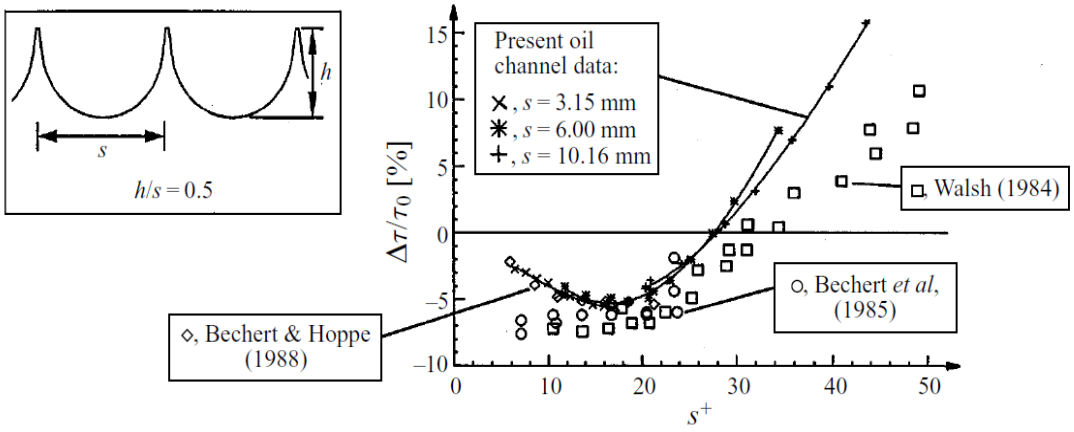

Figure 2.12: Measurements with semi-circular scalloped riblets (Bechert et al. 1997)

One of the standard techniques in the investigation of turbulent boundary layer flows over flat plates and riblets is the use of variable interval time averaging (VITA). In this method a short time interval r.m.s. value is compared to the long term r.m.s value, where the used value is typically the stream-wise velocity that has been measured at a fixed point (Blackwelder and Kaplan, 1976). In conditional averaging techniques, a burst event should be defined by establishing threshold criteria in the measurement of some turbulence quantity (Kim et al., 1971). The VITA has been used by Hooshmand et al. (1983), Choi (1989), Walsh (1982) and Gallager and Thomas (1984) to compare burst frequencies over flat and riblets walls. Choi (1989) used this technique to measure a bursting frequency and conditionally averaged wall shear stresses and cross-stream velocity fields in the valleys of L groove riblets. The results from these experiments are contradictory due to the fact that the VITA technique was inappropriate for use over riblets because of the large number of parameters that are required by the technique, and the lack of a proper definition of bursts as discreet events and their association with the entire low speed streak lift up and dissipation process (Hooshmand et al. 1983; Robinson 1988).

Another way to study the effect of riblets is to investigate the sweep and ejection events using the quadrant detection technique (Comte-Bellot et al. 1978; Schwarz-van Manen et al. 1990). Bogard and Tiederman (1986) defined a critical time between events to characterize these Reynolds stress producing events as either

grouped (multiple) or single events. Their results show that the ejection frequency over riblets decreases but the sweep frequency increases. They concluded no significant differences in either the sweep or ejection frequencies over the flat plate and riblet surfaces were observed above $y^+ \sim 35$. Tang and Clark (1992) confirmed the same conclusions using similar techniques.

In addition, flow visualization is the technique that has been used to measure the flow over riblets with particular attention to the behaviour of the flow in the riblets valleys. Gallager and Thomas (1984) and Bacher and Smith (1985) noticed a "quiescent pooling" of low speed flow in dye marked water flows in the V groove riblets valleys with dimension of $h^+ = s^+ = 15$. Similar results have been observed in smoke marked air flows over riblets with sizes of $2h^+ = s^+ = 16$ and $2h^+ = s^+ = 30$ by Hooshmand et al. (1983) and Clark (1989, cited in Tullis and Pollard 1993, p. 300), respectively. Moreover, near wall low speed streaks can be investigated by flow visualization on the effect of riblets. These streaks over flat walls have a spacing that increased with distance from the wall (Smith and Metzler, 1983); but this method is not reliable since the riblets surface location and the influence of the decreased friction velocity lead to difficulties in comparing the various riblets geometries with flat walls (Akinlade, 2005; Gallager and Thomas, 1984; Bacher and Smith, 1985; Choi, 1989). In addition, Hooshmand et al. (1983) did not observe any change in the low speed streak spacing.

Although most of the existing experiments for drag reduction on the surface considered two dimensionally longitudinal grooves, there are few attempts that investigated three-dimensional rib patterns. Bechert et al. (2000) examined the texture similar to the skin of fast sharks, sharp edged fin-shaped elements arranged in an interlocking array (as shown in Figure 2.13). They carried out the experiment on wind tunnels using direct force balances and oil channel. They claimed that the 3D riblet surfaces do indeed produce an appreciable drag reduction but they do not work reasonably as drag reducing devices. Also they observed the optimum drag reduction for short 3D riblets occurs at a lower rib height than for longer 3D riblets or for infinitely long 2D rib lets, supported with detailed data information as illustrated in Figure 2.14.

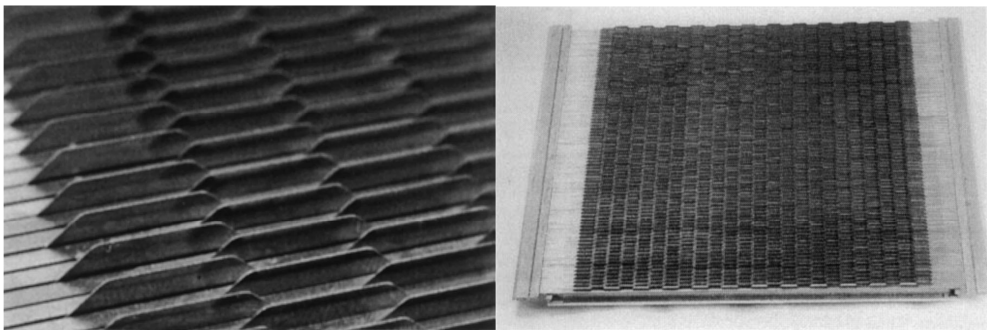

Figure 2.13: (a) Detailed photograph of the staggered fins on the test plate (b) Test plate with staggered fins for oil channel measurements (Bechert et al., 2000)

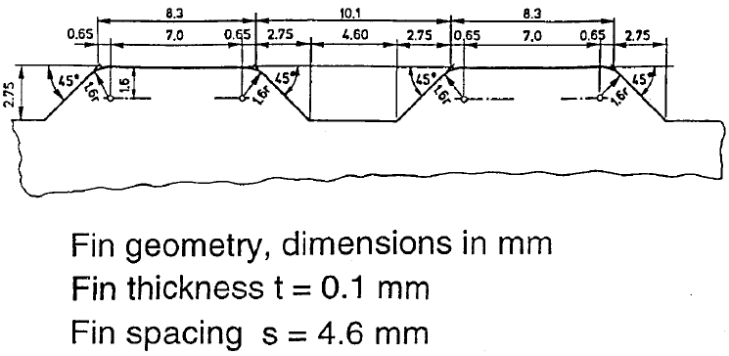

(a)

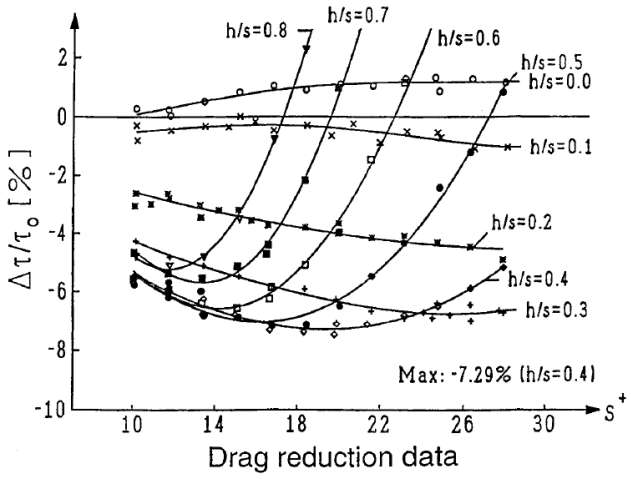

(b)

Figure 2.14: (a) Trapezoidal fin shape, (b) Two different Fins' shapes, Trapezoidal and rectangular, with three different lengths for each of them have been compared. Trapezoidal Fins of medium length (l=2s) perform slightly better (7.3%) than long Fins. The optimum s+ lies at higher s^+=19. On the other hand, the optimum rib height is lower, at h = 0.4s (Bechert et al. 2000)

2.5 Manufacturing of ribleted surfaces

Riblets used in industries (i.e aviation) require spacing at or below 1 mm. Even for study, most researchers have employed traditional milling or molding methods over the microfabrication techniques used in the micro structure production. The small sizes of riblets make their manufacture very challenging. On the other hand proper consideration for manufacturing and design should be made. Different methods such as laser machining (Siegel et al., 2008), EDM (Uhlmann et al., 2004), microgrinding and microplanning (Wang et al., 2010) have been implemented to obtain widths of about 20 µm for riblets. The micromilling process is also suitable for machining the microstructures (Fischer, 2000).

Lee and Jang (2005) fabricated the riblets according to the process described by Han et al. (2002). They used an anisotropic etching technique for fabricating V-grooved micro-riblet. Figure 2.15 illustrates the sizes of riblets was etched on a silicon wafer. Using this technique on a large area can lead to misalignment between the patterns on the ultra-violet (UV) mask and the crystal lines of the silicon wafer. To overcome this challenge, they used a polydimethylsiloxane (PDMS) micro-molding technique. The result of fabrication leads to a flexible film that can be attached to a curved surface.

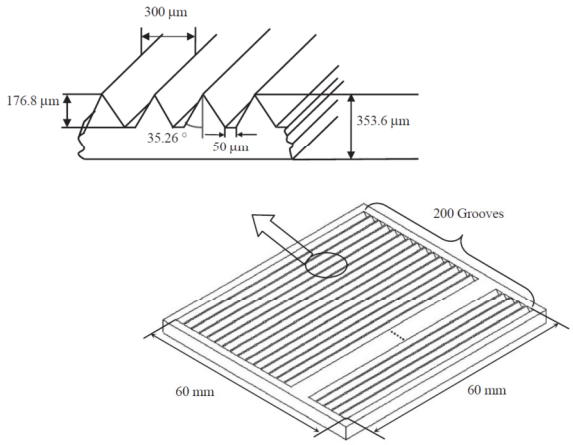

Figure 2.15: Schematic diagram of a micro-riblet film (MRF) (Lee and Jang, 2005)

Klocke and Feldhaus (2007) developed a new and incremental rolling process in order to produce riblet surface structures industrially (Figure 2.16). Their research proved that it is, in principle, feasible to produce defined riblet structures on the material, Ti-6Al-4V by employing the rolling process. Similarly, Hirt et al. (2007) used the rolling process for manufacturing riblets.

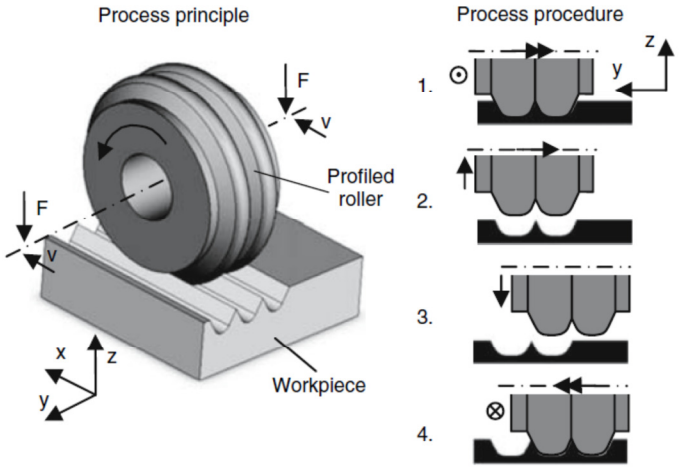

Figure 2.16: Principle of the incremental rolling process for producing defined riblet structures (Klocke and Feldhaus, 2007)

Wang et al. (2010) adapted the grinding process to the requirements of riblet production. They achieved high process efficiency by using multiple wheel profiles. They studied the influence of the dressing and grinding processes on the minimum producible riblet dimensions and on the structure quality (Figure 2.17). Riblets had dimensions between 20 and 120 µm. Metal bonded grinding wheels have been considered to achieve the required profile aspect ratio with a riblet width between 20 and 60 µm. In addition, an electro contact discharge dressing process (ECDD) was applied for the production of the wheel profile.

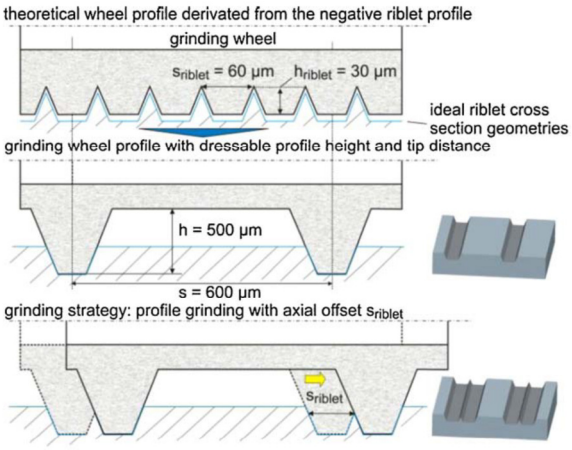

Figure 2.17: Wheel profile geometry and grinding strategy for riblet machining (Wang et al., 2010)

Gruneberger and Hage (2011) manufactured a riblet test surface with the rib spacing s = 0.15 mm with a paint application technique, that was developed by the Fraunhofer Institute for Manufacturing Technology and Applied Materials Research (IFAM) in Bremen, Germany. They produced this riblet structure on an aluminium plate for the oil-channel experiments. The paint material consists of a two-component polyurethane material modified with a UV-curable resin. The advantage of their work was that due to the flexibility of the silicone belt and of the soft guide rollers, paint application is possible even on curved surfaces. Figure 2.18 demonstrates the similar manufacturing method.

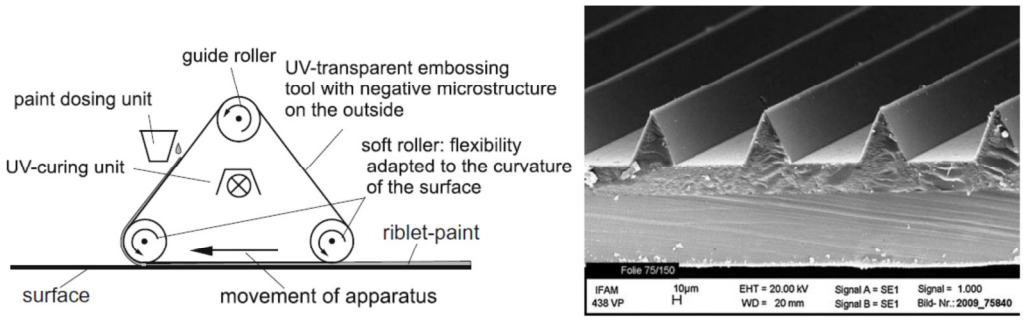

Figure 2.18: (a) Schematic of paint application apparatus, Stenzel (2009) (b) SEM picture of riblets fabricated with the paint application technique with rib spacing s = 0.15 mm; Stenzel and Hage (2009)

Another technique used for creating micro structure in order to reduce skin friction is Bio-Replication of Shark Skin (Han et al. 2010). For instance, Chen et al. (2013)

employed large-scale equal-proportional amplification bio-replication approach to adjust the micro-riblets of shark skin by taking solvent-swelling polymer as replica mould. The solvent-swelling property of polymer was studied by controlling its swelling ratio to make natural surface function adapting to various application environment.

Similarly Zhaoa et al. (2012) replicate shark skin surface with a vacuum casting method. They used fresh shark skin as a replication sample. The replication mold of shark skin was manufactured by casting the unsaturated polyester resin under vacuum and laying the multilayer glass fibers. After demolding, the replicated film of the shark skin with micro-riblets was achieved (Figure 2.19).

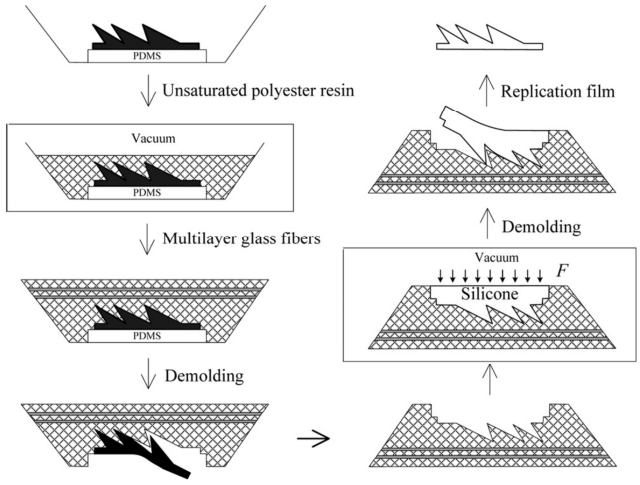

Figure 2.19: A sequential approach of micro-riblets replication (Zhaoa et al., 2012)

2.6 Conclusions

The chapter has presented a systematic review of micro-structured surfaces (riblets) that is highly associated with their effect on turbulent flow. Modelling work for performance as well as experiment and analysis techniques for performance characterization has also been surveyed. The review has revealed that the performance of riblets can be dramatically affected by their geometrical features. Some concluding remarks can be drawn, but not limited to:

- Knowledge revealed to optimal design of micro structures is relatively limited, including geometrical characteristics.
- Little is known about the mechanisms of the riblets and their interaction with flow.
- There is no effective approach of selecting simulation method with less computational cost.
- The manufacturing and production of micro-structured surfaces have not been developed properly, considering the challenge of having small sizes.

Chapter 3

Simulation based analysis and design of ribleted surfaces

3.1 Introduction

The effect of longitudinal riblet surface models (Semi-Circular and Serrate-Semi-Circular riblets) on a flat plate has been investigated numerically which involves examining drag reduction by solving the governing equations, the two transport equation (k-ε) model. The regimes for drag reduction in ribleted surfaces have been reviewed, with particular emphasis on the most effective shapes, and on the conditions under which that reduction increases (Walsh, 1978, 1980 and 1982). The results lead to the proposal of an alternative shape (Serrate-Semi-Circular riblets), together with analysis of the impact on the skin friction. The sizes have been carefully chosen based on the information from the literature review and modelling. Special attention has been given to the effect of the serration (angles) and cross section area (A_g) (García-Mayoral and Jiménez, 2011). The aim of this study is to find out about the effect of this newly designed shape (Serrate-Semi-Circular riblets). To achieve the aim, a well-known design (Semi-Circular riblet or U shape) is considered by way of comparison.

3.2 Theoretical model and numerical solution

The modelling was carried out to predict the drag reduction by riblets, in order to optimize the local skin friction (Figure 3.1) and the riblets effects were simulated using numerical modelling based on the finite volume method in the Cartesian coordinates system (x,y,z). Workbench FLUENT version (14.0) was used as the

Computational Fluid Dynamics Solver for the computer simulations and a three-dimensional numerical model was developed. The numerical simulation consisted of geometry creation, region specification, mesh generation, domains creation, boundary conditions assignment and (k-ε) equation solutions. The working fluid was air and the flow characteristics were Newtonian fluid as well as incompressible and turbulent flow.

Since these simulations were conducted with a RANS commercial solver, experimental data were required for very fine tuning of the coefficients in the mode and consequently, it was possible to capture the subtle modifications produced by the designed riblet geometries on the flow.

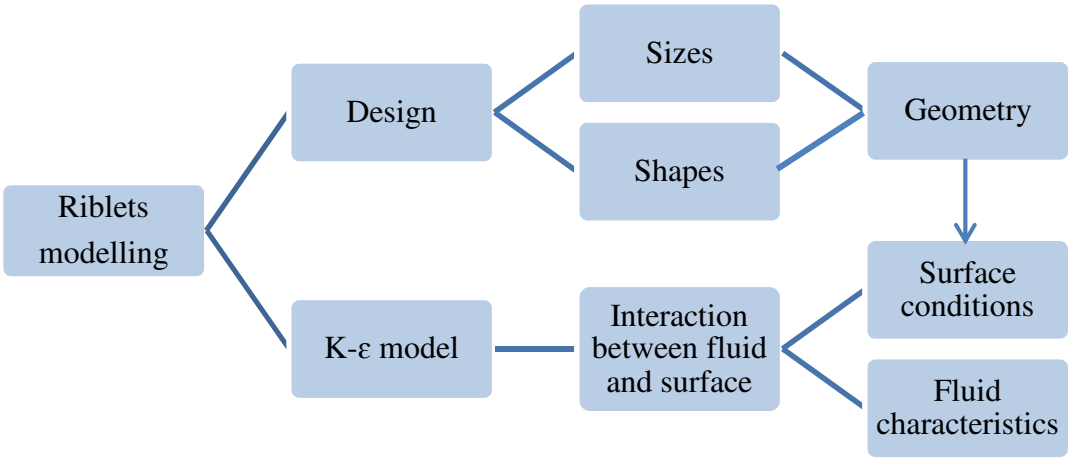

Figure 3.1: CFD modelling on ribleted surfaces

3.3 Geometry creation

In the simulation box, the upper wall was assigned as smooth and the ribleted surface was located at the lower wall. The depth of the computational domain was high enough to avoid its interference with the flow field and the sizes of this domain were L_z=1.06πδ (stream-wise), L_x=0.25-0.3πδ (span-wise) and L_y=2δ. By using this configuration, it was possible to achieve the corresponding results in one single simulation with minimum computational time (Jim´enez and Moin, 1991). δ is boundary layer thickness and is been defined in experimental trail on the smooth

surface. Table 5.1 in chapter 5 demonstrates this thickness in various positions. Different sizes of riblets for two shapes (Semi-Circular and Serrate-Semi-Circular) were created (Figure 3.2) and Tables 3.1 and 3.2 show the various scenarios that were modelled.

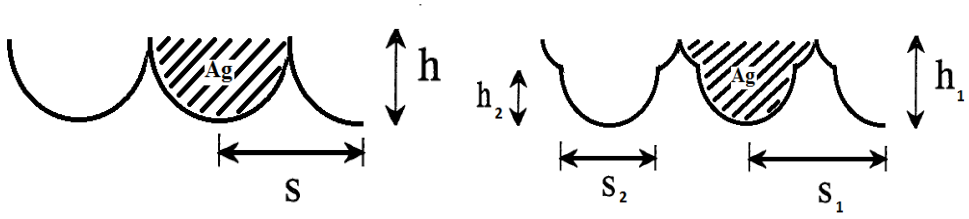

(a) (b)

Figure 3.2: (a) Semi-Circular riblets (b) Serrate-Semi-Circular riblets

Model	h(mm)	s(mm)
M.1	0.15	0.3
M.2	0.25	0.5
M.3	0.50	1.0
M.4	0.31	1.1

Table 3.1: Geometrical dimensions of the Semi-Circular riblets Sizes

Model	h_1(mm)	h_2(mm)	s_1(mm)	s_2(mm)
M.5	0.09	0.05	0.18	0.10
M.6	0.11	0.08	0.21	0.15
M.7	0.17	0.10	0.29	0.20
M.8	0.50	0.33	1.16	0.70

Table 3.2: Geometrical dimensions of the Serrate-Semi-Circular riblets Sizes

3.4 Mesh generation

In order to set up the mesh, the model geometry created in Design Modeller was moved into fluent-Mesh, i.e. the 'Standard meshing with Fluent-Mesh' option was used for meshing the ribleted section. In addition, the Delaunay Surface Mesher for

surface meshing and Advancing Front Volume Mesher for volume meshing were used. Since the ribleted surfaces have small wall size, the distributions of the mesh elements are poor in these locations. To avoid this problem and refine the mesh to a higher quality, surface proximity was used in these regions. Moreover, the Cut Cell method was used for the volume mesh generation in order to create periodic boundary in stream-wise direction. Additionally, with this method the grids can be relatively coarser in the region far from wall surfaces in order to save computational resources. Finally, in order to receive optimum results for skin friction on the riblets, surface sizing was selected.

An initial short study was undertaken to investigate the mesh quality and independency on the computational simulation. To this end, the mesh densities were varied from an initial number of 100s elements up to 4,931,117 in order to optimise the mesh density, achieve high mesh quality and obtain reasonable convergence. Information about the meshes specifications related to M.3 is shown in Table 3.3.

Study	S.1	S.2	S.3	S.4	S.5
R	100	100	100	100	100
PA	0.5	0.5	0.5	0.5	0.5
NCAG	5	5	5	5	5
PMS	45	40	40	35	30
FS	35	25	30	25	20
MAS	360	320	320	280	240
GR	1.08	1.09	1.08	1.10	1.10
MEL	3.5296e-005	3.5296e-005	3.5296e-005	3.5296e-005	3.5296e-005
Nodes	2383492	2810991	2998231	3519835	4931117
Elements	2235614	2627721	2817267	3269657	4591794

Table 3.3: Mesh specification with R: Relevance, PA: Proximity Accuracy, NCAG: Number Cells Across Gap, PMS: Proximity Min Size, FS: Face Size, MAS: Max Size, GR: Growth Rate, MEL: Minimum Edge Length (μM)

Trial runs were performed on the meshed geometry to check the size and quality of the meshes and also to investigate the mesh independency on a specific parameter of the computational domain. The above table demonstrates the mesh information

related to M.3 in order to show the mesh verification method. The pressure profile at the solid-fluid interface was used to investigate the drag reduction by the riblets. Because of conservation of energy in the computational solution this was found to be independent of the mesh density and therefore, pressure on a steeped drawn line along the test section was chosen as the convergence parameter. The line position has been chosen such that it demonstrates the fluctuations of the mesh densities. Figure 3.3 illustrates the location of the line.

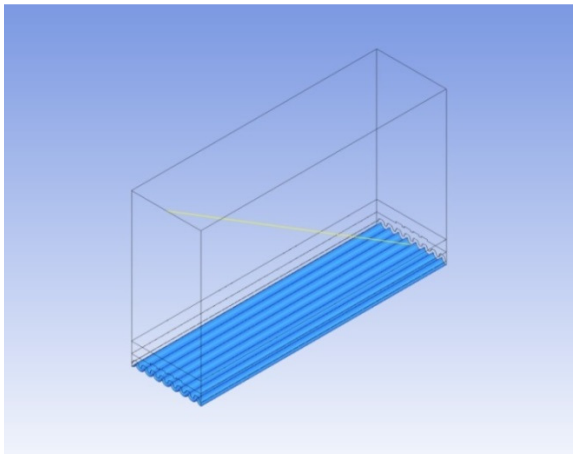

Figure 3.3: Line position for mesh verification

In total, five different trials were tested and compared. The variation of pressure along the line with the number of elements for two mesh densities of 3,269,657 and 4,931,117 is shown in Figure 3.4, but additional simulations are not shown.

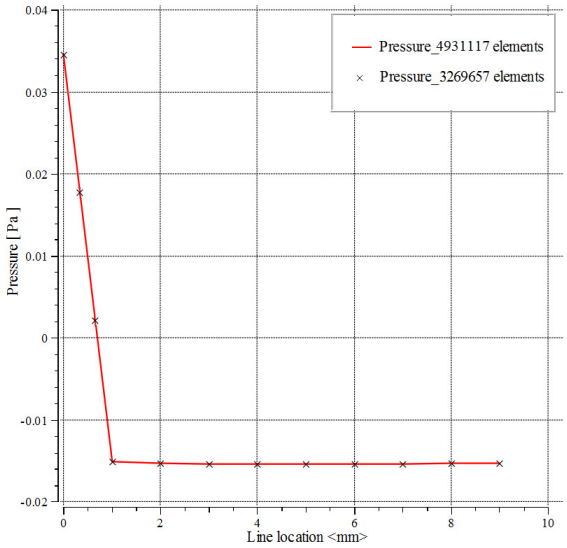

Figure 3.4: Mesh independence study; variation of central line pressure with number of elements

No change is observed in the obtained pressure distribution along the central line for these mesh densities, which demonstrates that the number of elements is sufficient for mesh independency in the computational simulation to be achieved. Therefore, in accordance with the high mesh quality and reasonable convergence time, 3,269,657 finite volumes were chosen as the optimal mesh density. Figure 3.5 illustrates the meshed geometry for the chosen number of elements and similar mesh verifications were carried out for other models as well.

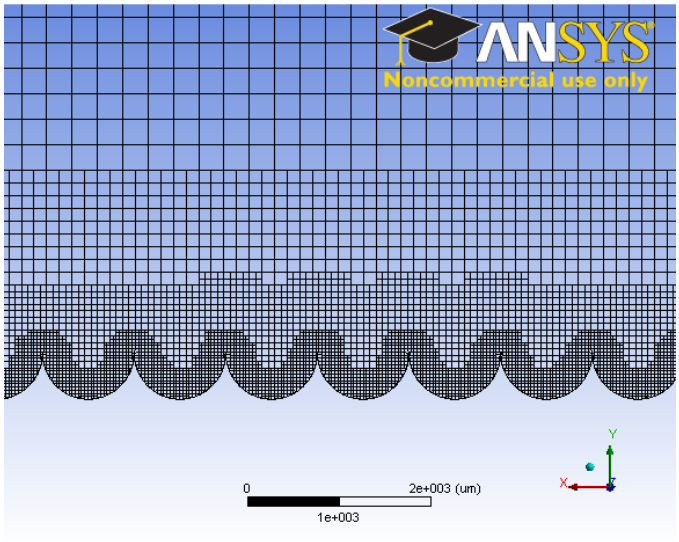

Figure 3.5: Mesh Geometry for 3,269,657 elements

In addition, as can be seen in Figure 3.6, the wall y+ value is between 1.15 and 2.50 (ignoring the anomalous at the inlet). Since this is less than 5, the near-wall grid resolution is acceptable.

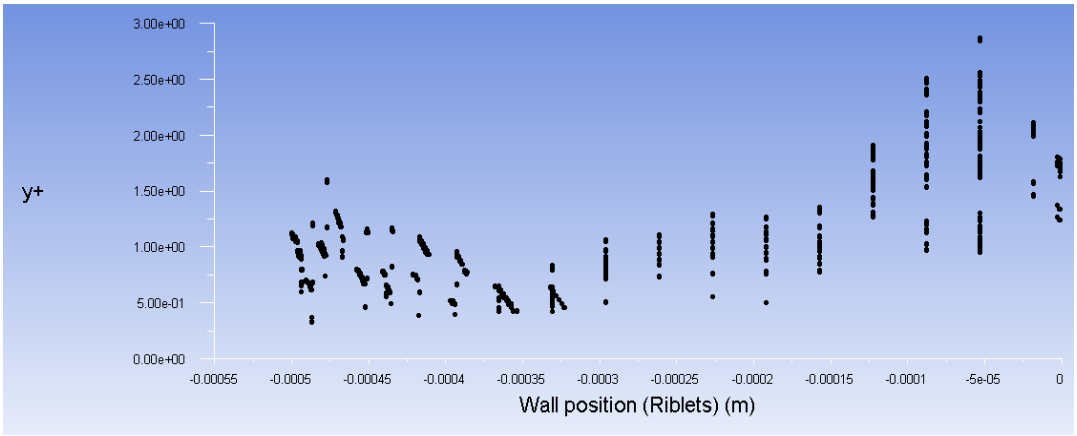

Figure 3.6: The wall y+ value on the riblets wall

3.5 Assignment of boundary conditions

After mesh generation, the meshed geometry was moved into the Fluent-Solution and subsequently, the boundary conditions were assigned for the specified domains (i.e. inlet, outlet, etc.). Since the unit cell is a 3D representation of the model, the boundary conditions are specified for the faces of the model with each face needing to be given one. The boundary conditions for numerical modelling were close to the experimental operating conditions, the locations of which are shown in Figure 3.7. The input data for the software were the atmospheric air properties with a mass flow rate of 30 m/s velocity. Since the simulations were conducted with a RANS commercial solver to capture the subtle modifications produced by the particular riblet geometry, Near Wall Function for wall roughness was used.

The input boundary conditions were as follows:

1) Inlet: the freestream flow ($U = U_\infty$)
2) Top channel wall: No-Slip and stationary wall (u, v, w, k, ε = 0)
3) Ribleted surface: No-slip condition with Near Wall Function for wall roughness
4) The rest of the model was symmetrical with periodic boundary conditions

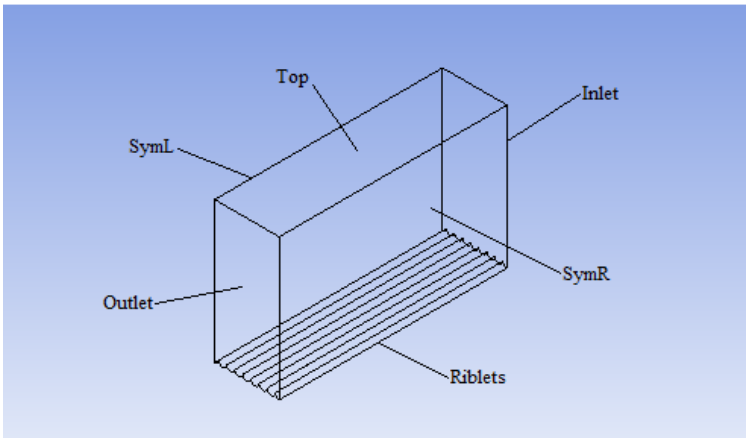

Figure 3.7: The location of boundary conditions, SymR and SymL: symmetry, Inlet and Outlet: periodic, Riblets and Top: stationary wall

3.5.1 Initialization

For wall-bounded flows in which the inlets involve a turbulent boundary layer, the Intensity and Length Scale method and the boundary-layer thickness, δ_{99} , were used to compute the turbulence length scale, L , from $L = 0.4\delta_{99}$. This value for L in the Turbulence Length Scale field was entered (i.e. for Re=3×10^5, δ_{99}=7.90 mm, L=3.16mm and for Re=8.26×10^3, δ_{99} =0.2516 mm, L=0.1mm). The turbulence intensity, I, is defined as the ratio of the root-mean-square of the velocity fluctuations, u', to the mean flow velocity,u_{avg} . A turbulence intensity of 1% or less is generally considered low and those greater than 10% are deemed high. Ideally, there should be a good estimate of the turbulence intensity at the inlet boundary from external, measured data. For example, when simulating a wind-tunnel experiment, the turbulence intensity in the freestream is usually available from the tunnel characteristics and in modern low-turbulence wind tunnels, the free-stream turbulence intensity may be as low as 0.05% (i.e. for Re=3×10^5, I is 3.307% and for Re=8.26×10^3, I is 5%).

3.5.2 Periodic boundary conditions

Periodic boundary conditions were assumed on the upstream and downstream domain boundaries and FLUENT provides the ability to calculate periodic flow. In such flow configurations, the geometry varies in a periodic manner along the direction for the flow, leading to a periodic fully developed flow regime in which the flow pattern repeats in successive cycles. These periodic conditions were achieved after a sufficient entrance length, which depended on the flow Reynolds number and geometric configuration.

Since the velocity profile is periodically repeating over ribblets in span-wise and stream-wise directions with an accompanying periodically constant pressure drop along the periodic length, a specified mass flow rate needed to be calculated and added to this modelling (Table 3.4).

$$M = \rho AV \tag{3.1}$$

where M is Mass flow rate (kg/s). ρ, A and V are density, Area and Velocity respectively.

Model	$A_g(\mu m^2)$	M (kg/s)
M.1	35325	0.004718
M.2	98125	0.005055
M.3	392500	0.005113
M.4	235718	0.005342
M.5	10290	0.004400
M.6	14494	0.004610
M.7	33564	0.004529
M.8	338987	0.005908

Table 3.4: Periodic boundary conditions with A_g ($L_g \approx A_g^{1/2}$) and M: Mass Flow Rate

3.5.3 Turbulence model (k-ε)

The k-ε models consist of two differential equations: one each for the turbulent kinetic energy k and turbulent dissipation ε. These two equations have to be solved along with the time-averaged continuity, momentum and energy equations. The standard (k-ε) model has two model equations: one for (k) and the other for (ε), which can be formulated from the following transport equations:

$$\frac{\partial}{\partial t}(\rho k) + \frac{\partial}{\partial x_i}(\rho k u_i) = \frac{\partial}{\partial x_j}\left[\left(\mu + \frac{\mu_t}{\sigma_k}\right)\frac{\partial k}{\partial x_j}\right] + G_k + G_b - \rho\varepsilon - Y_M + S_K \tag{3.2}$$

$$\frac{\partial}{\partial t}(\rho \varepsilon) + \frac{\partial}{\partial x_i}(\rho \varepsilon u_i) = \frac{\partial}{\partial x_j}\left[\left(\mu + \frac{\mu_t}{\sigma_\varepsilon}\right)\frac{\partial \varepsilon}{\partial x_j}\right] + C_{1\varepsilon}\frac{\varepsilon}{k}(G_k + C_{3\varepsilon}G_b) - C_{2\varepsilon}\rho\frac{\varepsilon^2}{k} + S_\varepsilon \tag{3.3}$$

In these equations, G_k represents the generation of turbulence kinetic energy due to the mean velocity gradients, whilst G_b is the generation of turbulence kinetic energy due to buoyancy, and Y_M represents the contribution of the fluctuating dilatation in compressible turbulence to the overall dissipation rate. S_K and S_ε are user-defined source terms. The remaining modelling constants have the following values:

$$C_{1\varepsilon} = 1.44, C_{2\varepsilon} = 1.92\ , \sigma_k = 1.0\ , \sigma_\varepsilon = 1.3 \tag{3.4}$$

where σ_k and σ_ε are the turbulent Prandtl numbers for k and ε.

Turbulent Kinetic Energy can be estimated from Turbulence Intensity. The relationship between the turbulent kinetic energy, k, and turbulence intensity, I, is:

$$K = \frac{3}{2}(U_{avg}I)^2 \tag{3.5}$$

where U_{avg} is the mean flow velocity (i.e. K=3.60375 for I=0.05% and K=36037.5 for I=5%)).

Also, the Turbulent Dissipation Rate (ε) can be estimated from a Length Scale (L):

$$\varepsilon = C_\mu^{3/4}\frac{K^{3/2}}{L} \tag{3.6}$$

where C_μ is an empirical constant specified in the turbulence model (approximately 0.09) and the determination of L was discussed previously (ε=355.698 for I=0.05% and ε=6157075690 for I=5%).

The turbulent viscosity ratio, $\frac{\mu_t}{\mu}$, is directly proportional to the turbulent Reynolds number. At the free-stream boundaries of most external flows, it is fairly small. Typically, the turbulence parameters are set so that $1 < \frac{\mu_t}{\mu} < 10$.

After setting up the simulation and boundary conditions assignment, the simulation was run as a steady state in the Fluent-Solver. Simulations were run using High Resolution methods and the Physical Timescale option was used for convergence control and the Energy equation in three-dimensions was solved for the volume mesh. To perform simulations of these models on a computer, these PDEs need to be discretised, resulting in a finite number of points in space at which variables, such as velocity and pressure, are calculated. The usual methods of discretisation, such as finite volumes, use neighbouring points to calculate derivatives, and so there is the concept of a mesh or grid on which the computation is performed. The main type of PDE used is elliptic, which is suitable for domains with closed boundaries.

3.6 Results and discussion

In order to verify the effect of turbulent boundary layer drag reduction over the ribleted surface, the skin friction coefficient (C_f) of the smooth surface is compared with the ribleted surfaces and the drag reduction efficiency (DR) is calculated using the following equation:

$$DR = \frac{C_{fsmooth} - C_{friblet}}{C_{fsmooth}} \times 100 \quad (3.7)$$

The shape of the riblet is an important factor affecting drag reduction over its surface. Table 3.5 illustrates the influence of the riblet shapes given in Table 3.1 and 3.2 on drag reduction. The results show that C_f at the riblet surface for M.2, M.5, M.6 and M.7 is smaller than the C_f at the flat surface. In the present study, maximum drag reduction of approximately 21% is observed for riblet case M.6. However, drag reduction is reduced to a negative value for the other riblet models, as shown in Table 3.5, which is due to the friction and break down of the drag reduction on the ribleted surface.

Model	$L_g(\mu m^2)$	Drag Reduction (%)
M.1	188	14
M.2	313	-0.07
M.3	626	8.6
M.4	484	-1.4
M.5	101	10
M.6	120	21
M.7	183	18
M.8	582	-0.5

Table 3.5: Results of the drag reductions, + and - denote the drag decrease and increase

In order to compare the selected model (M6) with the literature, dimensionless sizes are required (Table 3.6), which have been produced by skin friction velocity (u_τ) and kinematic viscosity (ν) from experimental data. The comparison is in section 5.5 (Chapter 5).

$$l^+ = \frac{lu_\tau}{v} \tag{3.8}$$

Model	h_1^+	h_2^+	s_1^+	s_2^+	$A_g^{+1/2}$
M.6	10.5	7.5	19.5	14	11

Table 3.6: The dimensionless sizes of model six

Considering Model 6 and 3, no apparent span-wise variation of the mean velocity is found above y⁄δ≈-0.1 and below y⁄δ≈0.05, as shown in Figure 3.8. The span-wise variation of the mean velocity occurs only very near the riblets for both shapes where, at a given y, the mean velocity above the riblet valley is larger than that above the tip. Similar observations for other type of riblets have also been reported in experimental and numerical studies (Hooshmand et al., 1983; Benhaliou et al., 1991; Bechert and Bartenwerfer, 1989).

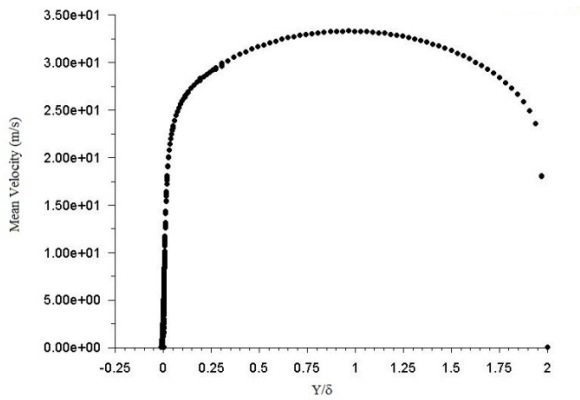

(a)

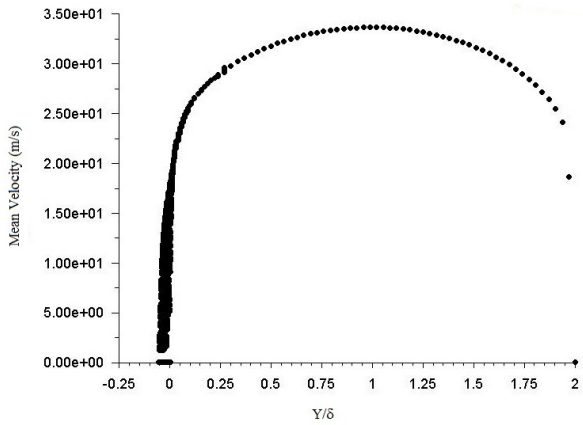

(b)

Figure 3.8: Span-wise variation of the mean velocity (a) M.6 and (b) M.3

Figure 3.9 shows the wall shear stress distribution for M.6 and it turns out that the smooth surface has a higher wall shear stress than the riblet surface for M.1, M.3, M.5, M.6 and M.7 (Appendix C). Additionally, it is observed that the shear stress of the smooth surface is almost constant along the stream-wise of plate and the average shear stress on the smooth surface is about 2.91 pa. From the figure, it can be seen that the shear stress of model 6 is smaller than the average value in the case with the smooth plate as shown in Appendix C.

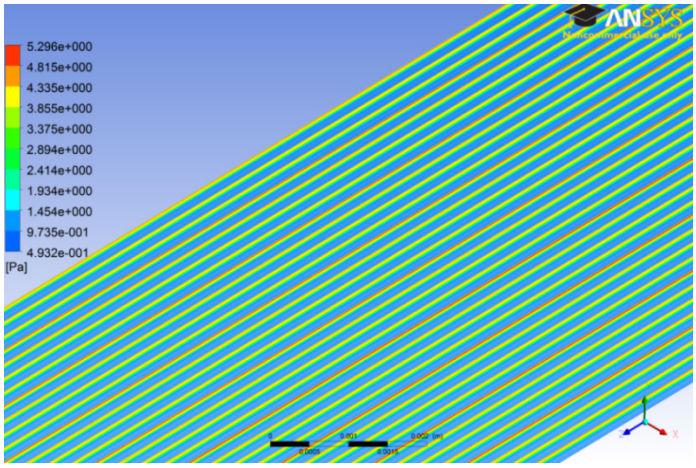

Figure 3.9: Wall shear stress distribution for M.6

As has been shown, in M.6, the shear stress and skin fiction have been decreased more than with the other models. In section 1.3, two possible different mechanisms for drag reduction by riblets have been discussed. Considering both theories, there is a possibility that the Serrate-Semi-Circular shape provides either more reduction in non-stream-wise momentum transfer compared with a Semi-Circular shape, or the ejection has been reduced and energy efficiency has been obtained. Considering the second theory, the selected shape (M.6) can reject vortices above the riblets better than the other modelled cases. In addition, as has been mentioned in literature review (2.1), the regions of high skin friction are associated with stream-wise vortices just above the wall. That is, the sweep motion because of these vortices creates high skin friction on the wall. With having serration inside the riblets, the chance of interaction inside the valley has been minimized due to creating riblets inside riblets, which affect the hairpin vortices over a wider range on the wall. Further experimental investigation, as presented in the following chapters, is needed to find the drag reduction mechanism of the designed riblet.

In addition, Garcia-Mayoral and Jimenez (2011) found that the groove cross section A_g^+ is a better characterization of drag reduction breakdown than the riblet spacing S^+ (see section 2.1). In this study, the riblets with similar spacing and height but different cross sections have been compared. For instance, M.8 and M.4 or M.7 and M.1 have almost the same maximum S and h, but due to having different shapes their groove areas are different and the one with $A_g^{+1/2}$=11 performs better in terms of drag reduction.

3.7 Conclusions

A reasonable method has been proposed to examine drag reduction by riblets. Drag reduction efficiencies have been analysed by comparing two kinds of different geometry shapes, Semi-Circular and Serrate-Semi-Circular. The presented exploration, made of a family of the newly designed riblets, according to the modelling predictions would give better performance than the usual Semi-Circular shape. Moreover, the results have shown that high drag reduction can be obtained with variations in their geometry and dimensions. That is, the best dimensions of the Serrate-Semi-Circular riblets that give a high reduction in drag are: s_1^+=19.5, s_2^+=14, h_1^+=10.5 and h_2^+=7.5.

Finally, the K-ε model has some disadvantages for their modelling. Regarding these, while the optimum drag reduction levels predicted in the study are broadly correct, there are nevertheless two substantial shortcomings in the computations: below h ~ 100 too little drag reduction is achieved, while for h > 150 too large reductions are indicated. This contrasting behaviour springs from two counteracting weaknesses in the model: an insufficient sensitivity to x-direction inhomogeneity on the level of ε and the use of an isotropic viscosity formulation that suppresses secondary motion (Launder and Li, 1993). This is the reason that in Table 3.5, the results for models M1 through M4 portrayed are slightly inconsistent with the results in the literature. In general, the findings in terms of comparison are accurate, although there might be different drag reduction predictions between the experimental and modelling results.

Chapter 4

Experimental methods

4.1 Introduction

The experimental facility, instrumentation and measurement techniques used in the present investigation are described in this chapter. This study concerns the measurement technique for deriving the skin friction and boundary layer structures, under a turbulent channel, from the velocity profile and pressure fluctuations. Recent measurements of good quality, using pitot tubes, hot-wire (single and cross-wire probes) and automated traverse, were used to assess critically, and then to improve the experimental accuracy of, the empirical coefficient and the determination of the surface shear and skin friction. In addition, microphones were embedded in the model to characterise, in detail, the unsteady pressure fluctuations on the surface of the plates under different boundary layer regimes, especially with the presence of riblets.

4.2 Experimental setup

The experimental set-up consisted of a flat plate (considered as a smooth surface), a ribleted plate, an open-circuit wind tunnel, the sensing instrumentation, and data-acquisition systems. The major objective of these experiments was to examine skin friction for the hydraulically smooth and fully ribleted surface.

4.2.1 Wind tunnels

The experiment was conducted in the Brunel University Department of Mechanical Engineering vertical blower wind tunnel as shown in Figure 4.10 and the

dimensions of the test section are 150mm × 50mm. The plates were fixed to the bottom side of the test section and while the maximum speed inside this can reach approximately 35 m/s, the base flow was chosen as 30 m/s. This tunnel also has a filter at the inlet to remove dust and dirt particles in order to minimise hot-wire contamination and breakage. Sandpaper was used to trigger the boundary layer into turbulence artificially. The location which was carefully chosen, such that the Reynolds number based on the displacement thickness was greater than 520 so as to ensure a rapid transition into a turbulent boundary layer, which occurs on the plates at zero angle of incidence. This is often referred to as a canonical zero-pressure turbulent gradient boundary layer. Moreover, the calibration wind tunnel was used for hot wires calibration (Figure 4.1).

Figure 4.1: Wind tunnel in the Aeronautic Lab at Brunel University used for calibration

4.2.2 Smooth and ribleted surfaces

The plates employed in the current investigation were made of aluminium 6082 and the flat plate roughness has been measured by a TESA/ZEGO microscope, being found to be less than 0.5 μm. The dimensions of both plates are 295mm × 150mm × 5mm (Figure 4.2 shows the flat plate) and the new design of the riblets has been milled on the flat plate (The CAD design for the micro featured plate is in Appendix D). Table 4.1 summarises the shape characteristics and note that there is no flow at the back of the test plates. Additionally, a small bevel angle is present near the trailing edge at the back.

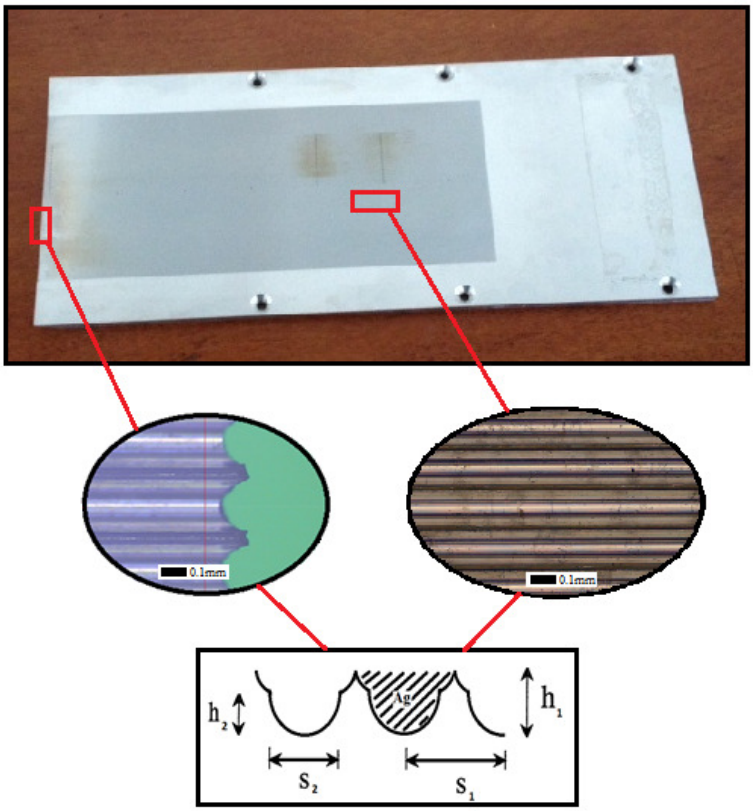

Figure 4.2: Serrate-Semi-Circular riblets (from TESA)

Model	h_1 (mm)	h_2 (mm)	s_1 (mm)	s_2 (mm)
M.6	0.108	0.75	0.210	0.150

Table 4.1: The sizes of Serrate-Semi-Circular riblets

4.2.3 Machining process and techniques

The optimised design has a Serrate-Semi-Circular riblet (Figure 4.2), which proved to be efficient in reducing surface friction through numerical simulation and an area of 200mm×100mm was required to be covered with the optimised structure, for which 500 Serrate-Semi-Circular grooves had to be manufactured.

Micro-milling tools which meet such demand should have a diameter below 150µm, however, previous experience indicates that this is quite challenging for micro tungsten carbide milling tools given the actual feedrate and depth of cut for each tool path employed during real machining. Besides, such tools, being so small

in diameter, will be very vulnerable and subject to machining process instability, thus resulting in premature tool fracture.

To avoid such problems, fly-cutting was conducted to generate these repetitive structures. The idea of fly-cutting is to attach the tool cutter at the end of the cylindrical shank (Figure 4.3); the rotational axis is perpendicular to the cutter, not collinear with the tool's geometrical axis as in micro-milling. Thus it is possible to increase the rotational diameter of the cutting tool significantly and have a much faster cutting speed. Moreover, the cutting tool can be manufactured with a low aspect ratio, and this could highly improve the tool's strength and durability. In addition, the tool shank can guarantee that the tooling system has sufficient stiffness to resist the force and deformation caused by the interaction of the cutting tool and the material. Finally, in fly-cutting we can increase the feedrate to quickly improve machining efficiency quickly with the surface quality controlled within the tolerance range.

Two specially designed small cutters made of CVD diamond have been ordered and instrumented to a 10mm tool shank (Figure 4.3). The first cutter has a diameter of 300µm in order to generate the upper semi-circle of the structure, and the second's diameter is 150µm so as to produce the lower semi-circle of the structure, as shown in Figure 4.3.

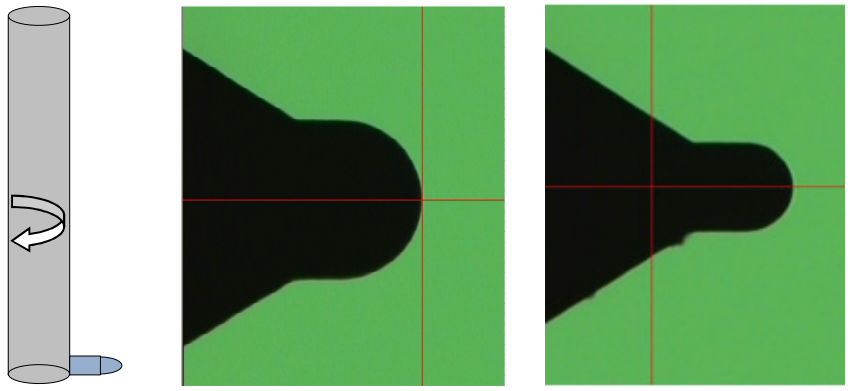

(a) (b) (c)

Figure 4.3: (a) Fly-cutting tooling system (b) 300µm diameter CVD tool (c) 150µm diameter CVD tool

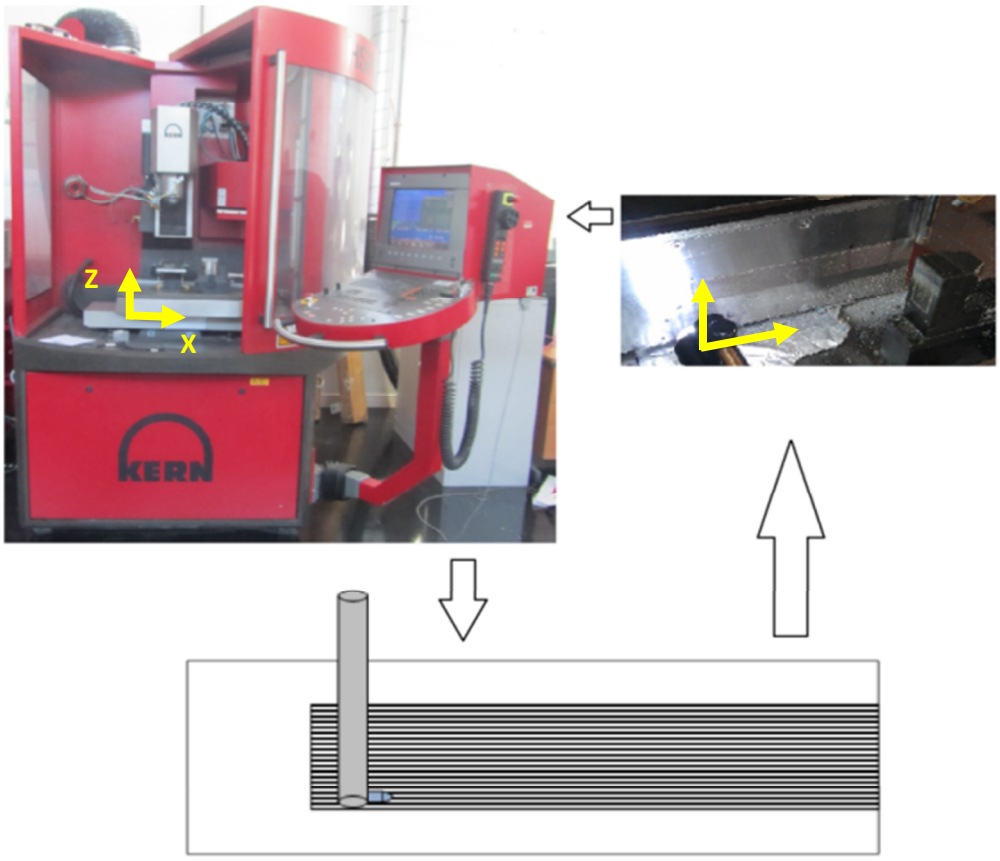

Figure 4.4: Mirco-milling machine, workpiece and diagram of machining set-up

Manufacturing was conducted on a 5-axis ultra-precision micro-milling machine, KERN HSPC, which has a machining volume of 280mm×250mm×250mm and it has a motion accuracy of better than 0.1µm on each translational axis. A ceramic bearing-supported spindle is instrumented with maximum a speed of 33000rpm.

In order to machine the workpiece as closely to the designed geometry as possible, several criteria were predefined: flatness error of the whole plate should be within 2µm; the dimensional accuracy of the structures should be within ±3µm and the surface finish is required to be less than 1µm.

The diagram of the machining set-up is shown in Figure 4.4. The workpiece is mounted on the machine vertically, and adjusted carefully to be parallel with the XOZ plane of the machine coordinate within an error of 5µm. As the CVD cutting tool spins with the cylindrical shank, it also travels along the direction of the structures. Once one structure is machined, the tooling system retracts and moves up by 210µm which is the size of pitch shown in Figure 4.2. Afterwards, the tool

was plunged in and engaged with the workpiece, then it starting to manufacture the next structure.

The machining is divided into two stages: the first employs the 300µm CVD tool to remove material quickly and machine the upper semi-circle of the structure, then the 150µm CVD tool is substituted and used to complete the rest of the machining, including the final surface finishing. During the two stages, the spindle speed is set to be 6000rpm, the 300µm and 150µm CVD tools both have a rotational diameter of 28mm, and the spindle run-out is controlled to within 5µm.

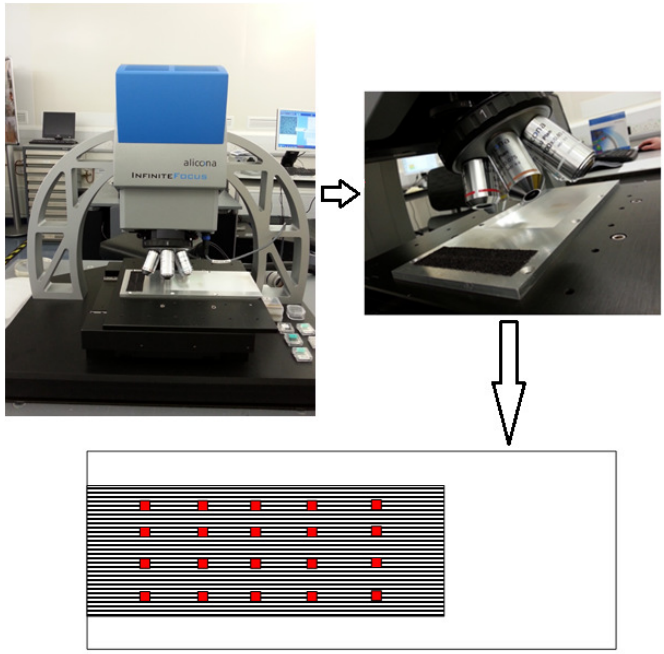

Figure 4.5: Measurements with Alicona 3D profiler with Lens 10X and the Measurement areas indicated by red squares, with dimensions 1.4mm×1.09mm

After the machining, the measurement is carried out on an Alicona 3D profiler to find the accuracy of the manufacturing process; 20 measurement locations are collected in order to assess the machining quality of the whole area and each location has an area of 1.09mm×1.4mm, as shown in Figure 4.5. The dimensional measurement shows good agreement between the designed and actually machined geometry (Figure 4.6). that is, the distances between peaks are all at 210µm with a tolerance of ±2µm and the depth of each riblet is around 107.7µm, which thus shows good machining accuracy (Appendix D, Figure 4 and 5) (AMEE, Brunel University and NPL, 2013).

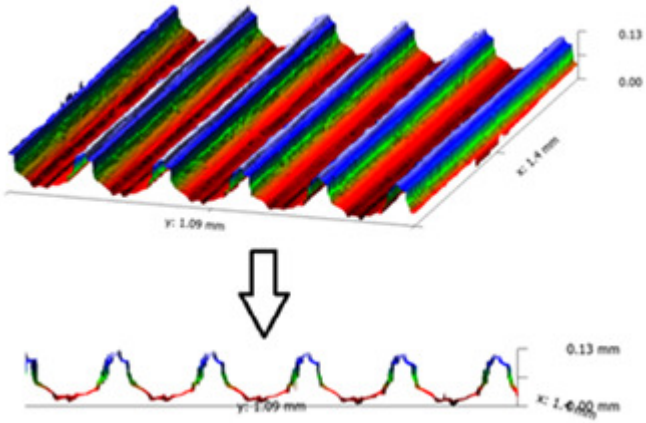

Figure 4.6: 3D profile of machined riblets and cross-section structures as measured with Alicona

4.2.4 Measurement instrumentation and techniques

Three different probes, namely, a pitot probe, single hot-wire and cross-wire, were used to measure the velocity fields in the turbulent boundary layer (Figure 4.9). A pitot probe was used to measure the mean stream-wise velocity, while the hot-wires were used to measure the fluctuating velocity components across the boundary layer at a section 150 mm (downstream) from the leading edge.

In addition, static pressure tappings of ≈ 0.5 mm were drilled onto the plates' surfaces, thereby allowing measurements of the static pressure and hence, the calculation of the static pressure coefficient distribution. The microphones selected for the unsteady surface pressure measurements have been 426E01 from PCB PIEZOTRONICS (Figure 4.7). The sensing area has been embedded in the plates under a pin hole of 4.5 mm diameter in order to minimise attenuation effects at high frequencies due to the finite size of the microphones. The dimensions of the pin hole configuration and microphone position are depicted in Figure 4.8.

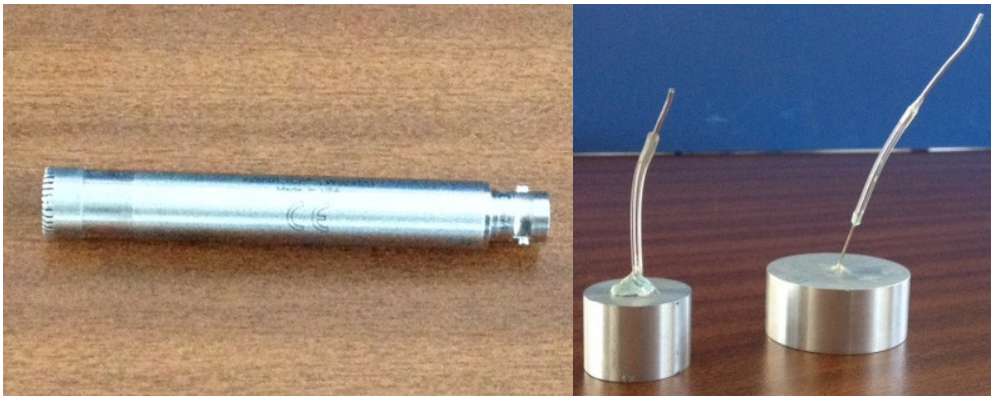

(a) (b)

Figure 4.7: (a) Microphone 426E01 from PCB PIEZOTRONICS (b) Microphones tubes and tubes' holders

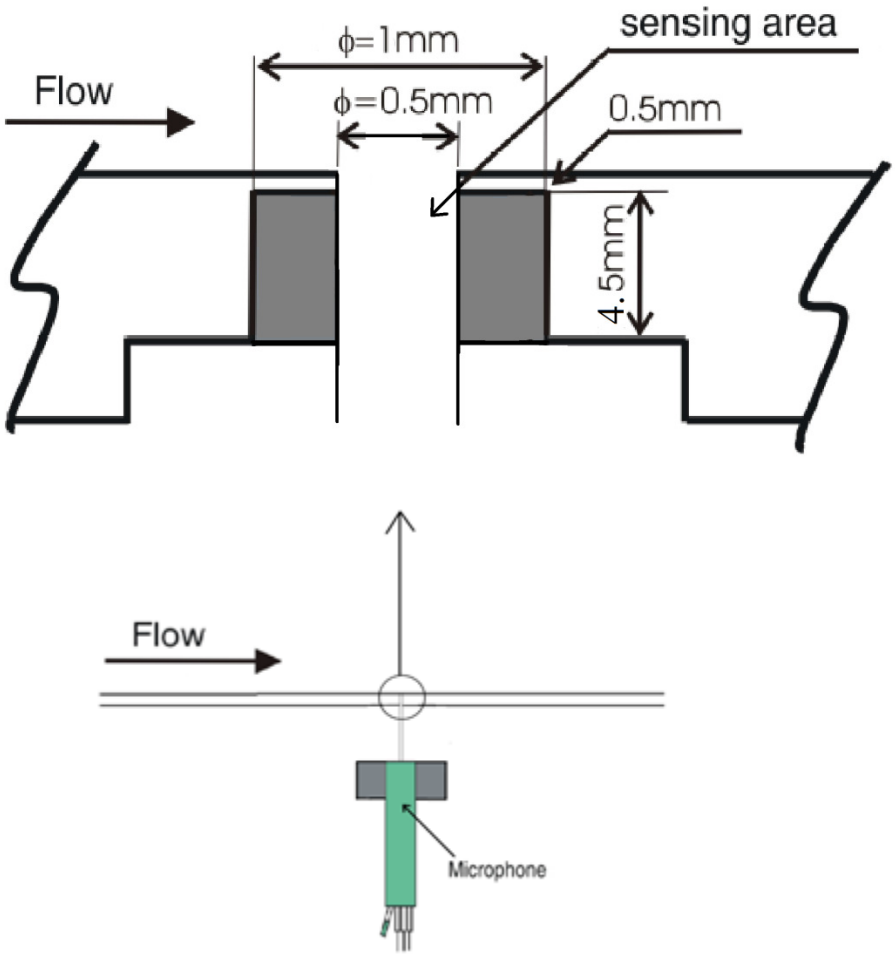

Figure 4.8: Dimensions of pin hole configuration and microphone position

A single hot wire probe was used to measure the boundary layer profiles at the surface of the plates. More specifically, a DANTEC 55P11 constant-temperature single hot-wire probe was operated with a TSI IFA-100 anemometer at an over-heat ratio of 1.8. The Intelligent Flow Analyzer (IFA) had three channels, which enabled voltage output from three wires simultaneously and the probe was connected to the first channel. The recommended operating resistance and bridge compensation were set on the IFA as given by the TSI. Moreover, the sensor of the hot-wire probe, made of platinum-plated tungsten wire, had an outside probe support diameter of 3.8mm and a length-to-diameter (l/d) ratio of about 335, which was large enough to avoid conduction errors.

In order to determine the turbulence structure on the plate surface a miniature type cross-wire (DANTEC 55P61) was used to measure the two-component velocity fluctuations u and v. The diameter and length for each wire were 5 μm and 1.25 mm respectively. The cross-wire was operated at an overheat ratio of 1.6 and it was found that the "cross-talk" between each wire at low speed due to the natural thermal convection was not very significant. A full velocity versus yaw-angle calibration technique was employed (section 4.3) to convert the acquired voltages into the velocities (Browne, 1989). This calibration method eliminated the potential error incurred by the different sensitivity of the yaw coefficients to the velocity. The data was sampled for cross-wire at a frequency of 40 kHz for approximately 10 seconds at each point by a 24-bit A/D card (TSI ADCPCI). Due to the physical size of the cross-wire, the nearest point in the boundary layer was approximately 1 mm from the wall. The probe was attached to a computer controlled two-dimensional traverse system (Vathylakis and Chong, 2013).

Figure 4.9: Single hot-wire and cross-wire

The signals from the single hot wire were acquired at 20 kHz, after passing through a 10 kHz anti-aliasing filter. The digitized voltage from the hot wire was then converted to velocity by interpolating the 4th-order polynomial velocity-voltage calibration curve. Because all of the flat plates were reflecting aluminium, the vertical distance of the hot wire probe with respect to the wall surface can be determined accurately with the aid of a travelling microscope. Additionally, a trip strip made of sand paper (36-d grit) was placed across the width of the top of the plate and the trip strip was 30 mm wide, being located 25 mm from the leading edge. This was used in all the experiments in order to maintain consistent development of the turbulent boundary layer. The use of a strip of roughness was also shown by Klebanoff and Diehl (1951) to provide effective boundary layer thickening and a fairly rapid self-similarity.

The measurements were taken using an automated traverse in the vertical (y), stream-wise (x) and span-wise (z) directions, with a displacement accuracy of 0.01mm, 0.01mm and 0.1mm, respectively. The traversing machine allows for 3-D placement of measurement probes and can position a thermal probe or pitot tube at any (x, y, z) position and is controlled by the stepper motor. The operation of the stepper motor uses the Thermalpro software on the computer**.**

The data logging was controlled by a PC running Thermalpro (5.00.10) software. Voltages were acquired using a National Instruments Data Acquisition DaqBoard/3005 card, which consisted of a 1-MHz A/D with 16-bit resolution. In addition, a National Instruments BNC-(18806-66) connector panel was used in

conjunction with the data acquisition board and BNC cables were connected to the input channels of this panel. Moreover, the flow temperature was measured with a Digimate FM10 thermometer.

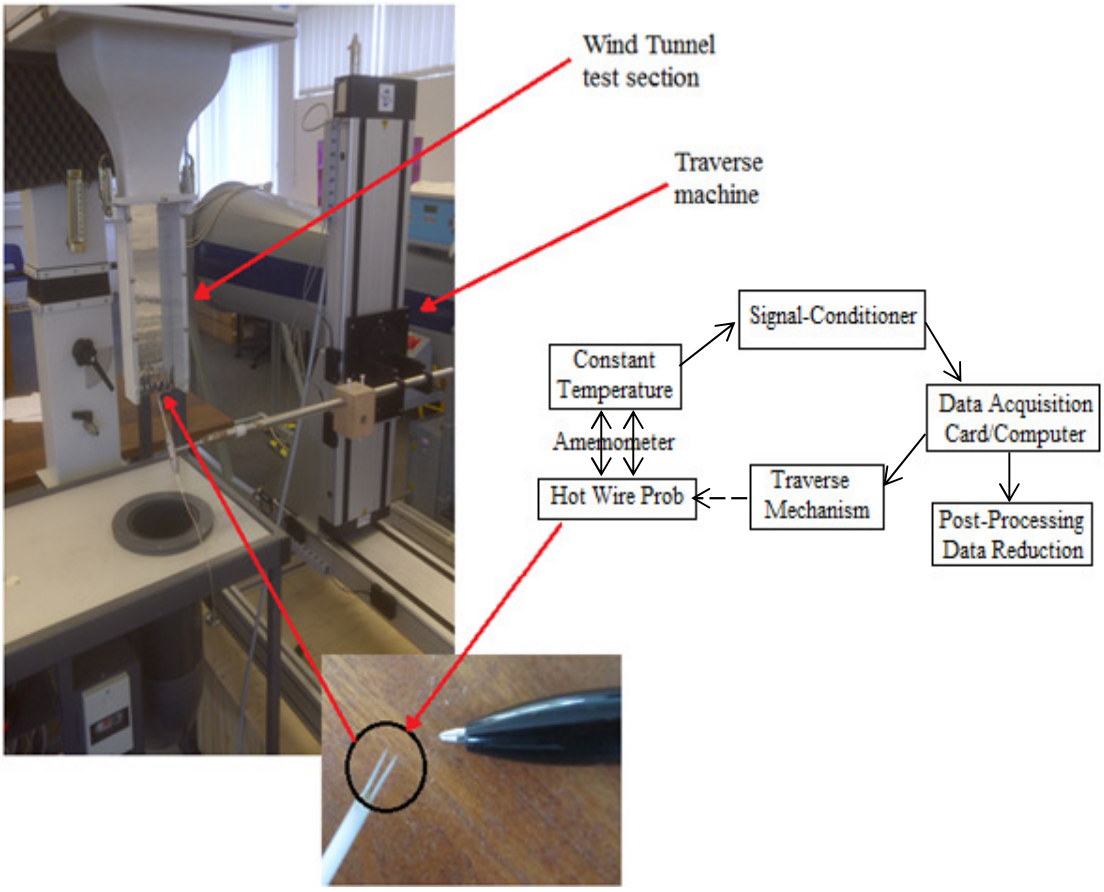

Figure 4.10: Experimental testing setup by using wind tunnel (Air Flow Bench AF10) and hot-wires data logging system

The collected data from acquisition card in the first step was reduced by Thermalpro. Second, the mean and root mean square (rms) of the velocity data in order to calculate the velocity profiles have been calculated as:

$$U_{mean} = \frac{1}{N}\sum_{i=1}^{N} U_i \tag{4.1}$$

$$u_{rms} = \sqrt{\frac{1}{N}\sum_{i=1}^{N}(U_i - U_{mean})^2} \tag{4.2}$$

where N is the total number of samples in the velocity time series. The rms is a measure of the amount of deviation of a signal data from its mean value and is computed as the square root of the variance.

The Reynolds shear stresses were calculated from the cross-wire measurements as:

$$-\overline{u'v'} = \sqrt{\frac{1}{N}\sum_{i=1}^{N}(U_i - U_{mean}).(V_i - V_{mean})} \quad (4.3)$$

4.2.5 Outline of the surface hot-wire and microphone array

There are about 70 microphone sensing holes across each of the plate models, each being 0.5 mm in diameter and 0.5 mm deep (Figure 4.8), and is followed by a recess hole inside the flat plate of 1 mm diameter. The depth of the recess holes are different, depending upon the location with respect to the trailing edge. These holes are to hold a small metal tube of 0.5 mm internal diameter, and the metal tube is connected to a plastic tube as part of a remote microphone system (to be discussed in the next section). As shown in Table 4.2, these sensing holes are named individually. This configuration allows for the wall pressure power spectral density (PSD) and stream-wise, span-wise and oblique coherence functions to be compared directly among different position on riblets and flat plates. In Figure 4.11, the surface microphone arrays for models are illustrated. Note that the black dots represent the location of the pin holes but do not correspond to their actual size (0.5 mm). The exact positions of the two microphones pin holes on the plates are summarised in Table 4.3. In addition, Table 4.4 demonstrates the positions of microphone and cross-wire on the plates for cross correlation.

	1	2	3	4	5	6	7	8	9	10	11	12	13	14	15	16	17	18	19	20
A	A1																			
B	B1	B2	B3	B4	B5	B6	B7	B8	B9	B10	B11	B12	B13	B14	B15	B16	B17	B18	B19	B20
C	C1	C2	C3	C4	C5	C6	C7	C8	C9	C10	C11	C12	C13	C14	C15	C16	C17	C18	C19	C20
D	D1																			
E	E1																			
F	F1																			
G	G1	G2	G3	G4	G5	G6	G7	G8	G9	G10	G11	G12	G13	G14	G15	G16	G17	G18	G19	G20

Table 4.2: Distributions of the microphone sensing holes on smooth surface studied here. Same arrangement applies to ribleted plate

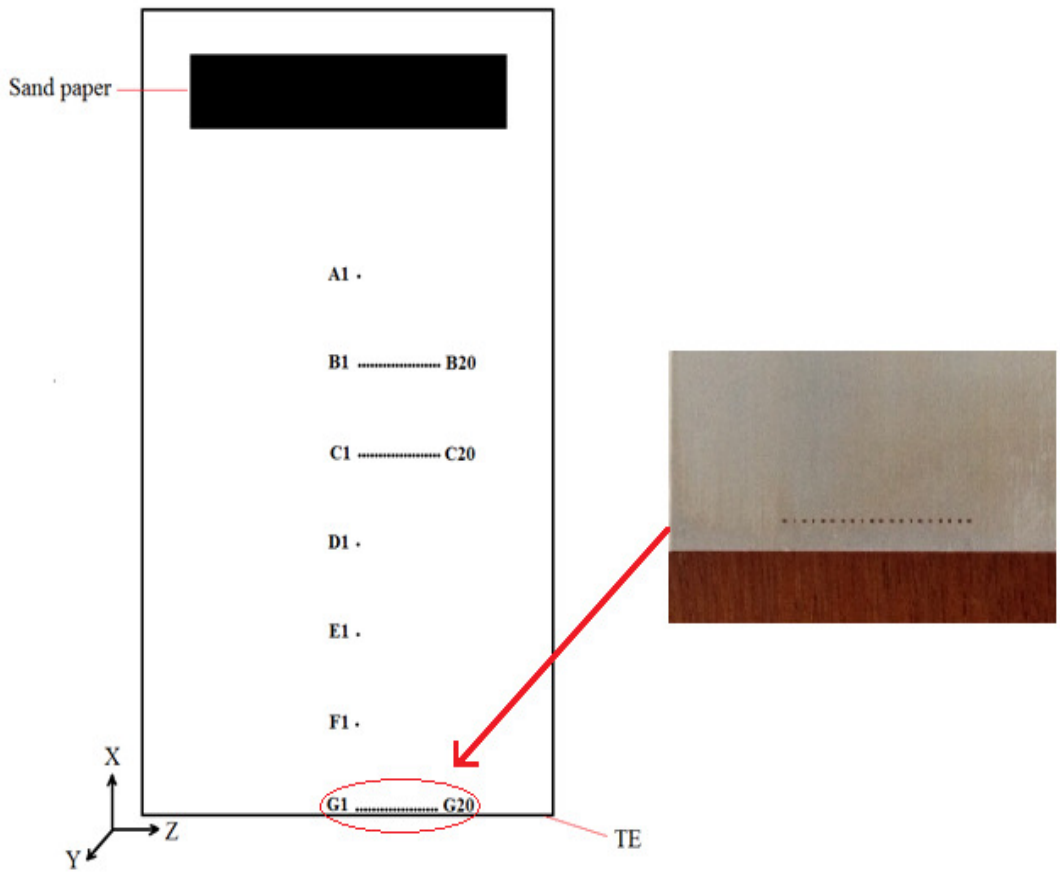

Figure 4.11: Surface microphone arrays for both models investigated, the system of coordinates indicated in

Number of microphones positions	MIC A position	MIC A Distance from TE, x (mm)	MIC B positions	MIC B Distance from mid span, z (mm)
1	A1	183	B1,C1,D1,E1,F1,G1	0
2	B1	153	C1,D1,E1,F1,G1	0
3	C1	123	D1,E1,F1,G1	0
4	D1	93	E1,F1,G1	0
5	E1	63	F1,G1	0
6	F1	33	G1	0
7	G1	3	G2-G20	[1.3,26], z+1.3
8	B1	153	B2-B20	[1.3,26], z+1.3
9	C1	123	C2-C20	[1.3,26], z+1.3

Table 4.3: Positions of two microphones in the smooth and ribleted plates

	1	2	3	4	5	6	7	8	9	10	11	12	13	14	15	16	17	18	19	20
A	A1																			
B	B1	B2	B3	B4	B5	B6	B7	B8	B9	B10	B11	B12	B13	B14	B15	B16	B17	B18	B19	B20
C	C1	C2	C3	C4	C5	C6	C7	C8	C9	C10	C11	C12	C13	C14	C15	C16	C17	C18	C19	C20
D	D1																			
E	E1																			
F	F1																			
G	G1	G2	G3	G4	G5	G6	G7	G8	G9	G10	G11	G12	G13	G14	G15	G16	G17	G18	G19	G20

Table 4.4: Green blocks highlighting the positions of microphone and cross-wire in the smooth and ribleted plates

The single hot wire position has been calculated by an Excel file for automated traverse and for each model the minimum numbers of 7×47×25 (x (stream-wise), z (span-wise), y) positions have been considered. The distance between the location in span-wise direction is 1 mm, in the stream-wise direction is 4 mm and on the longitudinal direction, y, is arranged nonlinearly according to the closeness to the surface.

4.2.6 Remote microphone arrangement

Two ½ inch condenser microphones were used to measure the *PSD* of the wall pressure from several distributed sensing holes (0.5 mm diameter), as seen in Figure 4.11. A small sensing hole was necessary in order to maintain the spatial resolution of the measured pressure and to minimize the attenuation of eddies with small wavelength. The microphones were connected to the sensing holes via a remote system. However, an initial attempt to measure the surface pressure by a probe-tube arrangement with a side-branch and an infinite tube ending was not successful due to the poor signal to noise ratio (Franzoni and Elliott, 1998). Instead, a more traditional, yet simpler design of the probe-tube arrangement was adopted. As shown in Figure 4.8, the microphone is always positioned directly underneath the sensing hole so that a straight line of sight can be drawn from the centre of the sensing hole, via a straight plastic tube of 0.5 mm internal diameter and 20 mm long, and into the centre of the microphone. Owing to the minimal sudden area variation along the tube duct, and the relatively short plastic tube, strong acoustic resonance in the form of a standing wave is not expected to be too significant in this particular remote arrangement. This is confirmed in Figure 4.12,

which shows an example of the measured wall pressure *PSD*. Because the test plates essentially act as a wind tunnel floor, there is a large degree of freedom in positioning the remote microphone system outside of the wind tunnel in order to ensure that a straight line of sight between the sensing hole and the microphone is always maintained. The remote microphone arrangement also allows the wall pressure measurements to take place relatively close to the plates' surfaces.

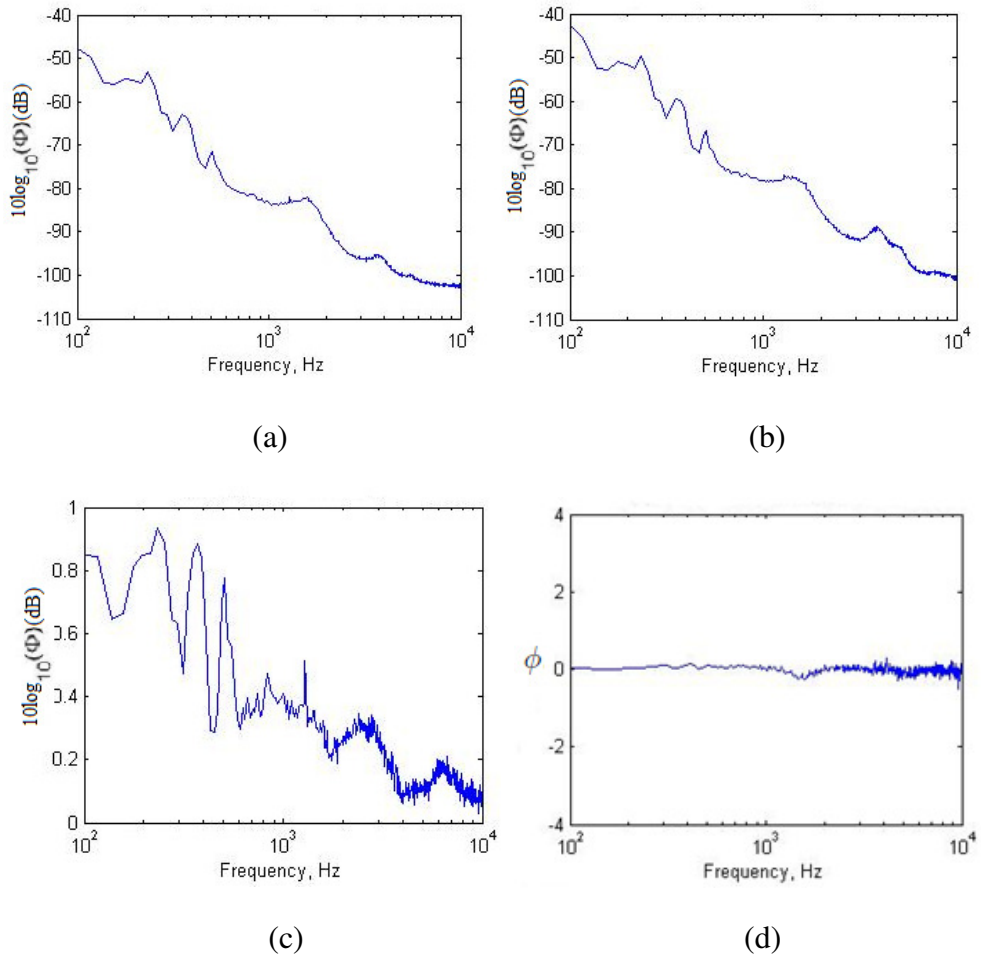

Figure 4.12: An example of wall pressure power spectra density (PSD) measured by two remote microphone sensors at points G1 and G2, Ø is phase angle (rad): (a) power spectral density of microphone A (b) power spectral density of microphone B (c) Coherence of microphones A and B (d) phase angle between microphones A and B

In this study no magnitude calibration of the two microphones was performed either in the free field condition or in the remote configuration. Considering that one of the main objectives was to investigate the difference in wall pressure *PSD*

levels among the different positions on the riblets and flat plate, an absolute magnitude level was not considered to be necessary. Moreover, phase calibration between the two microphones had been performed in a small anechoic chamber at Brunel University, both of which were exposed to a loudspeaker driven by a white noise signal input. Good coherence between the microphone signals was obtained and the phase angles were generally small within a wide frequency range. During the acquisition of unsteady wall pressure by the microphones, the sampling frequency and sampling time were set at 40 kHz and 10 seconds, respectively. The digitization of the analogue signals was performed by a 24-bit National Instrument A/D card. Finally, the wall pressure data was windowed-FFT (4096 point) and averaged to obtain the *PSD* with a resolution of 1 Hz bandwidth (Vathylakis and Chong, 2013).

4.3 Hot-wires calibrations

Figure 4.1 shows the wind tunnel used for the calibration. Each sensor was calibrated in free-stream flow before and after each profile or each set of data points was measured. If these two calibrations were in disagreement by more than 2-3%, or if the calibration error was more than 0.01, the entire process was repeated.

The single-wire probe was calibrated in situ against a pitot-static one over a range of 22 freestream velocities outside the boundary layer and the voltage signal from the anemometer was stored together with the freestream velocity. The calibration curve used for the experiment was a fourth-order polynomial expressed as follows:

$$U = C_1 + C_2E + C_3E^2 + C_4E^3 + C_5E^4 \tag{4.4}$$

where U is the mean velocity, C_1 to C_5 are constants to be determined and mean E is the voltage output from the anemometer. The mean velocity, U, was determined through the relationship:

$$P_{tot} - P = \frac{1}{2}\rho U^2 \tag{4.5}$$

Using a pitot-static probe to measure the dynamic pressure, where P_{tot} is the total pressure, P is the static pressure, and ρ is the density of air. The density could be determined accurately by measuring the static pressure and temperature. A typical single-wire calibration curve is shown in Figure 4.13.

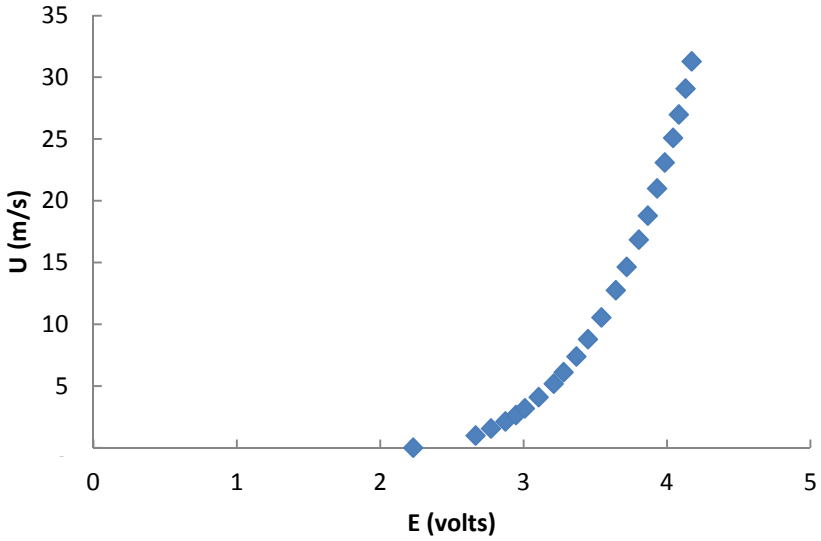

Figure 4.13: Single-wire calibration curve

Cross-wire has similar calibration process except for angle of attacks (AOA). Twelve different AOAs have been selected for calibration, which was carried out by changing the yaw angle of the XW probe over a certain range in a known velocity (magnitude and direction) flow and recording the output of the wires at every angle. The probe was calibrated in situ over a range of different wind-tunnel speed settings in the core region of the calibration wind tunnel using a pitot-static probe, which was oriented such that the binormal velocity component, i.e. the velocity component perpendicular to both wires, was equal to zero and the angles a_1 and a_2 were both equal to 45°(Figure 4.14). At a fixed freestream velocity, the angular position of the probe was varied between – 45 and +45 degrees at a constant increment of 8 degrees from -40 to +40. This procedure was repeated at 22 different freestream velocities. In addition, two dimensional third-order polynomials were fitted to the voltage data to give response equations for the velocity magnitude and the yaw angle (Österlund, 1999 and Bruun, 1995). A

typical cross-film probe calibration map is shown in Figure 4.14. The stream-wise and wall-normal velocities were obtained from the equations:

$$u = U_0 cos\alpha \tag{4.6}$$

$$v = U_0 sin\alpha \tag{4.7}$$

where U and V are the stream-wise and wall-normal velocity components, respectively, and α is the probe angle of attack. Two variables, x and y, denoting the stream-wise and cross stream velocity components, were determined from the wire voltages $E_1$and E_2 as follows:

$$x = E_1 + E_2 \tag{4.8}$$

$$y = E_1 - E_2 \tag{4.9}$$

The two variables were then used to obtain two two-dimensional third-order polynomials, given by:

$$U_0 = a_1 + a_2 x + a_3 y + a_4 x^2 + a_5 xy + a_6 y^2 + a_7 x^3 + a_8 x^2 y + a_9 xy^2 + a_{10} y^3 \tag{4.10}$$

$$\tan\alpha = b_1 + b_2 x + b_3 y + b_4 x^2 + b_5 xy + b_6 y^2 + b_7 x^3 + b_8 x^2 y + b_9 xy^2 + b_{10} y^3 \tag{4.11}$$

The above equations were solved using a least square method, to determine the coefficients a_1 to a_{10} and b_1 to b_{10}, which were then stored and used in the experiments to determine the instantaneous velocities, U and V (Akinlade, 2005).

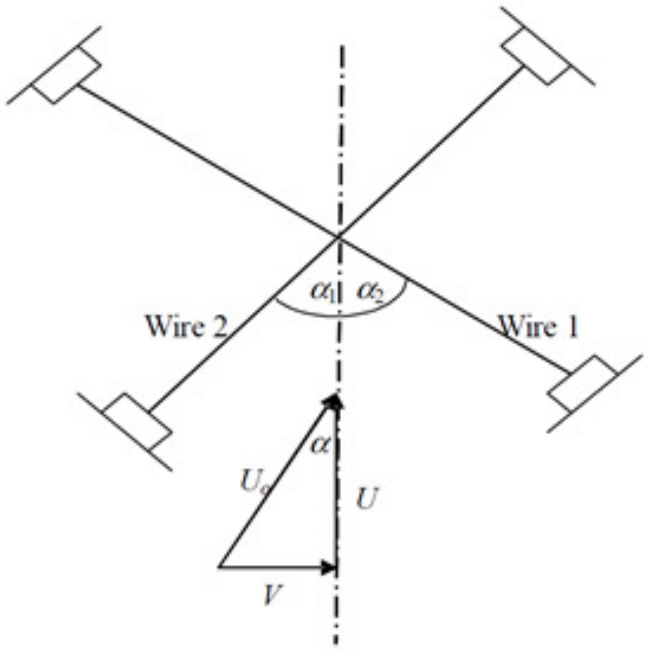

Figure 4.14: The definition of the yaw angle in the plane of the probe

4.4 Estimation of the experimental uncertainty

Measurement errors are broadly classified into systematic (fixed errors) and random errors. It is difficult to establish errors in experiments where there is not a sufficient number of samples (repetitions of the experiment) and furthermore, the "true" value of the measurement might not be known. An uncertainty analysis provides a reasonable alternative to determine the data quality. Precision uncertainty estimates for the velocity measurements were made through repeatability tests, with four replicate velocity profiles being taken on both the smooth and the ribleted surfaces. The systematic error, which represents the bias uncertainty, was obtained from the instrumentation used in the measurements, which have been mentioned in 4.2.4. The estimated bias errors were combined with the precision uncertainties to calculate the overall uncertainties for the measured quantities. One of the well-known methods for estimating uncertainty as used by Coleman and Steele (1999) is presented in Appendix B (Garcia Sagrado, 2007 and Akinlade, 2005). The other method used in this context presented by Kline and McClintock (1953) examines the derivative of the equation that relates an unknown

quantity (Z) to measured variables (X,Y). The maximum uncertainty can then be calculated by adding the appropriate uncertainty terms, e.g.:

$$Z=f(X,Y) \tag{4.12}$$

$$\partial Z = \left[\left(\frac{\partial f}{\partial X}\middle|\partial X\right)^2 + \left(\frac{\partial f}{\partial Y}\middle|\partial Y\right)^2\right]^{1/2} \tag{4.13}$$

where ∂X, ∂Y and ∂Z are the uncertainties associated with X, Y and Z respectively. In order to calculate ∂Z, ∂X and ∂Y must be known a priori from previous evaluations, instrument specifications or experience. In Tables 4.5 and 4.6, uncertainties related to various instruments employed during this investigation are summarised. These values have been used to calculate the uncertainties of "derived flow parameters" by taking the derivative of the corresponding physical equation in a similar way as in equation 4.13 (Garcia Sagrado, 2007).

Parameter	Device	Typical value	Random error	Uncertainty $(\partial X/X)$ %
Pressure	Microphone	Up to ≈250 Pa	±1.25 Pa	±0.50
Ambient Pressure (Absolute)	Barometer	101300 Pa	±10 Pa	±0.01
Temperature	Thermometer	300 K	±1	±0.33
Coordinate (position x, y, z)	Automated Traverse	30,30,6(mm)	±0.01, ±0.01, ±0.1 (mm)	±0.03, ±0.03, ±1.6

Table 4.5: Uncertainties associated with various measuring devices

Parameter	Typical value	∂Z	Uncertainty %
Density (kg/m^3)	1.2	±0.004	±0.33
Inlet velocity (m/s)	30	±0.1	±0.33

Table 4.6: Uncertainties associated with derived quantities

4.5 Conclusions

The described experimental methods are the path leading to a large matrix of data for velocity profile and turbulence quantities that encompass hydraulically smooth and riblet regimes. The following chapters are concerned with the analysis and discussion of the obtained data.

Chapter 5

Modifications of TBL characteristics through smooth and micro-structured surfaces

5.1 Introduction

In this chapter, first, boundary layer profiles along the plates, smooth and ribleted surfaces, are investigated and comparisons are made with their mean velocity profiles, root-mean-square (rms) velocity profiles, and boundary layer integral parameters. These proposed results have been obtained by single hot wire measurements and careful analysis has been undertaken on ensemble averaged velocity (single hot-wire) and their spectra. In addition, MATLAB (R2011b) has been used for all the data analysis.

5.2 Boundary layer integral parameters and shape factors

In this section, the integral parameters associated with the different boundary layer regimes are presented.

The boundary layer thickness δ has been calculated from the analysis of the mean velocity profiles, which is defined at the point where the velocity is 99% of the freestream velocity, defined as U_{99}.

In this study, the freestream velocity at the inlet of the test section has been measured at a distance of 22 mm from the leading edge. In addition, because of the effect of the side walls which grows towards the LE, the inlet velocity is 1.9 % lower than the outlet velocity. The presented results in this chapter have been measured at the middle of the test section, and the freestream velocity has been

used to normalise the data. In addition, due to the effect of the wall, the selected positions have been chosen at the mid span.

Figures 5.1, 5.2 and 5.3 show the mean velocity profiles for the flat plate and riblet models at x=48, 56 and 64 (mm), respectively. According to the classical theory of turbulence, the direct effect of any structured surface on the flow is a shift in the mean velocity profile, provided that the manipulations do not protrude into the flow a distance comparable to its thickness, which can be observed in the following figures. In addition, in the next sections, it is explained that the friction is actually derived from this shift with elemental algebra (Garcıa-Mayoral, 2011).

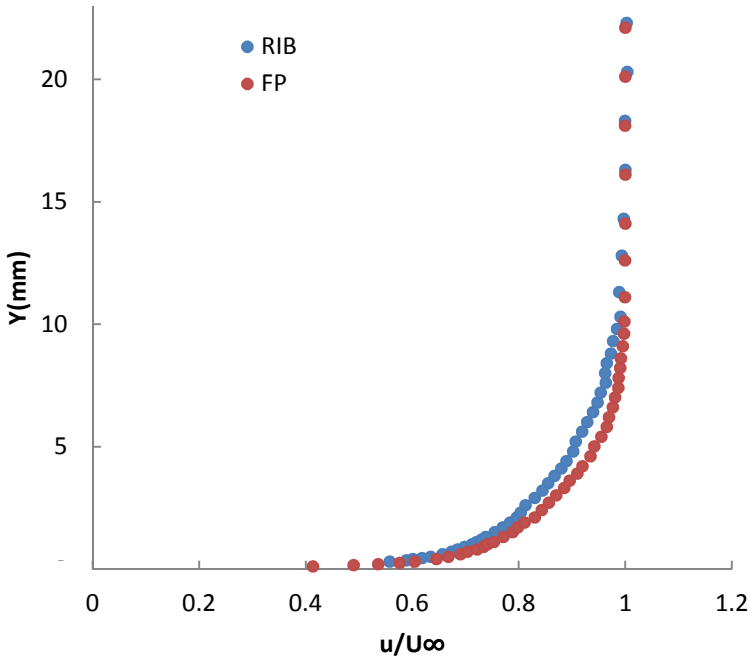

Figure 5.1: Boundary layer mean velocity profiles at x=48(mm) positions in the mid span-wise over the riblets and flat plate

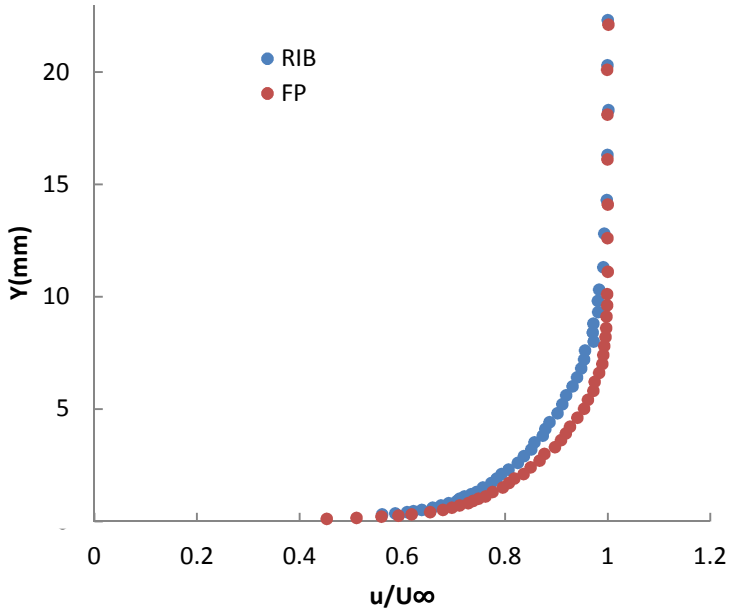

Figure 5.2: Boundary layer mean velocity profiles at x=56(mm) positions in the mid span-wise over the riblets and flat plate

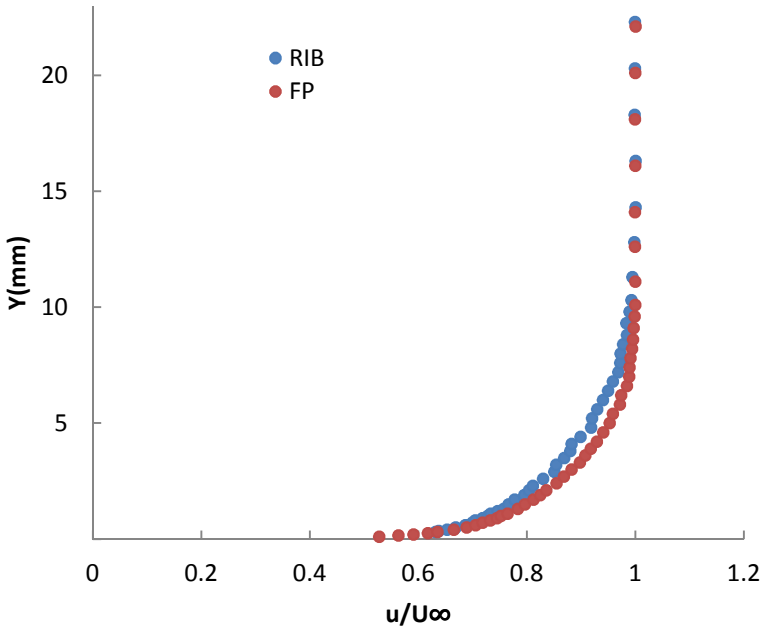

Figure 5.3: Boundary layer mean velocity profiles at x=64(mm) positions in the mid span-wise over the riblets and flat plate

5.2.1 Smooth and ribleted surface boundary layers

The displacement thickness δ_1 and the momentum thickness δ_2 are defined in equations 5.1 and 5.2 below.

$$\delta_1 U_e = \int_{y=0}^{\infty} (U_e - u) dy \tag{5.1}$$

$$\delta_2 U_e^2 = \int_{y=0}^{\infty} u(U_e - u) dy \tag{5.2}$$

In Table 5.1, the integral parameters at different stream-wise positions_upstream and downstream of the flat plate_are presented. The shape factor H_{12} is defined as the ratio between δ_1 and δ_2. The velocity at the position of the boundary layer thickness, $U_{99} = 0.99U_\infty$, has also been included in the table; and U_∞ presents the freestream velocity. The presented results in Table 5.1 is obtained from the data in the middle of the test section for various span-wise positions.

It can be seen that on smooth surface, the integral parameters are similar for the range of Re studied (Walsh, 1989) and the values of the shape factor H_{12} are almost typical of a TBL, going from 1.260 to 1.270 (Schlichting, 1979) for smooth surface. The shape of the profiles together with the values of the shape factor H_{12} confirms the existence of a TBL over both surfaces.

Position (z) (mm to mid span)	δ (mm)	δ_1(mm)	δ_2 (mm)	H_{12}	U_{99}(m/s)
-3.00	7.7	0.9129	0.7241	1.260	25.8793
-2.00	8.7	0.9774	0.7715	1.266	26.3703
-1.00	7.0	0.8763	0.6908	1.268	27.0310
0	8.1	0.9544	0.7510	1.270	26.7420
1.00	7.5	0.8584	0.6863	1.250	26.7974
2.00	7.7	0.8906	0.7085	1.257	26.8150
3.00	8.1	0.9557	0.7540	1.267	26.8076

Table 5.1: Integral parameters in the model with the smooth surface for Re=1.42×10^5; Boundary layer thickness, δ, and U_{99} being considered in middle of the test section (x=48 mm)

Position (z) (mm to mid span)	U_∞(m/s)	C_f
-3.00	26.1347	0.0045-0.0046
-2.00	26.6467	0.0044-0.0045
-1.00	27.3029	0.0044
0	27.0170	0.0044
1.00	27.0662	0.0044-0.0045
2.00	27.0854	0.0045-0.0046
3.00	27.0799	0.0045-0.0046

Table 5.2: Freestream velocity and skin friction in the model with the smooth surface, considered in middle of the test section

In Table 5.2, the skin friction coefficient (C_f) and freestream velocities of the test section are shown for the smooth surface. The method used to calculate C_f is described in section 5.4 and the skin friction coefficient can be found by $C_f = \frac{2\tau_w}{\rho {U_e}^2}$. In addition, Figure 5.11 presents C_f for the five different positions on stream-wise and to define C_f the wall shear stress τ_w is needed which is indicated as:

$$\frac{d}{dx}(U_e^2\delta_2) + \delta_1 U_e \frac{dU_e}{dx} = \frac{\tau_w}{\rho} \tag{5.3}$$

The friction velocity can be found by wall shear stress as follows:

$$u_\tau = \sqrt{\frac{\tau_w}{\rho}} \tag{5.4}$$

Position (z) (mm to mid span)	δ (mm)	δ_1(mm)	δ_2 (mm)	H_{12}	U_{99}(m/s)
-3.00	10	1.1710	0.9503	1.232	25.9721
-2.00	10	1.1550	0.9350	1.235	26.2833
-1.00	9.5	1.1929	0.9649	1.236	27.1075
0	9.2	1.1439	0.9210	1.242	26.6978
1.00	10	1.0847	0.8889	1.220	27.3961
2.00	9.5	1.0525	0.8617	1.221	27.7515
3.00	9	1.0152	0.8340	1.217	27.3960

Table 5.3: Integral parameters in the model with the ribleted surface for Re=1.42 × 10^5; Boundary layer thickness, δ, and U_e being considered in middle of the test section (x=48 mm)

Position (z) (mm to mid span)	U_∞(m/s)	C_f
-3.00	26.2971	0.0042
-2.00	26.6081	0.0041-0.0042
-1.00	27.4629	0.0041-0.0042
0	26.9972	0.0041-0.0042
1.00	27.7011	0.0042-0.0043
2.00	28.0609	0.0042
3.00	27.7043	0.0042

Table 5.4: Freestream velocity and skin friction in the model with the smooth surface, considered in middle of the test section

In Table 5.3, the integral parameters and shape factor H_{12} at different stream-wise locations are presented for boundary layers of the riblet surface. In Tables 5.1 and 5.3, the displacement thickness δ_1 and momentum thickness δ_2 for the riblets boundary layer cases can be seen to increase significantly compared with the smooth surface. The value of H_{12} for the riblets is approximately 1.220 and 1.242 for the lowest and highest respectively. It should be noted that in Tables 5.2 and 5.4, the skin frictions have also been presented for comparison. The obtained results show the effect of riblets on decreasing skin friction and consequently drag. It can be seen that the skin friction on the ribleted plate has been reduced by 7% on average when compared to the flat one. In addition, the experimental error and high intensity inside the channel create the variation in the results.

Study	Riblet Shapes	s^+	h^+	Modelling Method	Drag Reduction
Choi (1993)	V	20	17.3	S (DNS)	6%
Walsh (1982)	V	12	12	E	4%
Crawford (1996)	V	20.41	17.70	S(DNS)	5%
Walsh (1982)	U	16	8	E	4%
Park & Wallace (1994)	V	28	14	E	4%
Present study	υ	19	11	E	≈7%

Table 5.5: Optimized riblet's sizes founded in literature; S: simulation, E: experiment

The drag reductions for different studies have been presented in Table 5.5. The drag variations are also similar to several incompressible results. In terms of

comparison, with V and U shape riblet geometries, the experiments by Walsh (1982) reported a drag reduction of 4% for s+ ≈ 20, and for the DNS by Choi (1993) this was around 6% for s+ ≈ 20.

5.3 Boundary layer mean and root-mean-square velocity profiles

In this section, the velocity profiles, contour plots and flow visualizations are presented for both plates' boundary layer cases and the profiles are shown at various locations. Moreover, a comparison between the velocity profiles for smooth surface and riblets is made. In Figure 5.4 the boundary layer mean velocity profiles and in Figure 5.5 root-mean-square velocity profiles normal to the surface over the flat plate are presented.

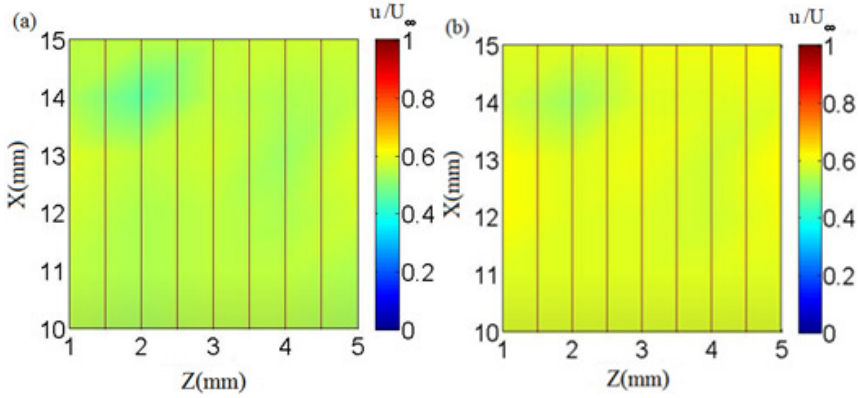

Figure 5.4: Boundary layer mean velocity profiles (u) contour plots normal to the plate over the smooth surface, x: stream-wise (5 positions) and z: span-wise (5 positions), a) y=0.3mm b) y=0.4mm

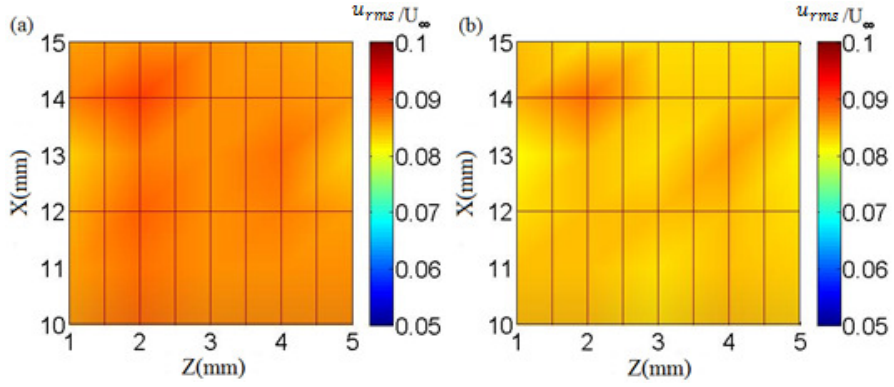

Figure 5.5: Boundary layer root-mean-square velocity profiles (u_{rms}) contour plots normal to the plate over the smooth surface, x: stream-wise (5 positions) and z: span-wise (5 positions), a) y=0.3mm b) y=0.4mm

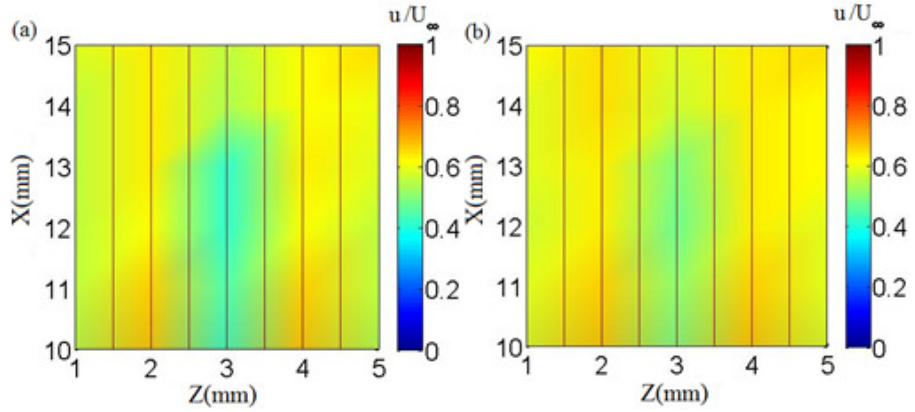

Figure 5.6: Boundary layer mean velocity profiles (u) contour plots normal to the plate over the riblets, x: stream-wise and z: span-wise, a) y=0.3mm b) y=0.4mm

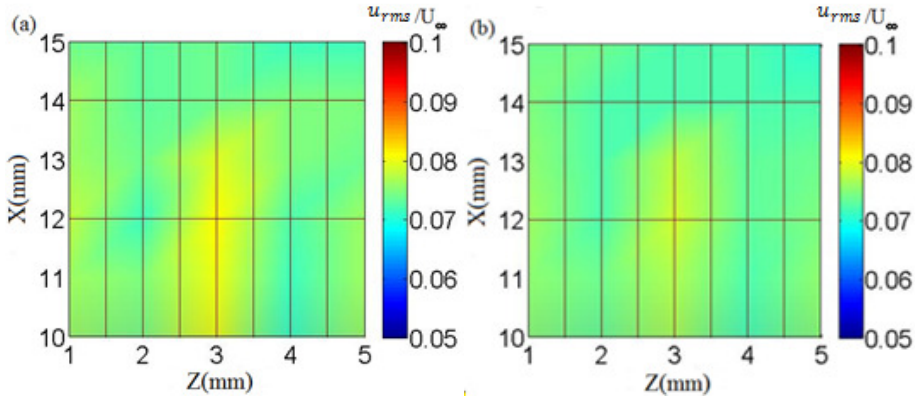

Figure 5.7: Boundary layer root-mean-square velocity profiles (u_{rms}) contour plots normal to the plate over the riblets, x: stream-wise (5 positions) and z: span-wise (5 positions), a) y=0.3mm b) y=0.4mm

The above Figures 5.6 and 5.7 in this section and Figures 5.1, 5.2 and 5.3 demonstrate the change in velocity profiles in the presence of riblets. Although the mean velocity profiles contour has a small change for the riblets when compared to the smooth surface, the root-mean-square velocity profiles contour shows a significant decrease for the former that is not apparent for latter. A large u_{rms} indicates a higher level of turbulence. Physically, the turbulence level correlates with the shear, such that a lower turbulence level leads to lower shear and consequently less friction.

5.4 Skin friction coefficient calculation and log-law representation

The value of the skin friction coefficient C_f has been determined by following a method similar to that of Clauser (1954). For a given Mach number (in this study M=0.1), Allen and Tudor (1969) proposed a chart with a family of curves of u/U_e versus yU_e/v with C_f as the varying parameter. Using a single hot wire allows the measurements inside the Buffer layer ($5 < y^+ < 30$). By plotting the experimental profile on the chart, the skin friction coefficient could be obtained by interpolating between the C_f curves. In Figure 5.8, the experimental profiles at different positions along the flat plate and riblets are shown.

In Figure 5.9, the experimental profiles at different positions in the middle of the test section along the riblets plate and flat plate are illustrated. An overall 7% skin friction reduction on the riblets is observed when compared to the smooth surface. However, owing to experimental errors there are fluctuations in these results. In addition, the measurements on the riblets took place in different geometrical position of grooves. These differences are due to the vortices formed above a riblet surface which remain there, interacting with the tips only and rarely causing any high-velocity flow in the riblet valleys. Since the higher velocity vortices interact only with a small surface area at the riblet tips, only this localized area experiences high shear stresses. The low velocity fluid flow in the valleys of the riblets produces very low shear stresses across the majority of the surface of the riblet (Lee and Lee, 2001). Therefore, in general the skin friction on this type of structured surfaces is low compared to smooth surfaces.

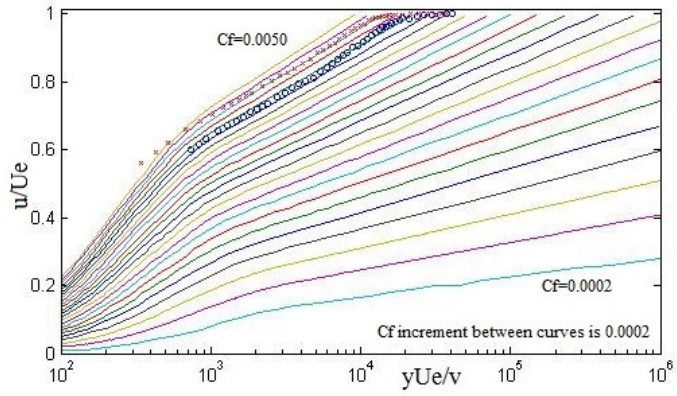

(a)

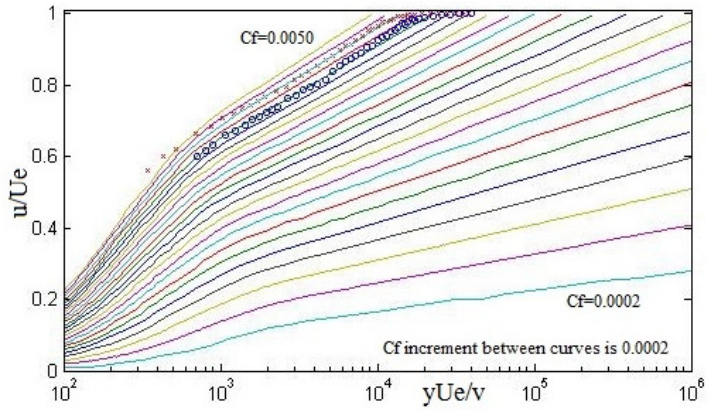

(b)

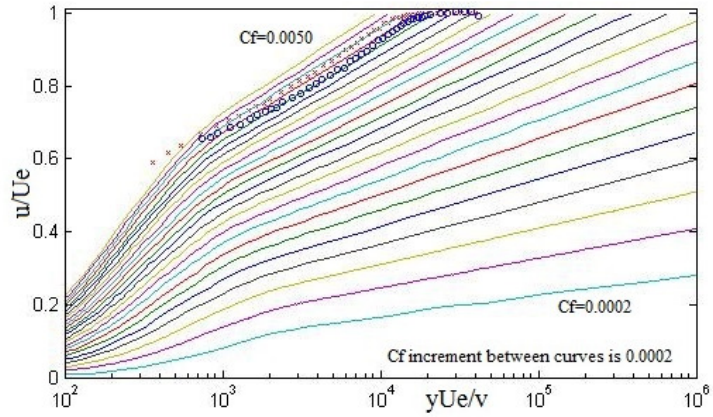

(c)

Figure 5.8: Charts used for the determination of the skin friction coefficient C_f from the experimental profiles at different positions over the flat plate (x) and riblets (○) middle of test section: (a) z=-1(Maximum reduction: 10.86%) (b) z=1 (c) z=3, (U_e: velocity at the edge of the boundary layer)

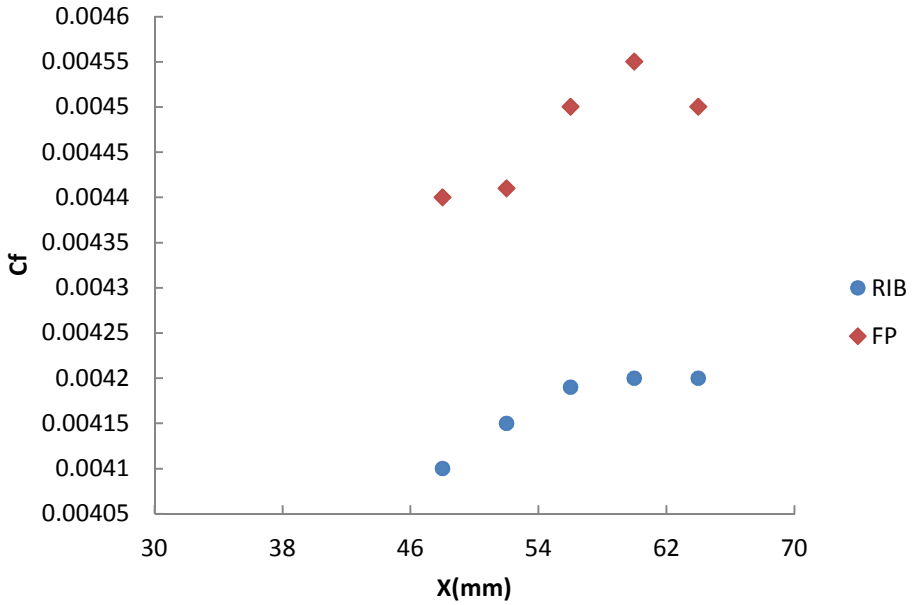

Figure 5.9: Charts used for the determination of the skin friction coefficient C_f from the experimental profiles at different stream-wise positions over the flat plate (♦) and riblets (•)

5.5 Velocity spectra

Considerations about the velocity spectra ($\emptyset_{uu}$ $[(m/s)^2/\text{Hz}]$) under the turbulent boundary layer have been summarised in this section, which have been calculated by averaging the spectra of 40000 records of 1024 samples each. The aim was to identify and confirm the characteristic frequencies present in the flow and hence, to obtain the specific information about the flow features over the riblets. The geometrical area under the spectrum, when plotted in semilogarithmic scale, represents the velocity fluctuations energy.

By plotting the spectra under two different representations (ribleted and smooth surface) a better understanding of the spectral characteristics of the flow as well as a better identification of the dominant frequencies have been possible. Figures 5.10 and 5.11 display the $\emptyset_{uu}$ at different positions in a stream-wise direction and it is

observed that the frequency associated with the dominant disturbance in the flow, is higher for the flat plate when compared with the riblets. Considering Figure 5.12, the velocity spectra's difference is higher near the wall and close to the boundary layer thickness and further away than it is around zero.

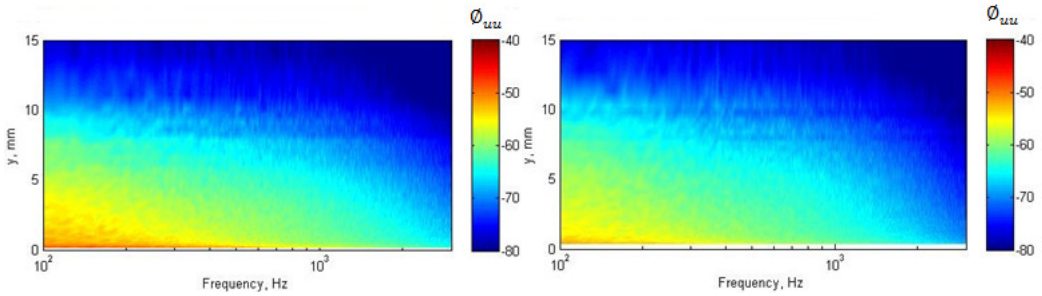

(a) (b)

Figure 5.10: Velocity spectra ($\emptyset_{uu}$ $[(m/s)^2/\text{Hz}]$) at middle of the test section (x=52mm): (a) flat plate (b) riblet plate

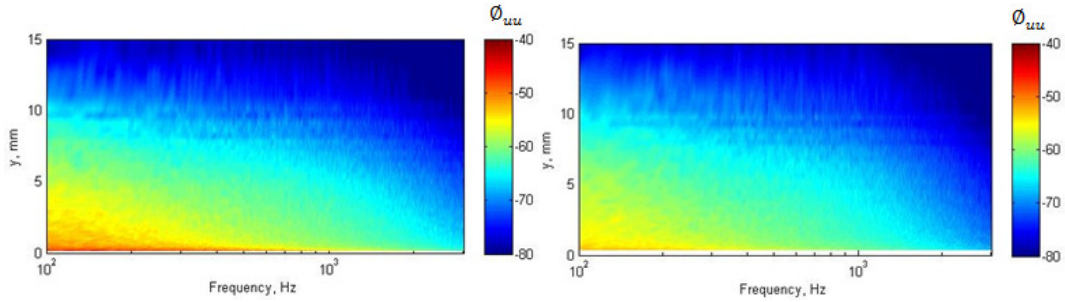

(a) (b)

Figure 5.11: Velocity spectra ($\emptyset_{uu}$ $[(m/s)^2/\text{Hz}]$) at middle of the test section (x=56mm): (a) flat plate (b) riblet plate

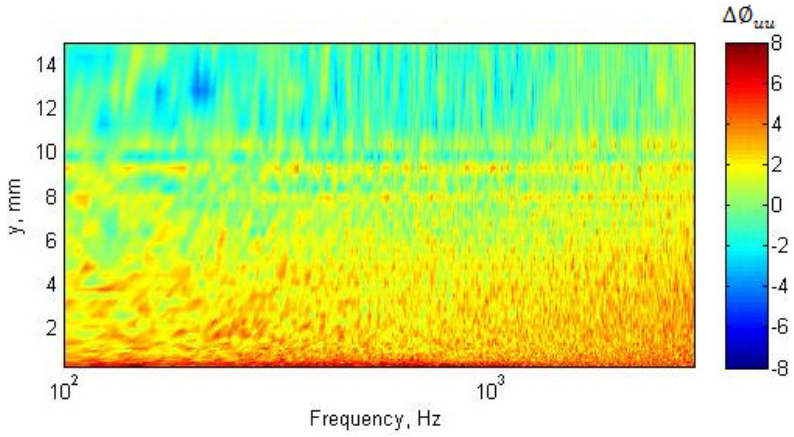

(a)

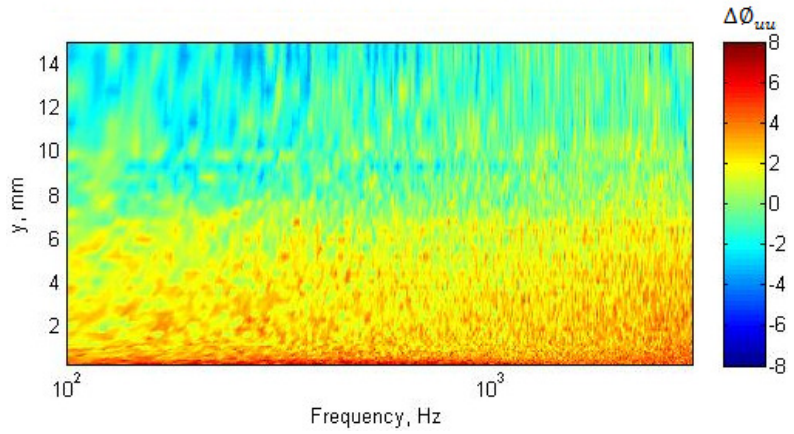

(b)

Figure 5.12: Difference in velocity spectra ($\Delta\emptyset_{uu}$ $[(m/s)^2$/Hz]) at middle of the test section: (a) x=52mm (b) x=56mm

5.6 Conclusion

The presented new design of riblets with serration inside provides 7% drag reduction. As is shown in Table 5.5, the drag in the present study has been decreased more than the other presented studies with U and V riblets. In section 1.3, two possible different mechanisms for drag reduction by riblets have been discussed. Further investigation is needed to confirm which mechanism is responsible for drag reduction by the designed riblet.

Chapter 6

TBL statistical structures on smooth and micro-structured surfaces

6.1 Introduction

In this chapter, some boundary layer features are investigated by performing cross-wire measurements and conditionally-time-averaged analysis of the data is examined in order to obtain a temporal variation of the statistical turbulence properties. The wall pressure spectra and the coherence functions (which are related to the span-wise correlation length) for the unsteady wall pressure on flat and riblet plates are also studied. It is hoped that the aerodynamic results presented in this chapter can help to improve the understanding of the riblets mechanism especially regarding the Serrate-Semi-Circular form.

6.2 Turbulence statistics

6.2.1 Reynolds shear stress and turbulent fluctuations

In this section, the turbulent velocity fluctuations (u_{rms}, v_{rms}) and Reynolds shear stress ($\overline{u'v'}$) under the different flow regimes are presented. The aim is to identify the dominant turbulence structures and how they will be affected by the micro-structured surface. Figure 6.1 shows the surface arrays for both investigated models.

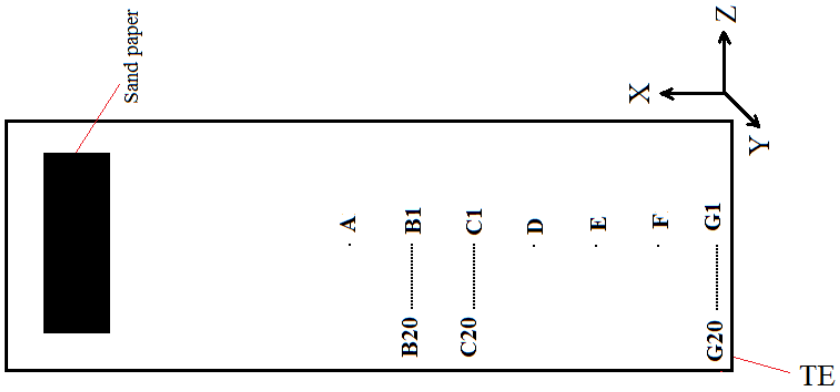

Figure 6.1: Surface arrays for both models investigated, the system of coordinates indicated in the figure

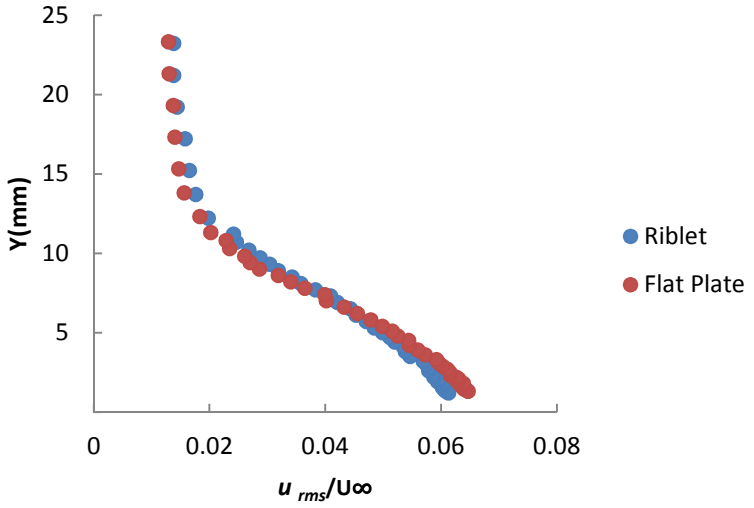

(a)

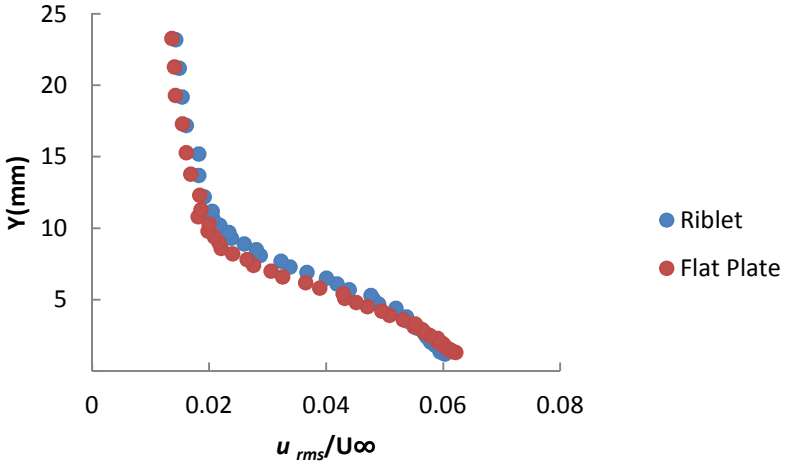

(b)

Figure 6.2: Velocity fluctuations (u_{rms}) for flat plate and riblets plate at positions: (a) G1 (TE) (b) D (middle of the test section)

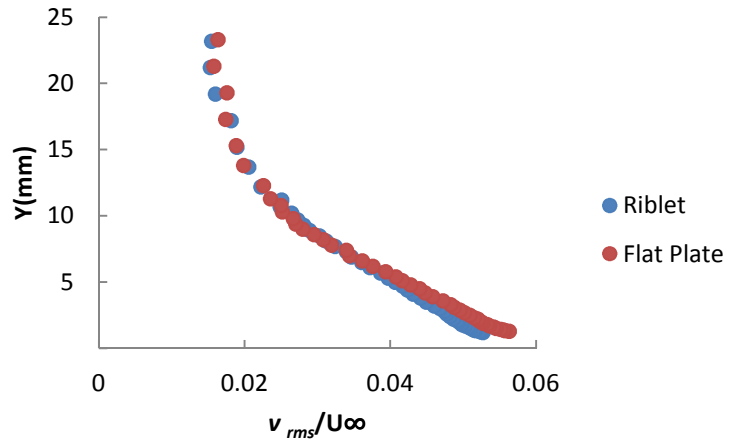

(a)

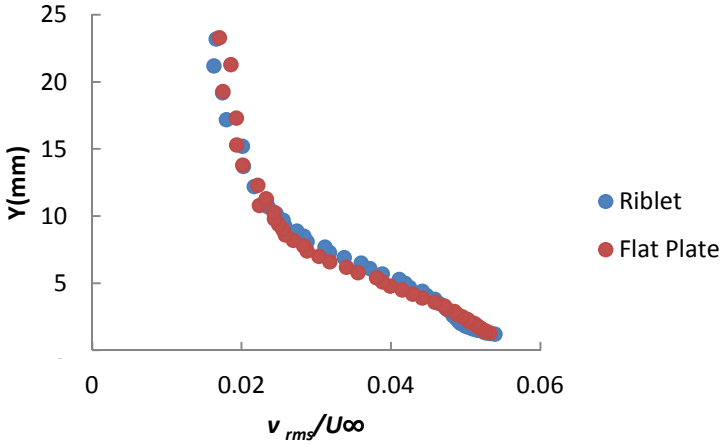

(b)

Figure 6.3: Velocity fluctuations (v_{rms}) for flat plate and riblets plate at positions: (a) G1 (TE) (b) D (middle of the test section)

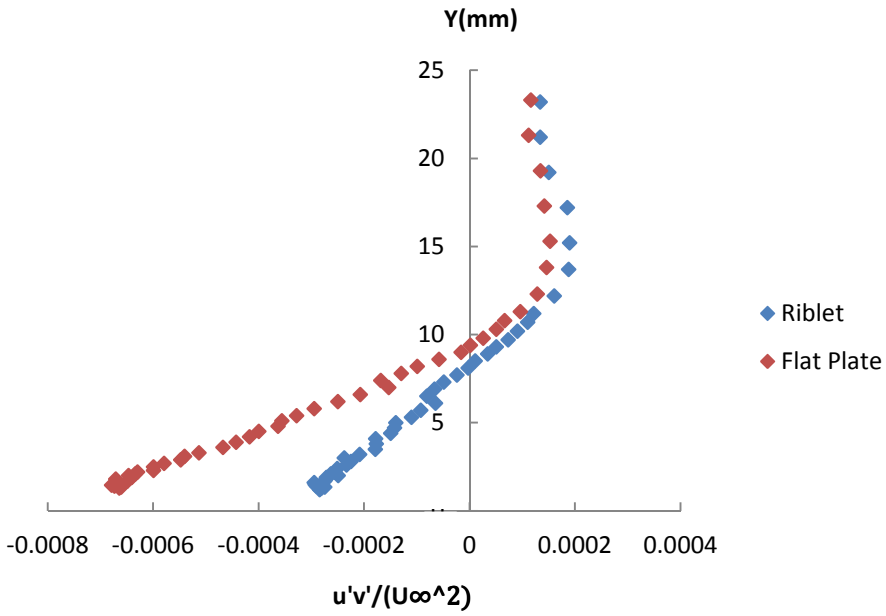

(a)

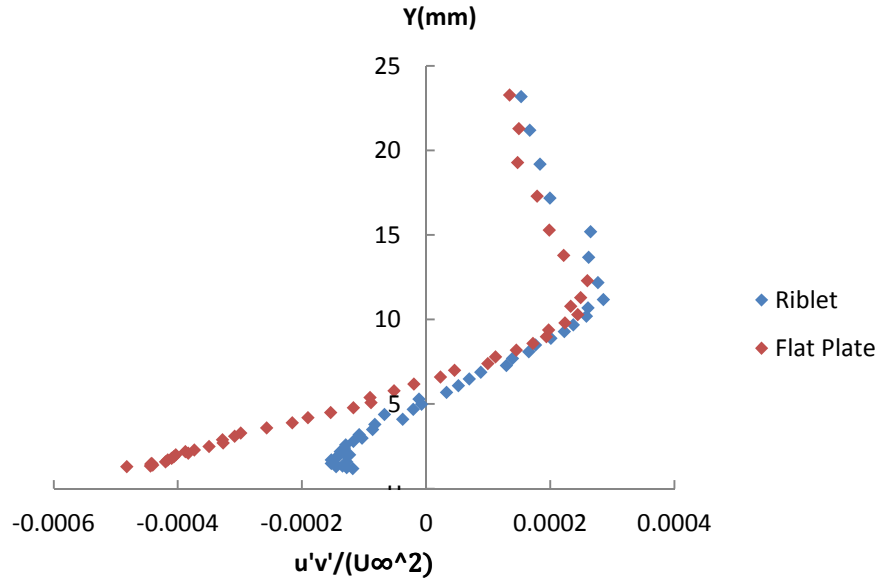

(b)

Figure 6.4: Reynolds shear stress for flat plate and riblets plate at positions: (a) G1 (TE) (b) D (middle of the test section)

Velocity fluctuations above the ribleted surface were reduced when compared with the smooth surface (Figures 6.2 and 6.3). The Reynolds shear stresses are shown in Figure 6.4 and although the maximum reduction of these close to the ribleted surface is significant (≈75%), the average Reynolds shear stress above them is reduced by 20% when compared to that above the flat plate. Choi (1993) reported a maximum reduction of 12% in the Reynolds shear stress above riblets and Walsh

(1980) claimed a 16% reduction. Moreover, Pulles et al. (1989) showed that the Reynolds shear stress is noticeably reduced through the log-law region for a riblet mounted surface. In addition, due to the calibration error the Reynolds shear stress exceeds zero. This error is, however, reflected in both models (flat and riblet plates) since they were examined under the same conditions.

6.2.2 Time-averaged turbulence structure

The previous sections were concerned with the Reynolds shear stress and velocity fluctuations of different positions on the smooth and ribleted surfaces. To provide a better understanding of the mechanisms involved the conditional average of the two components of the velocity and of the surface pressure fluctuations are analysed in this section. The boundary layer measurements took place at locations of G1-G3, G5, F, E, D, C1-C3, C5, B1-B3, B5 and A (Figure 6.1 and Tables 4.3 and 4.4 demonstrate the locations of the measurements), but to limit the amount of the collected data only the results corresponding to locations G1 are shown. Note that the wall pressure signals were also acquired simultaneously with the cross-wire during each measurement.

The basis of the conditional-averaging technique is similar to Sagrado (2007) and Daoud (2004). In this method the positive and negative wall pressure peaks in the time domain were used as the references for the ensemble averaging of the mean and fluctuating velocity signals, a graphical example of which is shown in Figure 6.4. First, an arbitrarily threshold of $\pm 1.5\, P'_{rms}$ (root-mean-square of pressure fluctuations [Pa]) was selected to identify the blocks of time relative to the dominant positive and negative wall pressure oscillations. Every time the p′ (Fluctuating surface pressure [Pa]) time series value exceeded that threshold or was inferior to it for the values below zero, the time of occurrence of the closest local positive or negative peak, respectively, that exceeded the threshold was found. This corresponded to a time offset of zero and the average of all velocity vectors occurring at all such instants for the entire velocity data record and hence represented the result at $\tau \approx 0$. Consequently, the positive (or negative) pressure peak at each identified time block is assigned to $\boldsymbol{\tau} \approx 0$. Therefore $\boldsymbol{\tau} < 0$ and $\boldsymbol{\tau} > 0$

represent times in advance and time delay, from the occurrence of the pressure peak, respectively. Once the times at which the pressure peaks occur have been identified for the entire number of pressure signals, the velocity signals could be ensemble-averaged accordingly. This is summarised in Figure 6.5, which shows a surface pressure signal with two lines indicating the arbitrary selected threshold values used to calculate the conditional averaged velocity vectors associated with positive and negative pressure peaks. Approximately 1400 ensembles were available to calculate the conditionally-averaged velocities at each point.

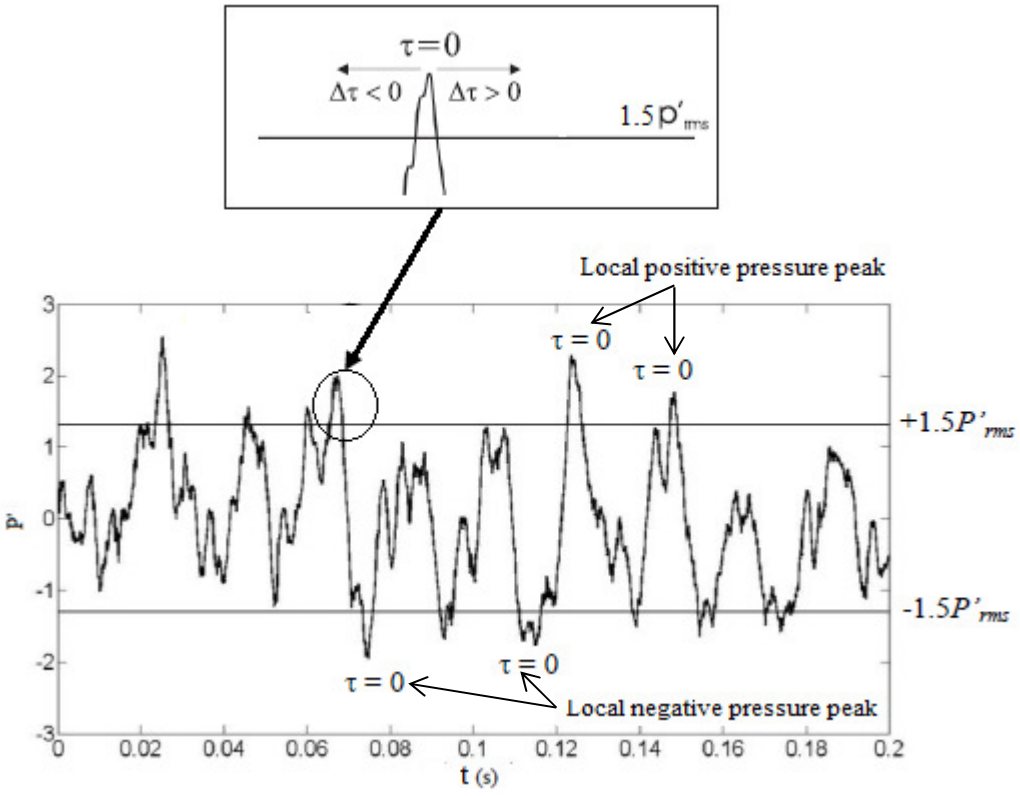

Figure 6.5: Surface pressure signals and the two threshold lines ($\pm 1.5P'_{rms}$) in sample real time selected to calculate the conditionally-averaged velocity associated with the positive and negative pressure peaks (Vathylakis and Chong, 2013)

The wall pressures <+P> and <-P> are associated with positive and negative pressure peaks, respectively, with the angular bracket denoting ensemble-averaged values. If <U(x, y, z; t) > and <V(x, y, z; t)> represent the ensemble-averaged velocities U and V respectively, the temporal variations of the velocity

perturbations caused by a coherent structure, $\widetilde{U}$ and $\tilde{V}$ relative to the local non conditionally-averaged velocities U_m and V_m can be calculated by:

$$\widetilde{U}(x,y,z;t) = \frac{<U(x,y,z,;t)> - U_m(x,y,z)}{U_\infty(x,z)} \tag{6.1}$$

$$\tilde{V}(x,y,z;t) = \frac{<V(x,y,z,;t)> - V_m(x,y,z)}{U_\infty(x,z)} \tag{6.2}$$

The velocity perturbation essentially measures the momentum excess or deficit caused by a coherent structure. Similarly, if the temporal variations of the root-mean-square (rms) fluctuations of u and v at each measurement point are represented by u_{rms} and v_{rms} respectively, they can be calculated as:

$$u_{rms}(x,y,z;t) = \frac{\sqrt{\sum_{i=1}^{N}[U(x,y,z;t) - <U(x,y,z;t)>]^2}}{N} \tag{6.3}$$

$$v_{rms}(x,y,z;t) = \frac{\sqrt{\sum_{i=1}^{N}[V(x,y,z;t) - <V(x,y,z;t)>]^2}}{N} \tag{6.4}$$

where N is the number of realizations. Finally, the temporal variations of the Reynolds shear stress <u′v′> can be calculated from the following equation:

$$< \mathrm{u'v'} > (x,y,z;t) = \sum_{i=1}^{N} \frac{[U(x,y,z;t) - <U(x,y,z;t)>][V(x,y,z;t) - <V(x,y,z;t)>]}{N} \tag{6.5}$$

Note that only the general features are discussed in relation to the conditionally-averaged results. At location G1, which is located close to TE and in the plane of symmetry, the corresponding contours of U, V, $\widetilde{U}$, $\widetilde{V}$, u_{rms}/U_∞, v_{rms}/U_∞ and $-< \mathrm{u'v'} >/(U_\infty)^2$ for <+P> and <-P> are shown in Figures 6.6 and 6.7, respectively. By examining the $\widetilde{U}$ contours for <+P>, it is clear that prior to the occurrence of the positive pressure peak around $\boldsymbol{\tau}\approx 0$ (the phase shift caused by the acquisition of the wall pressure signal and the cross-wire), activities pertaining to the passing of coherent structures are discernible for both of the smooth and ribleted surfaces.

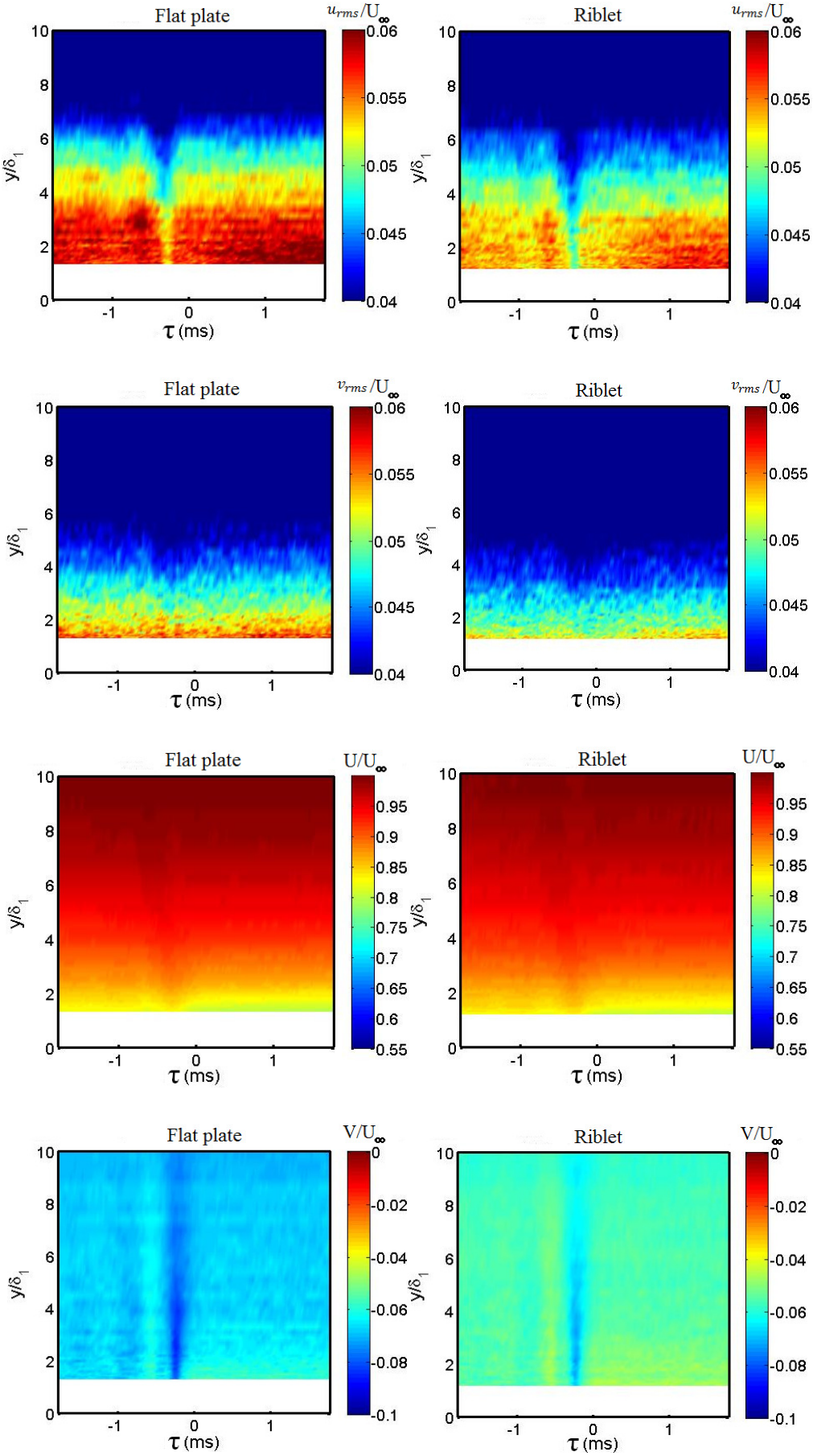
Flat plate
u_{rms}/U_∞
Riblet
u_{rms}/U_∞
Flat plate
v_{rms}/U_∞
Riblet
v_{rms}/U_∞
Flat plate
U/U∞
Riblet
U/U∞
Flat plate
V/U∞
Riblet
V/U∞
y/δ1
τ (ms)

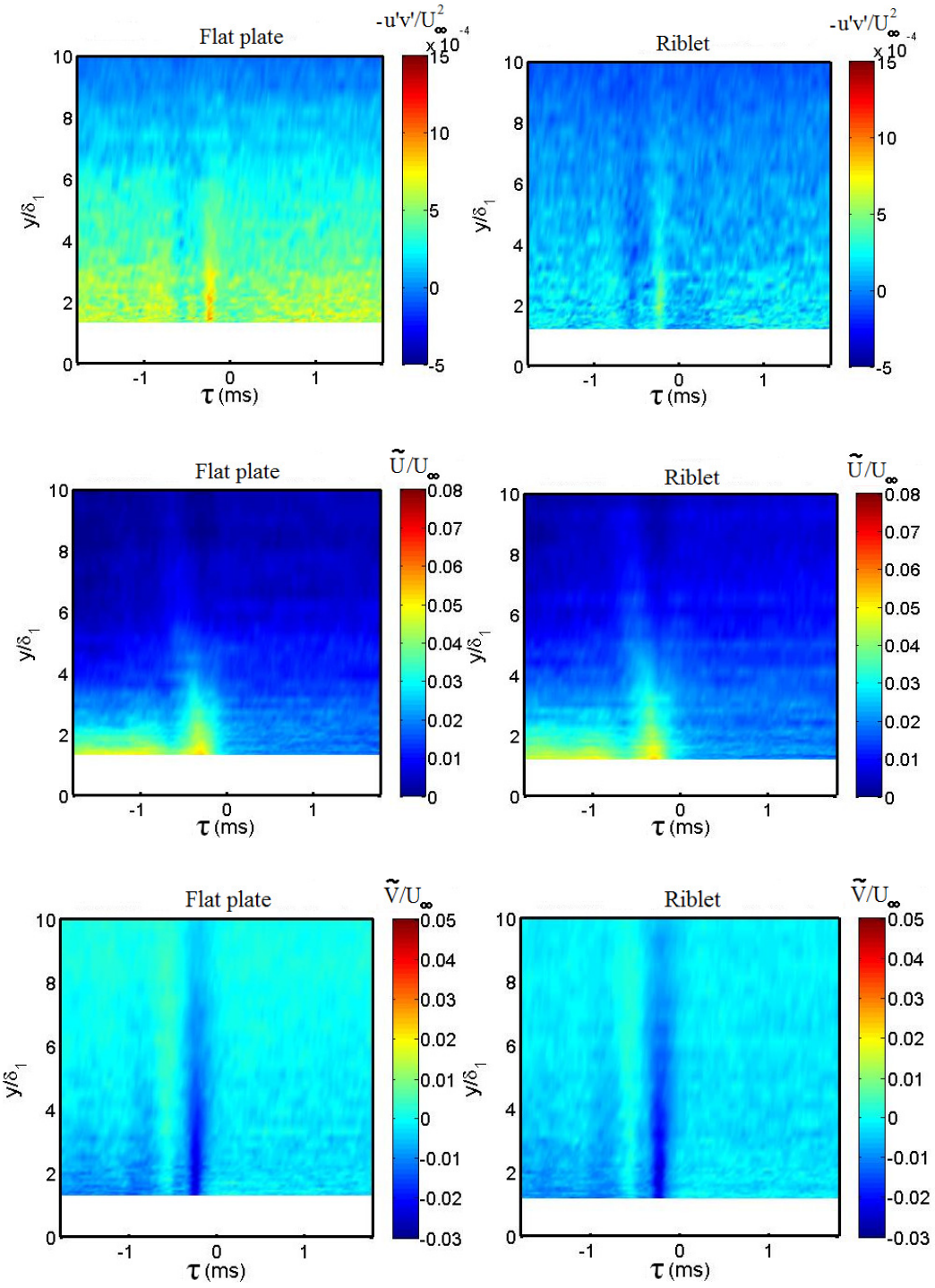

Figure 6.6: Contours of u_{rms}/U_∞, v_{rms}/U_∞, U/U_∞, V/U_∞ , $-< u'v' >/(U_\infty)^2$, $\widetilde{U}/U_\infty$, $\widetilde{V}/U_\infty$ and associated with <+P> at location G1

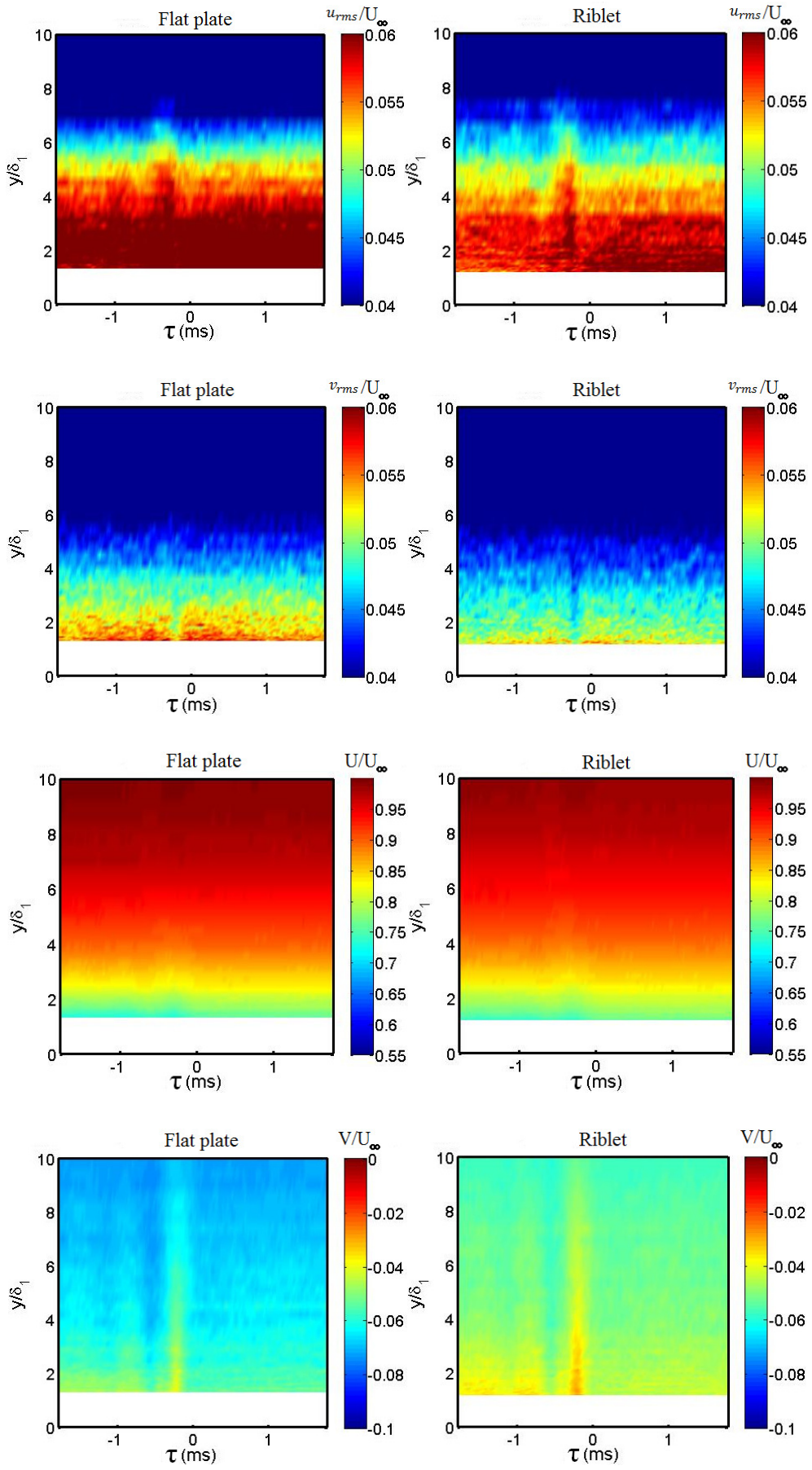
Flat plate
Riblet
u_{rms}/U_∞
v_{rms}/U_∞
U/U_∞
V/U_∞
y/δ_1
τ (ms)

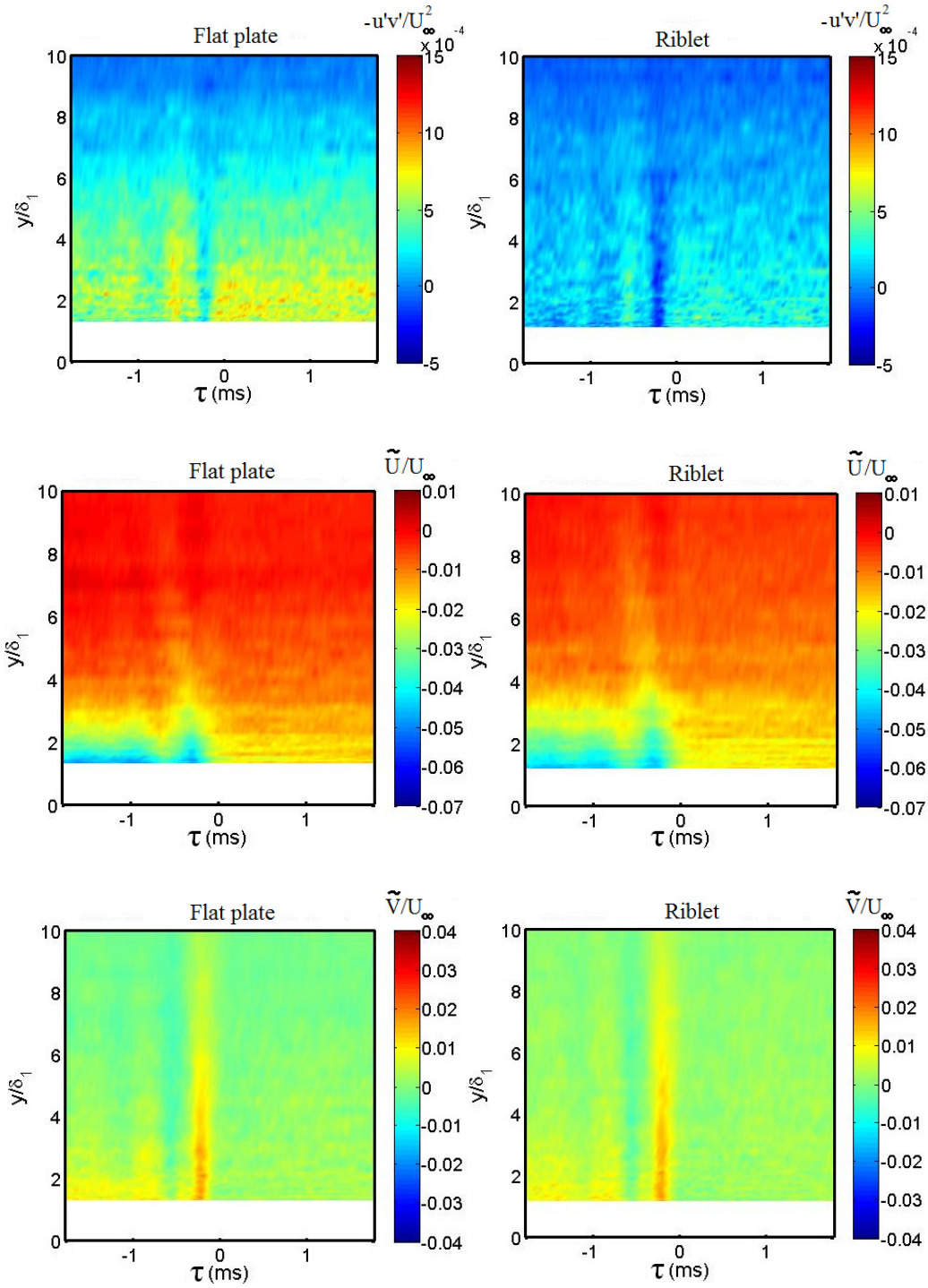

Figure 6.7: Contours of u_{rms}/U_∞, v_{rms}/U_∞, U/U_∞, V/U_∞ , $-< u'v' >/(U_\infty)^2$, $\widetilde{U}/U_\infty$, $\widetilde{V}/U_\infty$ and associated with <-P> at location G1

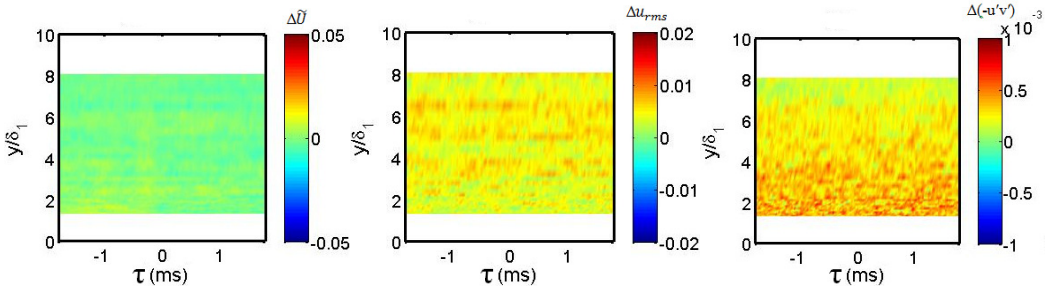

(a) (b) (c)

Figure 6.8: Contours of: (a) $\Delta\widetilde{U}$, (b) Δu_{rms} and (c) Δ(-u′v′) associated with <+P> at location G1 between smooth and ribleted surfaces

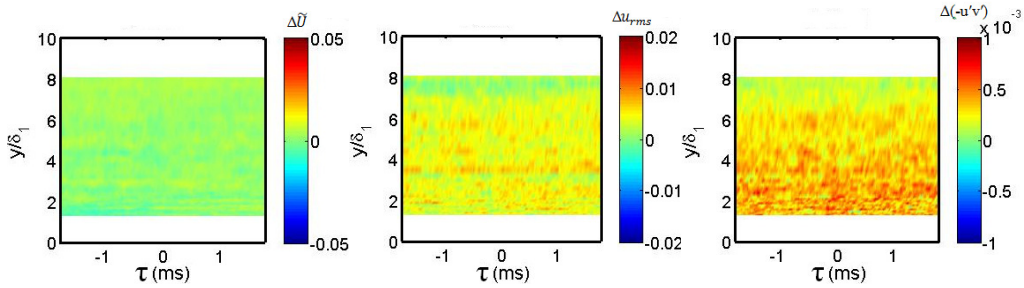

(a) (b) (c)

Figure 6.9: Contours of: (a) $\Delta\widetilde{U}$, (b) Δu_{rms} and (c) Δ(-u′v′) associated with <-P> at location G1 between smooth and ribleted surfaces

High momentum excess at $\boldsymbol{\tau}< 0$ for the $\widetilde{U}$ contour also indicates that ($< U > -U_m > 0$). For the corresponding $\tilde{V}$ contour, it can be observed that ($< V > -V_m < 0$), which indicates that the flow is towards the wall. This combination is related to the Q4-quadrant flow which, in conjunction with the <+P>, illustrates a sweeping of high-speed flow towards the near wall region (or to the back of the hairpin vortices) following a bursting event. Apparently the occurrence of high-momentum fluids also reduces the levels of Reynolds shear stress $< u'v' >/(U_\infty)^2$, as indicated in the figure. Conversely, a Q2-quadrant event ($< U > -U_m < 0, < V > -V_m > 0$) occurs for the <-P> case. This combination suggests that low-momentum fluids are ejected between the counter rotating legs of the hairpin vortices. The lifted low-momentum fluids, which are long and persistent at a higher velocity buffer layer, will eventually oscillate and break up. This event is commonly recognized as the main mechanism for generating turbulent energy, which

corresponds well with the current results on the Reynolds shear stress from which high $< u'v' > /(U_\infty)^2$ level can be observed for the <-P> case. The above mechanisms are also manifested exactly in the u_{rms}/U_∞, v_{rms}/U_∞contours for the <+P> and <-P> cases.

The results in Figures 6.6 and 6.7 suggest that both of the smooth and ribleted surfaces are not significantly different in terms of their characteristics in the velocity perturbations, rms velocity fluctuations and Reynolds shear stresses. In both figures, the velocity components in the stream-wise direction (U) have not changed, but the Vs (in non-stream-wise direction) have reduced for the ribleted surface. This reduction for the <-P> case suggests that vortices interaction in ejection for the ribleted surface is decreased. Also, the reduction for the <+P> case can be evidence that riblets reduce the skin-friction drag by impeding the non-stream-wise movement of longitudinal vortices during the sweep events (Choi, 1989 and 1987; Crawford, 1996).

In addition, the averaged Reynolds shear stresses $\overline{u'v'}/(U_\infty)^2$, which are calculated from the non-conditionally-averaged velocity data, are compared in Figure 6.4 for the flat plate and ribelts at location G1 in the previous section. Near the wall region the $\overline{u'v'}/(U_\infty)^2$ level for the riblet model is significantly lower, the similar results obtained with u_{rms}/U_∞ and v_{rms}/U_∞ (Figures 6.8 and 6.9). However, velocity perturbations contours do not illustrate a significant difference between the flat plate and rib lets, especially around the outer region of the boundary layer. This finding suggests that the riblets although having been effective at the near wall region, which is dominated by the viscous effect, are unable to influence the outer part of the boundary layer which constitutes the momentum part of the TBL.

6.3 Unsteady wall pressure on smooth and ribleted surfaces

In this section, a comparative study is performed, using the methodology described in Section 4.2.5 and 4.2.6 for the wall pressure *PSD*. As shown in Table 4.3, the measurement points comprise 70 locations of G1–G20, F, E, D, C1-C20, B1-B20, and A for both types of plates (Figure 6.1). The results from the coherence and

phase between microphones are presented, with the former, γ^2, providing further information about the TBL pressure structure. It characterises the frequency content of the cross-correlation and is defined as:

$$\gamma^2(f) = \frac{\left|\Phi_{p_i p_j}(f)\right|^2}{\Phi_{p_i p_i}(f)\Phi_{p_j p_j}(f)} \tag{6.6}$$

where $0 \leq \gamma^2 \leq 1$. It is also called $G_{p_i p_j}$ (the coherence) and its square root, γ, is the normalised cross-spectrum between the two signals $p_i'(t)$ and $p_j'(t)$. Hence, it is calculated by means of the cross-spectrum ($\Phi_{p_i p_j}$) between the two pressure signals and the autospectrum ($\emptyset_{p_i p_i}$) of each individual signal. $\Phi_{p_i p_j}$ is a complex function, $\Phi_{p_i p_j}(f) = \left|\Phi_{p_i p_j}(f)\right| \exp(i\emptyset_{p_i p_j}(f))$, where $\emptyset_{p_i p_j}(f)$ is the phase angle between the coherent components of $p_i'(t)$ and $p_j'(t)$. It can be calculated by direct spectral analysis or as the Fourier transform of the cross- correlation. When the frequency bandwidth of analysis is 1 Hz, the autospectrum $\Phi_{p_i p_i}$, equals the power spectral density (PSD) which has been called $\Phi, \Phi(f), \Phi(\mathrm{w})$ in this dissertation. The relationship between $\Phi(\mathrm{w})$ and $\Phi(f)$ is, $\Phi(\mathrm{w})=\Phi(f)/2\pi$ (Sagrado, 2007).

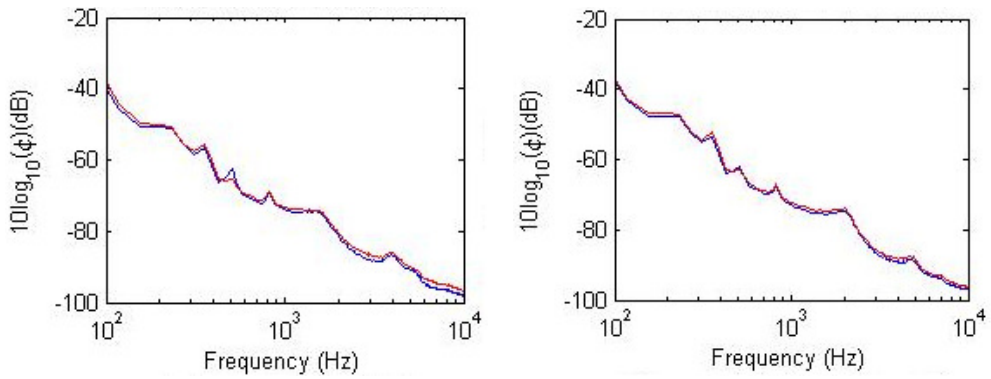

(a) (b)

Figure 6.10: An example of wall pressure power spectra density (PSD) measured by two remote microphones sensor or smooth plate (red) and riblets (blue) at C1-C2: (a) power spectral density of microphone A (b) power spectral density of microphone B

In order to investigate the coherences γ^2 and phases Ø of the turbulent eddies, a pair of microphones in various combinations of Δx (stream-wise spacing) and Δz

(span-wise spacing) was used to measure the unsteady wall pressures simultaneously on both of the plates. Figure 6.10 presents the PSD for each microphone separately. At low frequencies, the power spectra for both models are relatively close, with there being a slight difference at high ones. Due to the large quantity of data obtained, only selective results are presented here. Figure 6.11 shows coherence γ^2 and the phase spectra for the span-wise arrangement of the microphones (i.e. $\Delta x > 0$, $\Delta z = 0$) on the smooth and ribleted surface. Note that the pairing of the microphone can be referred to the notations used in Table 4.3.

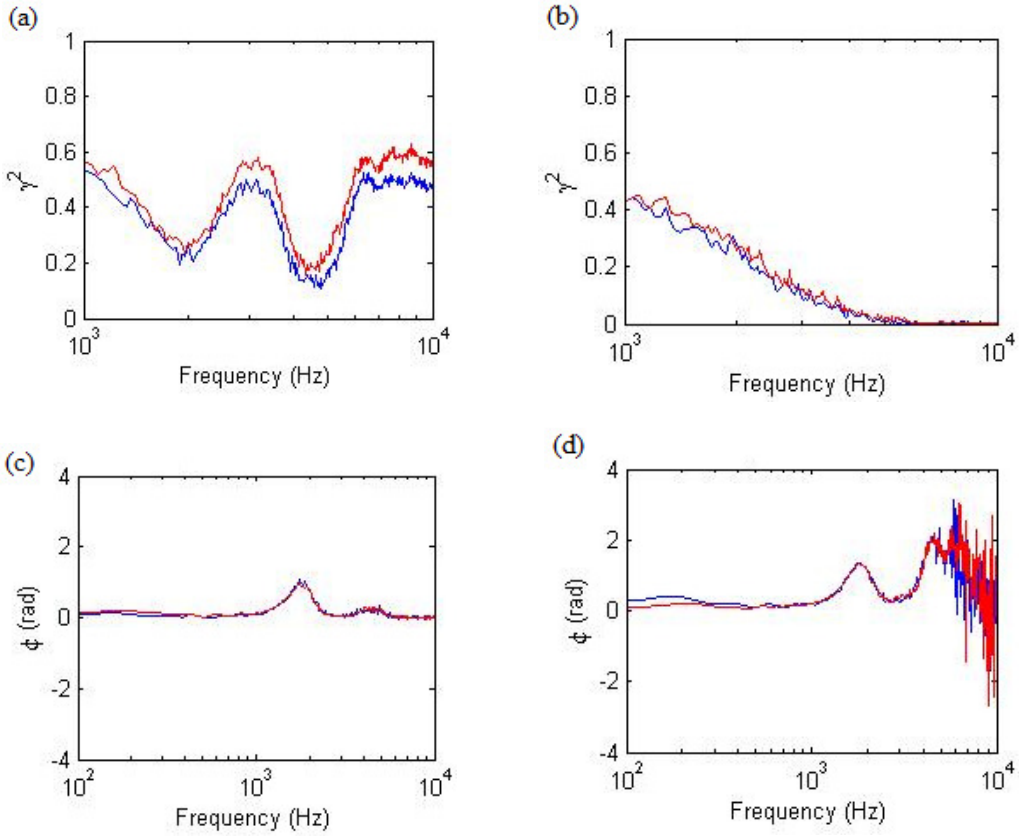

Figure 6.11: Span-wise phase spectra Ø (rad) and coherence γ^2 for smooth surface (red) and riblets (blue) of the following microphone pairs: (a-c) C1–C2 and (b-d) G1-G2

Figure 6.12 shows the difference in the coherence spectra level between the smooth and ribleted surfaces which becomes smaller through the spanning. At an even further upstream location, there is no longer any discernible difference between the surfaces. One reason why the coherence differences are small is because of the location of the microphones holes. These holes should be as close as possible to

each other in order to be able to cover approximately the vortices' size (which is not physically possible because of the microphones sizes).

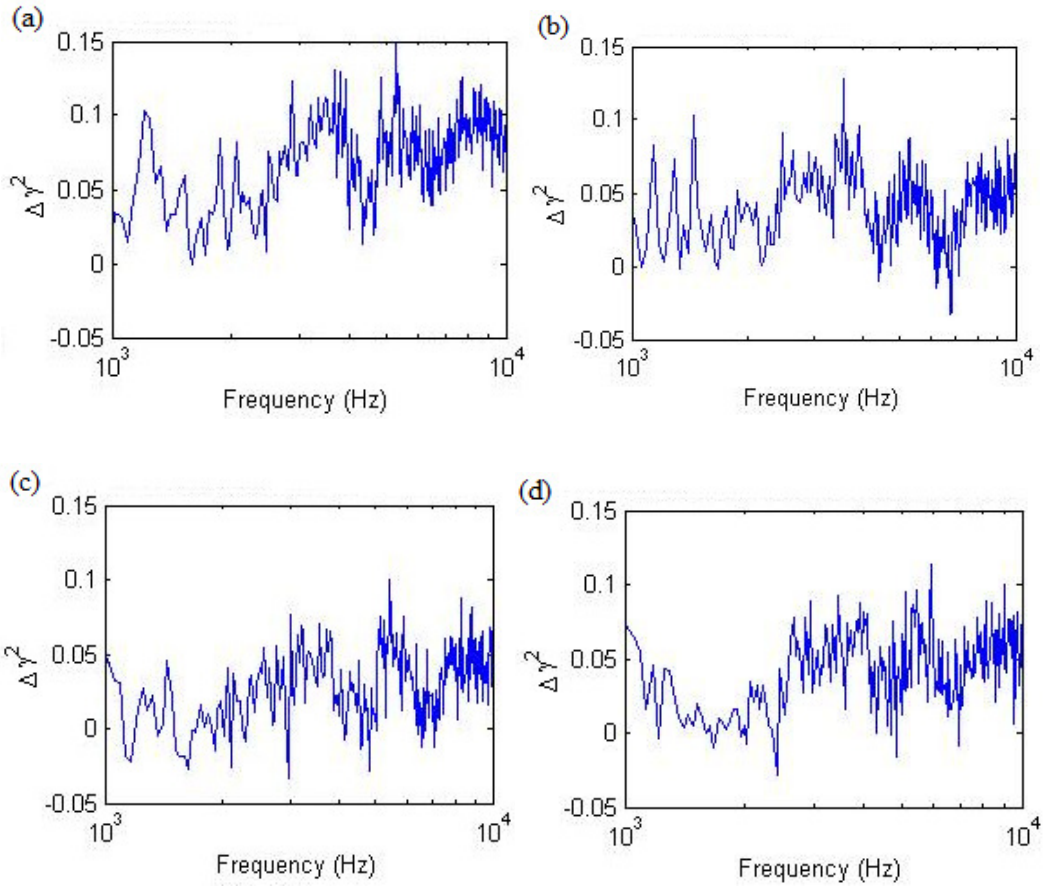

Figure 6.12: Measured the difference in coherence γ^2 (a – c) for smooth surface and riblets of the following microphone pairs: (a) C1–C2; (b) C1–C3; (d) C1-C4; and (d) C1-C7

6.4 Conclusions

In this chapter, the results from the cross-wire show that the Reynolds shear stress is noticeably reduced for the ribleted surface. In addition, an experimental study for a conditionally-averaging technique was applied to the cross-wire data at several locations on the smooth and ribleted surfaces to investigate the temporal variations of the pseudo-coherent structures. Finally, although the coherence and phase is smaller for the riblet model, the difference in coherence between two models was found not to be significant.

Chapter 7

Conclusions and recommendations for future work

7.1 Conclusions

This chapter summarises the main conclusions from the present investigation of micro structure mechanisms of relevance to drag reduction. The mechanisms studied have been those related to skin friction from turbulent boundary layers at zero angle of attack.

These complex mechanisms have been investigated from an aerodynamic point of view, i.e. by modelling of the different type of riblets and performing measurement of the surface pressure fluctuation and of the velocity field in the boundary layer. Such detailed measurements have provided further understanding of the relationship between the velocity and wall pressure fields and thus, about the flow structures over the ribleted surface. These flow structures comprise the sources of the velocity fluctuations, which are closely related to the sources of the skin friction.

The main conclusions are drawn as follows:

- The modelling was carried out to predict the drag reduction by riblets, in order to optimize the local skin friction. Workbench FLUENT version (14.0) was used as the Computational Fluid Dynamics Solver for the computer simulations. The numerical simulation consisted of geometry creation, region specification, mesh generation, domains creation, boundary conditions assignment and (k-ε) Equation solution. Drag reduction efficiencies were analysed by comparing two kinds of different geometry shapes, Semi-Circular and Serrate-Semi-Circular. The presented exploration, comprising a family of Serrate-Semi-Circular riblets, according to the modelling predictions, would give better performance than the usual Semi-Circular shape. That is, the results show that high drag reduction can be obtained with variations in the geometry and dimensions of the riblets. The best dimensions of

the Serrate-Semi-Circular riblets that give a high reduction in drag are: s_1=0.21mm, s_2=0.15mm, h_1=0.11mm and h_2=0.08mm.

- For all types of turbulence flow with different Reynolds numbers as long as it is continuously turbulent the instability problem exists in the buffer layer. Therefore, it is acceptable to assume that in this sub-layer the damping action of the viscosity is equally large with the effect of three dimensional perturbations; and these disturbances are intensified and are sufficiently large inside log law layer that is totally turbulence. One difficulty in defining the disturbances inside the buffer layer is that the perturbation appears at irregular time intervals at different irregular distributed positions. That is, in this region, sometimes the disturbances die away and sometimes they grow. This uncertainty should be considered as one of the reasons why the riblets are only effective in this region.
- Usually, a large portion of the total drag on long objects with relatively flat sides comes from turbulence at the wall, so riblets will have an appreciable effect. In addition, understanding the extent of the roughness effect arising from a variety of structured surface types would improve predictive capabilities for drag reduction. Regarding this, close to the wall itself, the effects of the featured surface on the velocity field depend on the specific geometry of the roughness elements. The review of controlling near-wall turbulence by riblets demonstrated that the reason why they give only about 6% reduction in skin friction is due to the geometry optimization. Therefore, structured surfaces may be a solution as a passive method due to their variety in sizes and shapes. In addition, some researchers have tried to simulate the flow over three-dimensional riblets experimentally in order to understand why this structure leads to the reduction of viscous drag in turbulent flow. However, the difficulty of such research has become clear due to the variety of variables and the complexity of the accompanying three-dimensional flow. Consequently, most of the CFD research is performed on a two-dimensional representation of the riblets, thereby decreasing the complexity of the problem. In many cases, the preparation of the surface mesh is the most time-consuming phase. Also, this phase often requires trimming or approximation of tiny parts difficult to resolve with the mesh. For this reason and the fact that the textures are three dimensional despite the riblets, the need for three dimensional modelling arises.

- Experimental facilities, instrumentation and measurement techniques have been used in the present investigation. Recently devised measurements of good quality, using pitot tubes, hot-wire (single and cross-wire probes) and automated traverse, have been employed to assess critically, and then to improve the experimental accuracy of, the empirical coefficient for the determination of the surface shear and skin friction. In addition, microphones were embedded in the model to characterise in detail the unsteady pressure fluctuations on the surface of the plates under different boundary layer regimes, especially with the presence of riblets. Further, analytical techniques were used to obtain a large matrix of data for velocity profile and turbulence quantities, which encompassed hydraulically smooth and rough flow regimes. ThermalPro and MATLAB were employed for the data analysis.
- Boundary layer profiles along the plates, smooth surface and riblets, have been investigated, the mean velocity profiles, root-mean-square (rms) velocity profiles and integral parameters. These proposed results have been obtained by single hot wire measurements. The determination of the onset of transition was achieved by careful analysis of the temporal signals of velocity (single hot-wire) and their spectra. It was found that the presented new design of riblets (s_1^+=19.5, s_2^+=14, h_1^+=10.5, h_2^+=7.5 and $A_g^{+1/2}$=11) with serration inside provides 7% drag reduction. Consequently, as has been shown in Table 5.5, the drag in the present study has been decreased more than the other presented studies and hence it can be concluded that Serrate-Semi-Circular shape provides reduction in velocity spectra and profiles.
- The cross correlation experiment, using a cross-wire and microphone, simultaneously, was performed to analyse the velocity components. The results did not detect any momentum transfer delay for the ribleted surface, especially for the outer region of the TBL. In addition, the wall pressure spectra and the coherence functions for the unsteady wall pressure on flat and riblets' plates were studied using two microphones. The results of this indicate that although the coherence and phase is smaller for the riblet model, the difference in coherence between the two models is found not to be significant.

The results from the different analysis of the simultaneous velocity and surface pressure were consistent and the different techniques were found to be complementary. Moreover, the stochastic estimation method expands the wealth of information about the relationship between riblets and drag reduction. It affords additional knowledge about the variability and characteristics of the dominant wall pressure generating flow structures in the presence of riblets. In sum, it is hoped that this detailed study into the nature of the wall roughness and its effect on skin friction has provided new understanding about riblets mechanisms.

7.2 Contributions to knowledge

The innovations and contributions to knowledge from this research are summarised as followings:

- A new micro-structured surface (Serrate-Semi-Circular riblets) has been designed with particular emphasis on the most effective shapes, and on the conditions under which drag reduction increases. Moreover, special attention has been given to the effect of serration (angles) and cross sectional area (A_g).
- The modelling has been employed to predict the drag reduction by selected riblets, in order to optimize the local skin friction and the riblets effects have been simulated using the (k-ε) Equation solution as numerical modelling.
- Investigations on the selected riblet have been carried out with well-designed evaluation trials. Skin friction and boundary layer structures have been studied in order to find the mechanism of drag reduction by riblets. Moreover, a conditionally-time-averaged analysis of the data has been undertaken in order to obtain a temporal variation of the statistical turbulence properties in the presence of a microphone and a cross-wire, simultaneously.

7.3 Recommendations for future work

Recommendations and suggestions for future work are put forward in this section:

- At the present time, no mathematical model exists that can predict the transition event on the buffer layer in turbulent flow and one obvious reason for this lack is the variety of influences such as freestream turbulence, surface roughness, sound, etc. Amplitude and spectral characteristics of the disturbances inside the laminar viscous layer strongly influence which type of transition occurs. The major need in this area is to understand how freestream disturbances are entrained into the boundary layer, i.e. to find the effect of roughness on the buffer layer.
- Currently, the study of the effect of riblets is focused on their sizes and shapes. Since the density of the riblets on the surface is almost linearly proportional to the amount of coverage over the body surface, the effect of their density has not been considered. However, this might not be economical and beneficial for all case studies. Therefore, apart from investigating the geometrical properties of riblets, the statistical properties of their finite densities could bear fruit in this field of study. One possible approach to studying configuration is simply to conduct numerical calculation on their densities explicitly from the Navier-Stokes equation; but this may turn out to be a hopeless task even for structured surfaces of moderate size. Consequently, a mathematical framework for expressing scale invariance in the skin friction coefficient should be developed.
- Due to the highly idiosyncratic nature of potential riblet applications (e.g. wind turbine blade, airfoil, etc), further testing of riblets of various sizes, geometries and configurations on a wider range of Reynolds numbers would provide valuable insights into their performance across these applications and thus help move forward trends observed in this study.

References

Acharya, M., Bornstein, J., and Escudier, M. P., 1986. 'Turbulent boundary layers on rough surfaces'. *Experiments in Fluids*, Vol.4, pp. 33-47.

Afazov, S.M., Ratchev, S.M., and Segal, J., 2010. 'Modelling and simulation of micro-milling cutting forces'. *Journal of Materials Processing Technology*, Vol.210 (15), 19, pp. 2154–2162.

Afzal, N., 2001. 'Power law and log law velocity profiles in fully developed turbulent boundary layer flow: equivalent relations at large reynolds numbers'. *Acta Mechanica*, Vol.151**,** pp. 195-216.

Akinlade, O. G., 2005. 'Effects of surface roughness on the flow characteristics in a turbulent boundary layer'. PhD Thesis, University of Saskatchewan, Canada.

Allen, J. M., and Tudor, D. H., 1969. 'Charts for interpolation of local skin friction from experimental turbulent velocity profiles'. Technical report, Tech. Rep. *NASA* SP-3048.

Antonia, R. A., and Krogstad, P. A., 2001. 'Effect of different surface roughnesses on a turbulent boundary layer'. *Fluid Dynamics Research,* Vol.28, pp. 139-157.

Bacher, E. V., and Smith, C. R., 1985. 'A combined visualisation-anemometry study of the turbulent drag reduction mechanisms of triangular micro-groove surface modifications'. *American Institute of Aeronautics and Astronautics (AIAA),* paper 85-0548.

Bandyopadhyay, P. R., 1987. 'Rough-wall turbulent boundary layers in the transition regime'. *Journal of Fluid Mechanics*, Vol.180, pp. 231-266.

Barenblatt, G. I., 1993. 'Scaling laws for fully developed shear flow. Part 1. Basic Hypotheses and Analysis'. *Journal of Fluid Mechanics,* Vol.248, pp. 513-520.

Barenblatt G. I., Chorin A. J., and Prostokishin V. M., 2000. 'A note on the overlap region in turbulent boundary layer'. *Physics of Fluids*, Vol.12**,** pp. 2159-2161.

Baron, A., Quadrio, M. and Vigevano, L., 1993. 'On the boundary layer/riblets interaction mechanisms and the prediction of turbulent drag-reduction'. *The International Journal of Heat and Fluid Flow,* Vol.14, pp. 324-332.

References

Baron, A., and Quadrio, M., 1997a. 'Turbulent boundary layer over riblets: conditional analysis of ejection-like events'. *The International Journal of Heat and Fluid Flow,* Vol.18 (2), pp. 188-196.

Baron, A., and Quadrio, M., 1997b. 'On the accuracy of wall similarity methods in determining friction velocity over smooth and ribletted surfaces'. *Transaction of the ASME: Journal of Fluids Engineering,* Vol.119 (4), pp. 1009-1011.

Bechert, D. W., Bruse, M., Hage, W. and Meyer, R., 1997. 'Biological surfaces and their technological application - laboratory and flight experiments on drag reduction and separation control'. *American Institute of Aeronautics and Astronautics (AIAA)*, paper 97-1960.

Bechert, D. W., and Bartenwerfer, M., 1989. 'The viscous flow on surfaces with longitudinal ribs'. *Journal of Fluid Mechanics*, Vol.206, pp. 105–129.

Bechert, D. W., Bruse, M. and Hage, W., 2000. 'Experiments with three-dimensional riblets as an idealized model of shark skin'. *Experiments in Fluids,* Vol.28, pp. 403-412.

Bechert, D. W., Bruse, M., Hage, W., van der Hoeven JGT and Hoppe, G., 1997. 'Experiments on drag-reducing surfaces and their optimization with an adjustable geometry'. *Journal of Fluid Mechanics,* Vol.338, pp. 59–87.

Beibei, F., Xiaodi, L., Darong, C. and Jiadao, W., 2011. 'Characteristics of flow over thin triangular riblet surface'. WSEAS International Conference, *Recent Advances in Fluid Mechanics*, Heat & Mass Transfer and Biology. <www.wseas.us/books/2012/CambridgeUSA/FLUHMABE.pdf> (Accessed: 12 December 2013).

Benhalilou, M., Anselmet, F., Liandart, J. and Fulachier, L., 1991, 'Experimental and numerical investigation of a turbulent boundary layer over riblets'. Procceeding of the 8th Symp. on Turbulent *Shear Flows*, Munich, pp. 18-5.

Blackwelder, R. F., and Kaplan, R. E., 1976. 'On the wall structure of turbulent boundary layers'. *Journal of Fluid Mechanics,* Vol.776, pp. 89-112.

Bogard, D. G., and Tiederman, W. G., 1986. 'Burst detection with single-point velocity measurements'. *Journal of Fluid Mechanics,* Vol.162, pp. 389-413.

Bradshaw, P., 1987. Wall Flows. *In Turbulent Shear Flows* 5, (eds. F. Durst, B. E. Launder, J. L. Lumley, F. W. Schmidt, and J. H. Whitelaw), pp. 171-175.

References

Brinskmeier, E., 2003. 'Residual stress in precision engineering components'. Fifth International Conference on *Industrial Tooling*, Southampton, UK, 10-11 September, pp. 1-22.

Brooks, T. F., and Hodgson, T. H., 1981. 'Trailing edge noise prediction from measured surface pressures'. *Journal of Sound and Vibration*, Vol. 78, pp. 69–117.

Browne, L. W. B., Antonia, R. A. and Chua, L. P., 1989. 'Calibration of X-probes for turbulent flow measurements'. *Experiment in Fluids*, Vol. 7, 1989, pp. 201-208.

Bruse, M., 1993. 'Experiments with conventional and with novel adjustable drag-reducing surfaces'. In: So, R.M.S. et al. (Eds.), Near-wall Turbulent Flows. Elsevier, Amsterdam, pp. 719-738.

Bruun, H. H., 1995. 'Hot-Wire Anemometry: Principles and Signal Analysis'. 20. Oxford University Press.

Buschmann, M. H., and Gad-el-Hak, M., 2003. 'Debate Concerning the Mean-Velocity Profile of a Turbulent Boundary Layer'. *American Institute of Aeronautics and Astronautics (AIAA) Journal*, Vol.41, pp. 565-572.

Bushnell, D. M., 2003. 'Aircraft drag reduction – A review'. *Proceedings of Institute of Mechanical Engineers*, part G: Journal of Aerospace Engineering, Vol.217 (G1), pp. 1–18.

Castillo, L., and Walker, D. J., 2002. 'Effect of upstream conditions on the outer flow of turbulent boundary layers'. *American Institute of Aeronautics and Astronautics (AIAA) Journal*, Vol.40, pp. 1292-1299.

Chen, H., Zhang, X., Zhang, D., Pan, J., Hagiwara, I., 2013. 'Large-scale equal-proportional amplification bio-replication of shark skin based on solvent-swelling PDMS'. *Journal of Applied Polymer Science*, DOI: 10.1002/APP.39402.

Choi, K. S., and Johnson, R., 1989. 'Near wall structure of a turbulent boundary layer with riblets'. *Journal of Fluid Mechanics*, Vol. 208, pp. 417– 458.

Choi, H., Moin, P., and Kim, J., 1993. 'Direct numerical simulation of turbulent flow over riblets'. *Journal of Fluid Mechanics*, Vol.255, pp. 503–39.

Choi, K. S., 1987. On physical mechanisms of turbulent drag reduction using riblets. In Transport Phenomena in *Turbulent Flows*, ed. M Hirata, N Kasagi, pp. 185–98. New York: Hemisphere.

References

Choi, K. S., 1989. 'Near wall structure of a turbulent boundary layer with riblets'. *Journal of Fluid Mechanics,* Vol.208, pp. 417-458.

Choi, K. S., 1999. 'European drag-reduction research - recent developments and current status'. *Fluid Dynamics Research*, Vol. 26, pp. 325-335.

Chu D. C., and Karniadakis G. E., 1993. 'A direct numerical simulation of laminar and turbulent flow over riblet-mounted surfaces'. *Journal of Fluid Mechanics,* Vol.250, pp. 1–42.

Clauser, F. H., 1954. 'Turbulent boundary layers in adverse pressure gradient'. *Journal of the Aeronautical Sciences,* Vol.21, pp. 91-108.

Coleman, G. N., and Sandberg, R. D., 2010. 'A primer on direct numerical simulation of turbulence methods, procedures and guidelines'. *Aerodynamics & Flight Mechanics* Research Group, University of Southampton, SO17 1BJ, UK, (March 2010).

Coleman, H. W., and Steele, W. G., 1999. 'Experimentation and Uncertainty Analysis for Engineers'. 2nd Ed, *Wiley*, New York.

Coles, D., 1956. 'The law of the wake in the turbulent boundary layer'. *Journal of Fluid Mechanics*, Vol.1, pp. 191-226.

Coles, D., 1962. 'The turbulent layer in a compressible fluid'. *The Rand Corp*., Rep. R-403-PR., Santa Monica, California.

Comte-Bellot, G., Sabot, J., and Saleh, I., 1978. 'Detection of intermittent events maintaining Reynolds stress'. *Proceedings of the Dynamic Flow Conference*, Marseille.

Corrsins, S., 1961. 'Theories of turbulent dispersion. Mlcanique de la Turbulence. Colloques Internationaux du Centre National de la Recherche Scientifique', no. 108, Editions du CNRS, Paris, pp. 27-52.

Coustols, E., and Cousteix, J., 1994. 'Performances of riblets in the supersonic regime'. *American Institute of Aeronautics and Astronautics (AIAA) Journal*, Vol. 32 (2), pp. 431–433.

Coustols, E. and Savill, A. M., 1992. 'Turbulent skin-friction drag reduction by active and passive means: Part I. In Skin friction drag reduction'. *Advisory Grow for Aerospace Research and Development (AGARD Rep.),* Vol.786, pp. 8.1–8.53.

References

Crawford, C. H., 1996. 'Direct numerical simulation of near-wall turbulence: passive and active control'. PhD Thesis. Princeton Univ., New Jersey, USA.

Daoud, M. I., 2004. 'Stochastic estimation of the flow structure downstream of a separating/reattaching flow region using wall-pressure array measurements'. PhD Thesis, Michigan State University, USA.

Dean, B. D., 2011. 'The effect of shark skin inspired riblet geometries on drag in rectangular duct flow'. PhD Thesis. The Ohio State University, USA.

DeGraaff, D. B., and Eaton, J. K., 2000. 'Reynolds-Number scaling of the flat-plate turbulent boundary layer'. *Journal of Fluid Mechanics*, Vol.422, pp. 319-346.

DeGraaff, D. B., 1999. 'Reynolds-Number scaling of the boundary layer on a flat plate and on swept and unswept bumps'. PhD Thesis, Stanford University, USA.

Djenidi, L., Dubief, Y., and Antonia, R. A., 1997. 'Advantages of using a power law in low Re boundary layers'. *Experiments in Fluids*, Vol.22**,** pp. 348-350.

Djenidi, L., 1991. 'Riblet flow prediction with a low-Reynolds-number k-e model'. 6th European Drag Reduction Working Meeting, abstract.

Djenidi, L., Squire, L. C. and Savill, A. M., 1990. 'High resolurion conormal mesh computation for V, U and L-groove riblets in laminar and turbulent boundary layer'. In Recent Development in *Turbulence Management*, K. S. Choi, ed., Kluwer, Dordrecht, pp.65-92.

Duan, L. and Choudhari, M. M., 2012. 'Effects of riblets on skin friction in high-speed turbulent boundary layers'. 50th *AIAA* Aerospace Sciences Meeting.

Dubief, Y., Djenidi, L. and Antonia, R. A., 1997. 'The measurement of $\partial u/\partial y$ in a turbulent boundary layer over a riblet surface'. *International Journal of Heat and Fluid Flow,* Vol.18, pp.183-187.

Gad-el-Hak, M., and Bandyopadhyay, P. R., 1994. 'Reynolds number effects in wall bounded turbulent flows'. *Appl. Mech. Rev.* Vol.47 (8), 307–365.

Gruneberger, R., Hage, W., 2011. 'Drag characteristics of longitudinal and transverse riblets at low dimensionless spacings'. *Experiments in Fluids*, Vol. 50, pp. 363–373.

El-Samni, O. A., Chun, H. H. and Yoon, H. S., 2007. 'Drag reduction of turbulent flow over thin rectangular riblets'. *International Journal of Engineering Science,* Vol.45, pp. 436–454.

Engin, S., and Altintas, Y., 2001. 'Generalized modeling of mechanics and dynamics of milling cutters'. *Annals of the CIRP*, Vol.50 (1), pp. 25-30.

Etsion I., Brizmer V., Klingerman Y., 2003. 'A laser Surface textured parallel trust bearing'. *Tribology Transactions*, Vol.46 (3), pp. 397-403.

Etsion I., Ronen A., 2001. 'Friction reduction surface texturing in reciprocation automotive components'. *Tribology International*, Vol.44, pp. 359–366.

Etsion I., Klingerman Y., 1998. 'Analytical and experimental investigation of laser-textured mechanical seal faces'. *Tribology Transactions*, Vol.42 (3), pp. 511-516.

Franzoni, L. P. and Elliott, C. M., 1998. 'An innovative designs of a probe-tube attachment for a ½-in. microphone'. *Journal of Acoustical Society of America*, Vol.104, pp. 2903–2910.

Fernholz, H. H., and Finley, P. J., 1996. 'The incompressible zero-pressure gradient turbulent boundary layer: an assessment of the data'. *Progress in Aerospace Sciences,* Vol.32, pp. 245-311.

Fernholz, H. H., Krause, E., Nockemann, M., and Schober, M., 1995. 'Comparative measurements in the canonical boundary layer at Reynolds 6 × 10^4 on the wall of the DNW'. *Physics of Fluids A*, Vol.7, pp. 1275-1281.

Finley, P. J., Chong, P. K., and Chin, J. P., 1966. 'Velocity measurements in a thin turbulent wake layer'. *La Houille Blanche*, Vol.21, pp. 713-721.

Fischer, S., 2000. 'Fertigungssysteme zur spanenden Herstellung von Mikrostrukturen'. Dr.-Ing. Dissertation, RWTH, Aachen.

Fowell, M., Olver, A.V., Gosman, A.D., Spikes, H.A., and Pegg, I., 2007. 'Entrainment and Inlet Suction: Two mechanisms of hydrodynamic lubrication in textured bearings'. *Transaction of the ASME: Journal of Tribology*, Vol.129 (2), pp. 336-348

Gallager, J. A. and Thomas, A. S. W., 1984. 'Turbulent boundary layer characteristics over steam-wise grooves'. *American Institute of Aeronautics and Astronautics (AIAA)*, paper 84-2185.

Garcıa-Mayoral, R., 2011. 'The interaction of riblets with wall-bounded turbulence'. PhD Thesis, Stanford University, USA.

References

García-Mayoral, R., and Jiménez, J., 2012. 'Drag reduction by riblets'. *Philosophical Transactions of the Royal Society*, Vol.369, pp. 1412–1427.

Gaudet, L., 1987. 'An assessment of the drag reduction properties of riblets and the penalties of off-design conditions'. *Royal Aircraft Establishment Farnborough*, England, ADA194003.

Gaudet, L., 1989. 'Properties of riblets at supersonic speed'. *Applied Scientific Research*, Vol.46 (3), pp. 245–254.

GEC Alsthom, 1991. 'Industrial applications of drag reduction to the French high speed trains (TGV)'. Abstract, 6th European *drag reduction* meeting, Eindhoven.

George, W. K., and Castillo, L., 1997. 'Zero pressure gradient turbulent boundary layer'. *Applied Mechanics Review,* Vol.50, pp. 689-729.

Goldstein, D. B., Handler, R., and Sirovich, L., 1995. 'Direct numerical simulation of turbulent flow over a modelled riblet covered surface'. *Journal of Fluid Mechanics,* Vol.302, pp. 333–376.

Goldstein, D. B., and Tuan, T. C., 1998. 'Secondary flow induced by riblets'. *Journal of Fluid Mechanics,* Vol.363, pp. 115–151.

Granola, H., Murcsy-Milian, H., and Tamasch, F., 1991. 'Errors, truncation and other deleterious effects in fluid dynamical research'. *Proceeding Conference of Loss Mechanisms in Aeronautics*, April, Brunswick, Maine, USA.

Granville, P. S., 1976. 'A modified law of the wake for turbulent shear layers'. *Transactions of the ASME: Journal of Fluids Engineering*, Vol.29, pp. 578-580.

Hahn, S., Je, J., and Choi, H., 2002. 'Direct numerical simulation of a turbulent channel flow with permeable walls'. *Journal of Fluid Mechanics,* Vol.450, pp. 259–285.

Han, X., Wang, J., Zhang, D., 2010. 'Bio-replicated Forming of the Biomimetic Drag-reducing Surface based on Underwater Low-resistance Scarfskin's. Proceedings of the *IEEE*, International Conference on Mechatronics and Automation, August 4-7, 2010, Xi'an, China.

Hanratty, J., Chornl, G., and Hatziavramdid, TIS., 1977. 'Turbulent fluctuations in the viscous wall region for Newtonian and drag reducing fluids'. *Physics of Fluids,* Vol.20, S112.

References

Hatman, A., and Wang, T., 1998. 'A prediction model for separated-flow transition'. *ASME,* Paper No. 98-GT-237.

Head, M. R., and Bandyopadhyay, P., 1981. 'New aspects of turbulent boundary-layer structure. *Journal of Fluid Mechanics*, Vol.107, pp. 297–338.

Hirt, G., and Thome, M., 2007. 'Large area rolling of functional metallic micro structures'. *Production Engineering Research and Development*, Vol. 1, pp .351–356.

Hooshmand, A., Youngs, R. A., Wallace, J. M. and Balint, J. L., 1983. 'An experimental study of changes in the structure of a turbulent boundary layer due to surface geometry changes'. *American Institute of Aeronautics and Astronautics (AIAA)*, paper 83-0230.

Hosni, M. H., Coleman, H. W., Gardner, J. W., and Taylor, R. P., 1993. 'Roughness element shape effects on heat transfer and skin friction in rough wall turbulent boundary layers'. *International Journal of Heat and Mass Transfer*, Vol.36, pp. 147-153.

ISO 4287: 1997. Geometrical product specifications (GPS) – surface texture: profile method - terms, definitions and surface texture parameters.

Itoh, M., Tamano, S., Iguchi, R., Yokota, K., Akino, N., Hino, R. and Kubo, S., 2006. 'Turbulent drag reduction by the seal fur surface'. *Physics of Fluids,* Vol.18 (6), 065102.

Jim´enez, J., 1992. 'Wall friction and the structure of near-wall turbulence'. *In 11th Australasian Fluid Mech. Conf.* (ed. M.R. Davis & G.J. Walker), pp. 813–816. Hobart, Australia.

Jim´enez, J. and Moin, P., 1991. 'The minimal flow unit in near-wall turbulence'. *Journal of Fluid Mechanics,* Vol.225, pp. 213–240.

Jim´enez, J., and Pinelli, A., 1999. 'The autonomous cycle of near wall turbulence'. *Journal of Fluid Mechanics,* Vol.389, pp. 335–359.

Jimenez, J., Uhlman, M., Pinelli, A., and Kawahara, G., 2001. 'Turbulent shear flow over active and passive porous surface's. *Journal of Fluid Mechanics,* Vol.442, pp. 89–117.

Jung, W.J., Mangiavacchi, N., and Akhavan, R., 1992. 'Suppression of turbulence in wall-bounded flows by high-frequency span-wise oscillations'. *Physics of Fluids A,* Vol.4, pp. 1605–1607.

Kang, S., 2008. 'An improved boundary method for computation of turbulent flows with heat transfer'. PhD Thesis. Stanford University, USA.

Khan, M. M. S., 1986. 'A numerical investigation of the drag reduction by riblet surfaces'. *American Institute of Aeronautics and Astronautics (AIAA)*, paper 86-1127.

Karniadakis, G. E., and Choi, K. S., 2003. 'Mechanisms on transverse motions in turbulent wall flows'. *Annual Review of Fluid Mechanics*, Vol.35, pp. 45–62.

Karniadakis, G. E., Israeli, M. and Orszag, S. A., 1991. 'High-order splitting methods for the incompressible Navier-Stokes equations'. *Journal of Computational Physics*, vol.97, pp. 414.

Kim, II. T., Kline, S. J. and Reynolds, W. C., 1971. 'The production of turbulence near a smooth wall in a turbulent boundary layer'. *Journal of Fluid Mechanics,* Vol.50, pp. 133-160.

Kim, J., Moin, P., and Moser, R., 1987. 'Turbulence statistics in fully developed channel flow at low Reynolds number'. *Journal of Fluid Mechanics,* Vol.177, pp. 133-166.

Klebanoffr, P. S. and Diehl, Z. W. 1951. 'Some features of artificially thickened fully developed turbulent boundary layers with zero pressure gradient'. *National Advisory Committee for Aeronautics,* Wash., Technical Note no. 2475.

Klocke, F., and Feldhaus, B., 2007. 'Development of an incremental rolling process for the production of defined riblet surface structures'. *Sebastian Mader Prod*. Eng. Res. Devel, Vol.1, pp.233–237.

Kong, F. Y., and Schetz, J. A., 1982. 'Turbulent boundary layer over porous surfaces with different geometries'. *American Institute of Aeronautics and Astronautics (AIAA)*, Paper 82-0030.

Kraker D. A., Ostayen R. A. J. van B., Rixen D. J., 2010. 'Development of a texture averaged Reynolds equation'. *Tribology International*, Vol.43, pp. 2100–2109.

Kramer, M. O., 1937. 'Einrichtung zur Verminderung des Reibungswiderstandes'. Patentschrift 669897, Klasse 62b, Gruppe 408. March 17.

References

Krogstad, P. A., Antonia, R. A., and Browne, L. W. B., 1992. 'Comparison between rough and smooth wall turbulent boundary layers'. *Journal of Fluid Mechanics*, Vol.245, pp. 599-617.

Lai, X., Li, H., Li C., Lin, Z., and Ni, J., 2008. 'Modelling and analysis of micro scale milling considering size effect, micro cutter edge radius and minimum chip thickness'. *International Journal of Machine Tools and Manufacture*. Vol.48 (1), pp. 1–14.

Launder, B. E., and Li, S. P., 1991. 'Prediction of drag reduction by riblet'. *Presentation at the 6th Drag Reduction Meeting*, Eindhoven.

Launder, B. E., and Li, S. P., 1993. 'On the prediction of riblet performance with engineering turbulence Models'. *Applied Scientific Research,* Vol.50, pp. 283-298.

Lee, K., and Dornfeld, D. A., 2005. 'Micro-burr formation and minimization through process control'. *Precision Engineering*, Vol.29 (2), pp. 246–252.

Lee, p., and Altintas, Y., 1996. 'Prediction of ball-end milling forces from orthogonal cutting data'. *International Journal of Machine Tools and Manufacture*, Vol.36 (9), pp. 1059-1072.

Lee, S. J., and Jang, Y. G., 2005. 'Control of flow around a NACA 0012 airfoil with a micro-riblet film'. *Journal of Fluids and Structures*, Vol.20, pp. 659–672.

Lee, S. J., and Lee, S. H., 2001. 'Flow field analysis of a turbulent boundary layer over a riblet surface'. *Experiments in Fluids,* Vol.30, pp. 153–166.

Liu, X., DeVor, R. E., and Kapoor, S. G., 2004. 'The mechanics of machining at the microscale: assessment of the current state of the science'. *Journal of Manufacturing Science and Engineering*, Vol.126, pp. 666-678.

Lu, S., Willmarth, W. 1973. 'Measurements of the structure of the Reynolds stress in a turbulent boundary layer'. *Journal of Fluid Mechanics*, Vol.60, pp. 481–511.

Luchini, P., Manzo, F. and Pozzi, A., 1991. 'Resistance of a grooved surface to parallel flow and cross-flow'. *Journal of Fluid Mechanics*, Vol.228, pp. 87–109.

Luchini, P. and Pozzi, A., 1997. 'Computation of three-dimensional stokes flow over complicated surfaces (3d riblets) using a boundary-independent grid and local corrections'. 10th European *Drag Reduction* Meeting, Berlin.

Luchini, P., and Trombetta, G., 1995. 'Effects of riblets upon flow stability'. *Journal of Applied Sciences Research*, Vol.54, pp. 313-321.

Luchini, P., Manzo, F., and Pozzi, A., 1992. 'Viscous eddies over a grooved surface computed by a Gaussian-integration Galerkin boundary-element method'. *American Institute of Aeronautics and Astronautics (AIAA) Journal.,* 30 (8), 2168-2170.

Luo, X., 2004. 'High precision surfaces generation: modelling, simulation and machining verification'. PhD Thesis. Leeds and Metropolitan University, USA.

Marian, G. V., Kilian, M., and Scholz, W., 2007. 'Theoretical and experimental analysis of a partially textured thrust bearing with square dimples'. *Journal of Engineering Tribology*, Vol.221, pp. 771–8.

McLean, J. D., Georg-Falvy, D. N. and Sullivan, P., 1987. 'Flight test of turbulent skin friction reduction by riblets'. *Conf. on turbulent drag reduction by passive means*, pp. 408-48.

Millikan, C. M., 1938. 'A critical discussion of turbulent flows in channel and circular tubes'. *In Proc. 5th International Congress on Applied Mechanics*, Wiley, New York, pp. 386-392.

Nanbu, T., Ren, N., Yasuda, Y., Zhu, D., and Wang, Q. J., 2008. 'Micro-textures in concentrated conformal-contact lubrication: effects of texture bottom shape and surface relative motion. *Tribology Letters*, Vol.29, pp. 241–252.

Nikuradse, J., 1932. 'Stromungsgesetze in rauhen rohen. ForschHft Ver'. Dt. Ing 361.

Osaka, H., Kameda, T., and Mochizyki, S., 1998. 'Re-examination of the Reynolds Number effects on the mean flow quantities in a smooth wall turbulent boundary layers'. *The Japan Society of Mechanical Engineers,* International Journal Series B, Vol.41 (5), pp. 802-811.

Österlund, J. M., 1999. 'Experimental studies of zero pressure-gradient turbulent boundary-layer flow'. PhD Thesis. Royal Institute of Technology Department of Mechanics, SE-100 44 Stockholm, Sweden.

Österlund, J. M., Johansson, A. V., Nagib, H. M., and Hites, M. H., 2000. 'A note on the overlap region in turbulent boundary layers'. *Physics of Fluids*, Vol.12, pp. 1-4.

Panton, R. L., 1990. 'Scaling turbulent wall layers'. *Transactions of the ASME: Journal of Fluids Engineering,* Vol.112, pp. 425-432.

Panton, R. L., 2000. 'Power law or log law, that is not the question'. *Bulletin of American Physical Society*, Vol.45, pp. 160.

Park, S. R., and Wallace, J. M., 1994. 'Flow alteration and drag reduction by riblets in a turbulent boundary layer'. *American Institute of Aeronautics and Astronautics (AIAA) Journal*, Vol.32 (1), pp. 31–38.

Peet, Y., Sagaut, P., and Charron, Y., 2009. 'Pressure loss reduction in Hydrogen pipelines by surface restructuring'. *International Journal of Hydrogen Energy,* Vol.34, pp. 8964-8973.

Pei S., Ma S., Xu H., Wang F., and Zhang Y., 2011. 'A multi-scale method-of modelling surface texture in hydrodynamic regime'. *Tribology International*, Vol.44, pp. 1810–1818.

Peskin, C. S., 1982. 'The fluid dynamics of heart valves: Experimental, theoretical, and computational methods'. *Annual Review of Fluid Mechanics,* Vol.14, pp. 235-259.

Perry, A. E., Schofield, W. H., Joubert, P., 1969. 'Rough wall turbulent boundary layers'. *Journal of Fluid Mechanics*, Vol.37, pp. 383–413.

Perry, A. E., Lim, K. L., and Henbest, S. M., 1987. 'An experimental study of the turbulence structure in smooth- and rough-wall boundary layers'. *Journal of Fluid Mechanics*, Vol.177, pp. 437-466.

Pollard, A., 1998. 'Near-wall turbulence control'. *Springer*, pp. 431-466.

Prandtl, L., 1954. 'Zeitschrift für Angewandte Mathematik und Physik'. Vol.5.

Prandtl, L. 1932. 'Zur Turbulenten Strömung in Roren und langs Plätten, Ergeb Aerod Versuch Gottingen'. IV Lieferung, 18 (in German).

Pulles, C. J. A., Prasad, K. K. and Nieuwstadt, F. T. M., 1989. 'Turbulence measurments over longitudinal micro-grooved surfaces'. *Applied Scientific Research*, Vol. 46, pp.197.

Robert, J. F., 1992. 'Drag reduction: an industrial challenge in Skin friction drag reduction'. *AGARD Rep*., Vol.786, pp. 2.1–2.15.

Robinson, S. K., 1988. 'Effects of riblets on turbulence in a supersonic boundary layer'. *American Institute of Aeronautics and Astronautics (AIAA)*, paper 88-2526.

References

Rotta, J. C., 1962. 'Turbulent boundary layers in incompressible flow'. *Prog. Aeronaut. Sci.*, Vol.2, pp. 1-220.

Sagrado, A. G., 2007. 'Boundary layer and trailing edge noise sources'. PhD Thesis, University of Cambridge, UK.

Sareen, A., 2012. 'Drag reduction using riblet film applied to airfoils for wind turbines'. PhD Thesis, University of Illinois, USA.

Sawyer, W. G., and Winter, K.G., 1987. 'Turbulent skin friction of surfaces with stream-wise grooves'. *Conf. turbulent drag reduction by passive means*, London, pp. 330-362.

Sawyer W.G., and Winter K.G., 1987. 'An investigation of the effect on turbulent skin friction of surfaces with stream-wise grooves, in turbulent drag reduction by passive means'. Con. 15-17 Sept., London, *UK Royal Aeronautical Society*.

Schlichting, H., 1968. 'Boundary-Layer Theory', 6th Edition, *McGraw-Hill*, New York.

Schlichting, H., 1979. 'Boundary-Layer Theory', 7th Edition, *McGraw-Hill*, New York.

Schlichting, H., and Gersten, K., 2000. 'Boundary Layer Theory', *Springer*, 8th revised and enlarged edition;

Schoppa, W., and Hussain F., 2002. 'Coherent structure generation in near-wall turbulence'. *Journal of Fluid Mechanics*, Vol.453, pp. 57–108.

Schultz-Grunow, F., 1941. 'New frictional resistant law for smooth plates'. *National Advisory Committee for Aeronautics*, TM 986. Vol.17 (8), pp. 239-246

Schwarz-van Manen, A. D., Hoogsteen, R., Stouthart, J. C., Krishna Prasad, K., and Nieuwstadt, F. T. M., 1990. 'Coherent structures over drag reduction surfaces'. Proc. 12 Symp. On *Turbulence*, University of Missouri_Rolla, pp. 93-112.

Seo, J., 2003. 'Investigation of the upstream conditions and surface roughness in turbulent boundary layer'. PhD Thesis, Department of Mechanical and Aeronautical Engineering, Rensselaer Polytechnic Institute, NY.

Seo, J., Castillo, L., Johansson, T. G., and Hangan, H., 2004. 'Reynolds stress in turbulent boundary layers at high Reynolds Number'. *Journal of Turbulence*, Vol.5, pp. 1-22.

Sheng, J., Malkieland, E., and Katz, J., 2009. 'Buffer layer structures associated with extreme wall stress events in a smooth wall turbulent boundary layer'. *Journal of Fluid Mechanics*, Vol.633, pp. 17–60.

Siegel, F., Klug, U., Kling, R., Ostendorf, A., 2008. 'Extensive micro-structuring of metals using picosecond pulses—ablation behavior and industrial relevance'. in: Proceedings of the LPM 2008, 9th International Symposium on Laser Precision Manufacturing (17–20 June, Quebec, Canada).

Smits, A. J., and Wood, D. H., 1985. 'The response of turbulent boundary layers to sudden perturbations'. *Annual Review of Fluid Mechanics*, Vol.17, pp. 321–358.

Smith, C. R., and Metzler, S. P., 1983. 'The characteristics of low-speed streaks in the near-wall region of a turbulent boundary layer'. *Journal of Fluid Mechanics*, Vol.129, pp. 27-54.

Smits, C. R., Walker, J. D. A., Haidari, A. H., and Taylor, B. K., 1989. 'Hairpin vortices in turbulent boundary layers: the implications for reducing surface drag'. *Proc. IUTAM Symp*. On Structure of Turbulent and Drag Reduction. Zurich, Springer-Verlag. Ann. pp. 51-58.

Stachomiak G. W., and Batchelo, A. W., 2005. 'Engineering Tribology', *Butterworth-Heinemann*, third edition.

Starling, I., and Choi, K. S., 1997. 'Non-linear laminar-turbulent transition over riblets. Proceedings of the Laminar Flow Workshop', Queen Mary and Westfield College, London.

Stout, K. J., Davis, E. J., and Sullivan, P. J., 1990. 'Atlas of Machined Surfaces', Chapman and Hall, London.

Stout K. J., 2000. 'Development of Methods for the Characterisation of Roughness in Three Dimensions', London, Penton Press.

Suzuki, Y. and Kasagi, N., 1994. 'Turbulent drag reduction mechanism above a riblet surface'. *American Institute of Aeronautics and Astronautics (AIAA) Journal*, Vol.32 (9), pp. 1781–1790.

Szodruch, J., 1991. 'Viscous drag reduction on transport aircraft'. *American Institute of Aeronautics and Astronautics (AIAA),* paper 91-0685.

Tachie, M. F., Bergstrom, D. J., and Balachandar, R., 2003. 'Roughness effects in low- Re open-channel turbulent boundary layers'. *Experiments in Fluids*, Vol.35, pp. 338-346.

Tachie, M. F., Bergstrom, D. J., Balachandar, R., and Ramachandran, S., 2001. 'Skin friction correlation in open channel boundary layers'. *Transactions ASME Journal of Fluids Engineering*, Vol.123, pp. 953-956.

Tala-Ighil, N., Fillon, M., Maspeyrot, P., 2010. 'Effect of textured area on the performances of a hydrodynamic journal bearing'. *Tribology International*, Vol.44 (3), pp.211-219.

Tang, Y. P. and Clark, D. G., 1992. 'On near wall turbulence-generating events in a turbulent boundary layer on a riblet surface'. *6th European drag reduction meeting*, Eindhoven.

Tani, I., 1988. 'Drag reduction by riblet viewed as a roughness problem'. *Proceedings of Japan Academy*, Vol.64, Se. B, No.2, pp. 21-24.

Tennekes, H. and Lumley, J. L. 1972. 'A first course in turbulence'. MIT Press, Cambridge, USA.

Tomboulides, A. G., Israeli, M., and Karniadakis, G. E., 1989. 'Efficient removal of boundary- divergence errors in time-splitting methods'. *Journal of Scientific Computing*, vol.4, pp. 291.

Townsend, A. A., 1956. 'The Structure of Turbulent Shear Flow'. Great Britain: Cambridge University Press.

Townsend, A. A., 1961. 'Equilibrium layers and wall turbulence'. *Journal of Fluid Mechanics,* Vol.11, pp. 97–120.

Tullis, S. W. J., 1992. 'Modelling the time dependent flow over riblets in the near wall region'. MSc Thesis, Department of Mechanical Engineering, Queen's University at Kingston, Canada.

Tullis, S., and Pollard, A., 1994. 'The time dependent flow over v and u groove riblets of different sizes'. *Physics of Fluids A*, Vol.6(2), pp. 1000-1001.

Tullis, S., and Pollard, A., 1993. 'Modelling the time dependent flow over riblets in the viscous wall region'. *Applied Scientific Research,* Vol.50, pp. 299-314.

Uhlmann, E., Piltz, S., Doll, U., 2004. 'Funkenerosion in der Mikrotechnik. Einsatzgebiete und Verfahrensgrenzen'. *Werkstatttechnik wt*-online, V (12), pp. 733–737.

Vathylakis, V., and Chong, T. P., 2013. 'On the turbulent boundary layers developed on flat plate with a serrated trailing edge'. *American Institute of Aeronautics and Astronautics (AIAA)* conference, pp.16.

Viswanath, P. R., 2002. 'Aircraft viscous drag reduction using riblets'. *Progress in Aerospace Sciences*, Vol.38, pp. 571–600.

Vukoslavcevic, P., Wallace, J. M., and Balint, J. L., 1992. 'Viscous drag reduction using stream-wise aligned riblets'. *American Institute of Aeronautics and Astronautics (AIAA) Journal,* Vol.30, pp. 1119–1122.

Vukoslavcevie, P., Wallace, J. M., and Balint, J. L., 1987. 'On the mechanism of viscous drag reduction using stream-wise aligned riblets: a review with new results'. *Proc. RAeS Int. Conf*. Turbulent drag reduction by passive means, London, pp. 290-309.

Walsh, M. J., 1980. 'Drag characteristics of V-groove and transverse curvature riblets'. *Progress in Astronautics and Aeronautics*, Hough, G.R. (ed.), Vol.72, pp. 168-184.

Walsh, M. J., 1982. 'Turbulent boundary layers drag reduction using riblets'. *American Institute of Aeronautics and Astronautics (AIAA)*, Paper 82, 0169.

Walsh, M. J., 1983. 'Riblets as a viscous drag reduction technique'. *American Institute of Aeronautics and Astronautics (AIAA) Journal*, Vol.21, pp. 485.

Walsh, M. J., 1990. 'Effect of detailed surface geometry on riblet drag reduction performance'. *Journal of Aircraft,* Vol.27 (6), pp. 572–573.

Walsh, M. J., and Lindemann, A. M., 1984. 'Optimization and application of riblets for turbulent drag reduction'. *American Institute of Aeronautics and Astronautics (AIAA),* paper 84-0347.

Walsh, M. J., Sellers, W. L., and McGinley, C. B., 1989. 'Riblets drag at flight conditions'. *ournal of. Aircraft*, Vol.26 (6), pp. 570-575.

Walsh, M. J., and Weinstein, L. M., 1978. 'Drag and heat transfer on surfaces with small longitudinal fins'. *American Institute of Aeronautics and Astronautics (AIAA)*, paper 78-1161.

Wang, B., Kohler, J., Berend, D., 2010. 'Manufacturing of functional riblet structures by profile grinding'. CIRP *Journal of Manufacturing Science and Technology*, V (3), pp. 14–26.

References

Weiss, M. H., 1997. ‘Implementation of drag reduction techniques in natural gas pipelines’. presented at 10th European *Drag Reduction* Working Meeting, Berlin, Germany, March 19-21.

White, F. M., 1974. ‘Viscous Fluid Flow’. McGraw-Hill, New York.

Wilkinson, S. P., Anders, J. B., Lazos, B. S., and Bushnell, D. M., 1987. ‘Turbulent drag reduction research at NASA Langley: progress and plans’. *International Journal of Heat and Fluid Flow*, Vol.9, pp. 266-277.

Zagarola, M. V., and Smits, A. J., 1998. ‘A new mean velocity scale for turbulent boundary layers’. *ASME*, paper FEDSM98-4950.

Zagarola, M. V., Perry, A. E., and Smits, A. J. 1997. ‘Log laws or power law: the scaling in the overlap region’. *Physics of Fluids*, Vol.9, pp. 2094-2100.

Zhaoa, D. Y., Huanga, Z. P., Wanga, M. J., Wangb, T., Jin Y., 2010. ‘Vacuum casting replication of micro-riblets on shark skin for drag-reducing applications’. *Journal of Materials Processing Technology*, Vol. 212, pp. 198– 202.

Zuniga, F. A., Anderson, B. T., and Bertelrud, A., 1992. ‘Flight test results of riblets at supersonic speeds’. *NASA Technical Paper,* pp. 4387.

Alicona 3D profiler, 2013. Available at: <http://www.alicona.co.uk/home/products/infinitefocus-standard.html>, (Accessed: 10 December 2013).

Michigan Metrology, 2010. Available at: < http://www.michmet.com/>, (Accessed: 10 November 2010).

Polytec, 2012. Available at: <http://www.polytec.com/uk/>, (Accessed: 12 December 2012).

Appendices

Appendix A

Design and modelling of micro-structured surfaces

Lubrication interfaces can be affected by the geometry of micro-scale textures and the relative motion of the surfaces in contact. A few researchers like Hamilton et al. 1966 and Anno et al 1968 have already proved that texturing of the surfaces can produce beneficial effects in seals and in parallel thrust bearing. Since 1966 this non classical lubrication has received attention from other research groups. Most research presented has concentrated on liquid lubricated mechanical components. This report considers gas (air) lubrication using incompressible laminar flow.

A.1 Introduction and background

The study of fluid dynamics interactions with solid can be classified in terms of the scale, compressibility, time dependency and method of the analysis. For instance, in terms of scale, it has been examined that the Navier-Stokes theory cannot be used to explain the flow behaviour, when the external characteristic length (i.e. film thickness, channel depth) becomes comparable with the internal characteristic length (i.e. molecular dimension). Experiments demonstrate, in channel depth of less than 30 nm, viscosity of some fluids is greater than bulk viscosity. In other words, near a solid wall, a thin layer (of the order of 5-10 nm) of fluid becomes rigid, which leads to decreasing the channel depth. In this condition, the long-range intermolecular forces and molecular packing effects must be taken into account. (Eringen, Okada, 1995)

Considering the method of analysis, most of the simulation methods in use have been developed for many years such as Finite Element Methods and Finite Volume Method. The selection of the modelling method is also related to the problem in hand. For instance, Lattice Boltzmann methods can be beneficial to those problems which have complicated geometrical boundary conditions. This solver considers flows to be composed of a collection of pseudo-particles that are represented by a velocity distribution function. These fluid portions reside and interact on the nodes of a grid. System dynamics and complexity emerge by the repeated application of local rules for the motion, collision and redistribution of these coarse-grained droplets. (Raabe, 2004)

Recently, some investigations have been done on Laser Surface Texturing (LST) on bearings by Etsion et al. In their case study they considered the trust bearing

(1996) and the mechanical seal faces (1998). In most of the presented work, two dimensional steady state form of the Reynolds equation for laminar and compressible fluid has been considered.

In 2006, they investigated the hydrostatic gas lubrication for parallel surfaces with micro-dimpled texturing. Their study focused on a single three-dimensional dimple, generated by LST, with two different methods of analysis. The pressure distribution and load carrying capacity gained by a numerical solution of the exact full Navier-Stokes equations, and an approximate solution of the much simpler Reynolds equation. They used Finite Different Method (ANSYS/Floutran) to solve the Reynolds equation for a hydrostatic compressible flow. It was concluded that the maximum difference in the pressure distribution between the two mentioned solutions occurs in the midsection of the dimple. In spite of this, the differences in load carrying capacity are insignificant (Feldman, Kligerman, Etsion and Haber, 2006).

Another research from this group (2003) focused on comparing two different LST concepts that can be used to produce load carrying capacity in parallel sliding. These concepts are full LST or partial LST. They found that full texturing is useful for developing the large load carrying capacity expected from a hydrodynamic thrust bearing. Also it can be beneficial in a very short slider bearing as is the case with mechanical seals. On the other hand for partial texturing, the effect is useful in finite and long sliders. They had another project on micro texturing surfaces in order to create micro pores to optimize tribological features of reciprocation automotive components. The results confirmed reducing friction.

Marian et al (2007) worked on partially texturing the inlet zone of a thrust washer. They created a thermo-hydrodynamic model to investigate the square dimples shape theoretically (fluid film thickness and friction torque) and experimentally (photolithographic method). On the numerical analysis their model was presented in cylindrical coordinates. “It is found that an optimal number of 12 sectors maximize the load carrying capacity of the bearing. The optimal textured fraction, which maximizes the load carrying capacity, is 0.5 on the circumferential direction and 0.9–1 on the radial direction”.

One of the interesting projects has been done by Fowell et al (2007). They identified an inlet suction that is applicable to low convergence, micro-pocketed bearings. For this mechanism, sliding of one of the bearing surfaces generates a sub-ambient pressure in pockets close to the bearing inlet. This can create different approach to the classical lubrication. By using analytical solution for simple pocketed bearings they calculated hydrodynamic load support and friction. The results show that “for the parallel case, inlet suction provides the only mechanism of hydrodynamic load support, and that inlet suction continues to play a major role in load support and friction reduction up to quite high convergence ratios”. They

believe that this mechanism is the reason that friction of textured bearings is reduced.

To improve the performance of bearing, Tala et al (2010) used different shapes of micro-cavities and various location of the patterned zone. As their case study they consider a journal bearing. Similar to other researcher they used a numerical modelling (FDM) to analyze the cylindrical texture shape. They results demonstrates that the micro-cavities increase locally the lubricant film thickness and decrease the friction forces.

Instead of Reynolds equation De Kraker et al (2010) applied Navier Stoke equation in order to capture the more complex flow pattern. They used multi-scale method for fluid flow in a single micro-scale texture unit cell, then the results of NV are averaged to flow factors to be used in a novel texture averaged Reynolds equation on the macro-scale bearing level.

Moreover, Toshikazu et al (2008) have conducted a numerical investigation to explore the effect of texture distribution on elasto-hydrodynamic lubrication (EHL) film Thickness. They tried to understand the effects of dimple size, and depth on surface interaction.

A.2 Challenges

Considering possible solutions on lubrication improvement, numerically generated textures by means of model-based virtual texturing and numerical simulation can determine the effect of different bottom shapes and density of the dimples on the surfaces. Also this study includes different surface motion, for instance texture surface moving, un-textured surface moving, and both moving. This type of research is numerically investigated by Computational Fluid dynamics (CFD). Different methods have been used such as FEM, FCM and FVM. As a computational need to receive the best numerical analysis, parallel computation (clusters) can be used in order to have a full solution.

To continue the investigation on surface texturing, it is important to continue the study into the relation between the load and the density of the dimples on the surfaces. Relation between pressure, load and friction affected by the number of created dimples can lead to optimised work done by bearings.

Moreover, most of the micro patterning on the bearing has been done by LST or photolithography. Although, LST is environmentally friendly and it can produce identical dimples at high surface density, micro milling can be a more economical option in many applications and can also deliver the same quality of work. Also, the discussion on the bottom shape texturing on bearings and seals by micro-milling is still not been investigated properly. Finally, reviewed articles demonstrate that the majority of the research in this area is focused on

incompressible fluids as lubricants. Consequently, a numerical analysis by computational fluid dynamics for compressible flow will guide this type of research to the next stage.

A.3 Theoretical analysis

For the first step, a theoretical model should be developed to study the effect of micro-milled surface texturing on an air bearing. On this analysis, to obtain maximum efficiency in terms of the ratio of load carrying capacity, the surface texturing parameters are numerically evaluated.

The following main assumptions are considered: the lubricant is a continuum and Newtonian fluid with no slip at the boundary walls, the flow is laminar, the fluid viscosity in the outlet boundary is considered without stress, and the fluid does not exchange heat with the walls (adiabatic model, temperature does not vary over the film thickness). For the preliminary models the stationary conditions have been considered for the simulations. In the regions of lubrication theory, the pressure is governed by the Reynolds equation and Navier Stokes equations (Stachomiak and Batchelo, 2005), first the Reynolds equation is expressed as follows:

$$\frac{\partial}{\partial x}\left(\frac{h^3}{\eta}\frac{\partial p}{\partial x}\right)+\frac{\partial}{\partial y}\left(\frac{h^3}{\eta}\frac{\partial p}{\partial y}\right)=6\left(U\frac{dh}{dx}+V\frac{dh}{dy}\right)+12(W_h-W_0) \quad (1)$$

Where h and p are local film thickness and pressure.

In order to obtain the dimensionless form of the above equation, the film thickness and the boundary conditions should be defined.

$$h=c\pm h_1(x,y) \qquad \sqrt{x^2+y^2}\le r_1 \quad (\pm\text{: in and out}) \quad (2)$$

$$h=c \qquad \sqrt{x^2+y^2}>r_1 \quad (3)$$

Where $h_1(x,y)$ depends on the dimple shape and size, c stands for the initial film thickness and $2r_1$ is the maximum width of the dimple.

In this thin film, the bottom wall is stationary and the upper wall is moving, V = V $(v_1, v_2, 0)$; also, the boundary condition for the selected case studies can be defined for the pressure in the Reynolds equation. Equation 1 is rendered dimensionless by using r_1 and c to scale length and Pa to scale the pressure field. Finally the linearized dimensionless Reynolds equation is as follows:

$$\frac{\partial}{\partial X}\left(H^3\frac{\partial P}{\partial X}\right)+\frac{\partial}{\partial Y}\left(H^3\frac{\partial P}{\partial Y}\right)=6\left(U\frac{dH}{dX}+V\frac{dH}{dY}\right) \quad (4)$$

The second type of analysis for the thin film and lubrication considers NS. The three dimensional NS equations for Newtonian ideal gas in a laminar flow, neglecting external forces are:

$$\rho u_i \frac{\partial u_i}{\partial x_i} = -\frac{\partial p}{\partial x_j} - \frac{\partial}{\partial x_j}\left(\frac{2}{3}\mu \frac{\partial u_i}{\partial x_i}\right) + \frac{\partial}{\partial x_i}\left[\mu\left(\frac{\partial u_i}{\partial x_j} + \frac{\partial u_j}{\partial x_i}\right)\right. \quad (5)$$

Since the flow is assumed to be isothermal, $\frac{p}{\rho}$=constant.

Also, the steady state continuity equation for compressible flow is as follows:

$$\frac{\partial}{\partial x_i}(\rho u_i) = 0 \quad (6)$$

Consequently, the total load supported by the bearing can be obtained by integrating the pressure distribution over the specific bearing area:

$$w = \int p dA = \iint p dx dy \quad (7)$$

Although the results found by Reynolds equations for the load capacity are reliable; In order to receive the precise solution for the lubrication theory in micro scale, the NS equation should be selected for the analysis.

A.4 Modelling

The NS equation with its appropriate boundary conditions is solved by the finite element method using COMSOL/MATLAB.

The dimples are considered to have different forms in order to find the most efficient shape. The comparison between the dimples shapes and their density has been done in Cartesian coordinates, but the bearing should be modelled in cylindrical coordinates. Two groups of dimples, circle and square are numerically generated. The surfaces of these shapes are assumed to be smooth.

2D modelling has been carried out for this comparison for hydrostatic condition (i.e. pressure inlet around 3 bar). Also, because at this stage the shapes mattered, the texture density, in terms of the area ratio of dimples centres over the nominal surface, is kept constant for all cases. The depth of dimples, for this comparison is also kept constant; although it should be determined later by optimization. At this stage, it has been considered to be equal with the radius of the dimples (i.e. 5µm). In addition, the initial film thickness is 7µm.

Appendix A

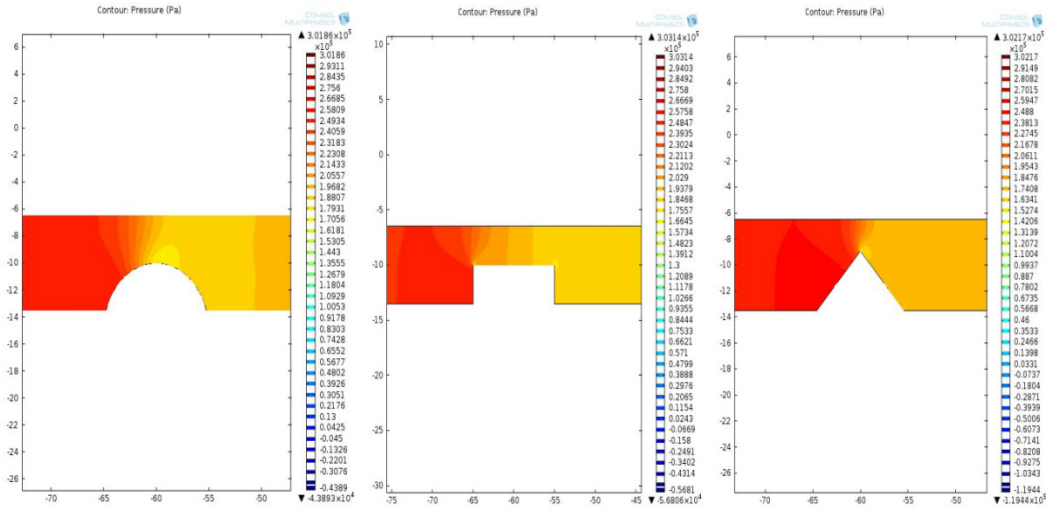

Figure 1: 2D modelling for different dimples' shapes

The moving wall has a velocity in the X direction (i.e. 100 m/s); the pressure distribution has been demonstrated in XY plane. Dimples with circle geometry resulted in more changes in pressure distribution (Fig 2); also the average generated pressure on the upper wall for this shape is quite close to the other cases.

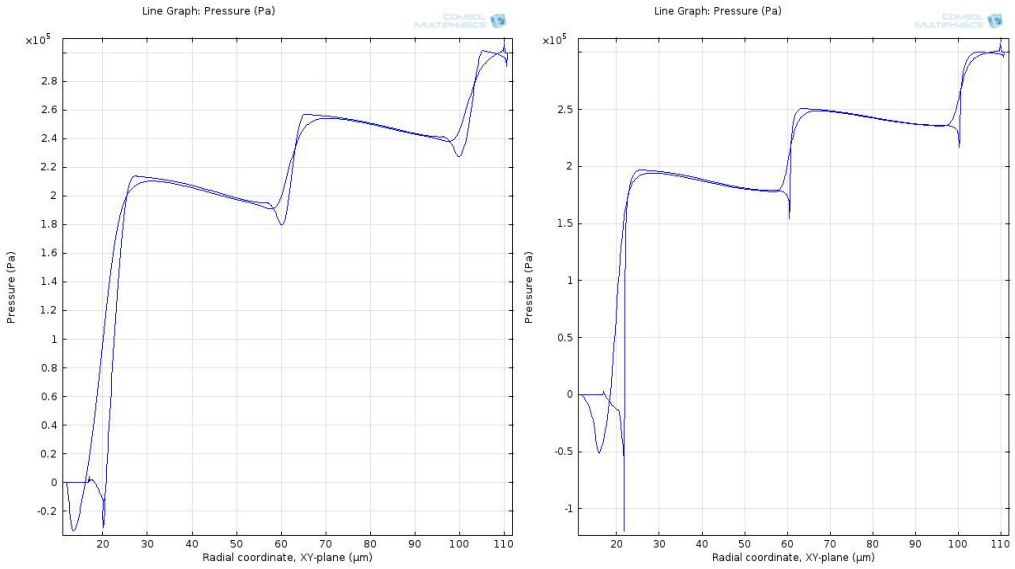

(a) (b)

Appendix A

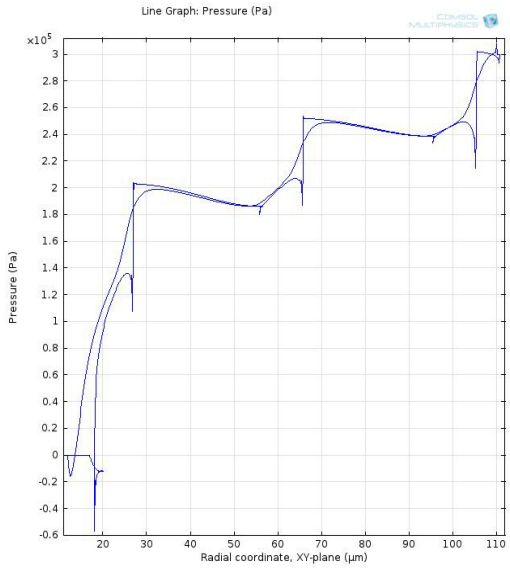

(c)

Figure 2: Pressure distribution (a) Circle shape (b) Cone shape (c) Square shape: this distribution follows the profile of the designed surfaces (three dimples have been modelled for each case)

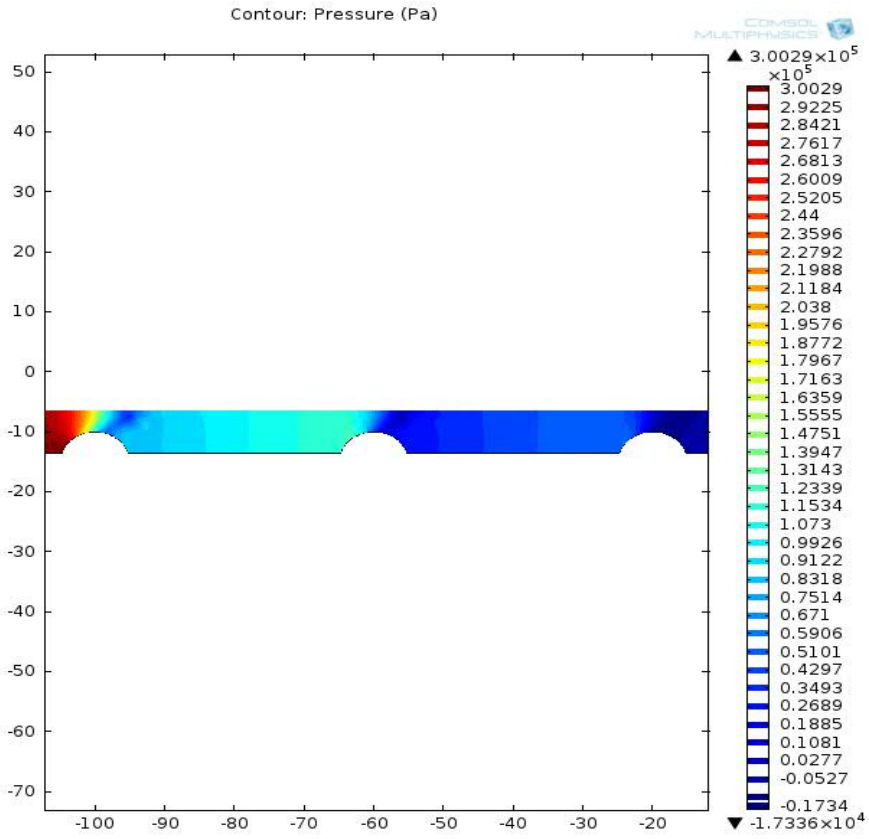

Figure 3: Contour Field of the air flow at the mid cross section of three dimples

Appendix A

Defining the shape of the dimples is the first step for this modelling. There are many factors which effect the pressure distribution on a thin film, such as the speed of the slider, the wedge, density distribution of the dimples (lattice size), the location of the dimples (clusters), and configuration (partially texturing).

The next level of this analysis is determination of the lattice sizes. Three dimensional modelling has been carried out for this investigation. The ratio of the dimples diameter and the distance between their centres considered with the lattice size coefficient, L. The distribution of the dimples on the surface of the bottom wall is not just important for pressure distribution, but it is essential in terms of the manufacturing and energy consumption.

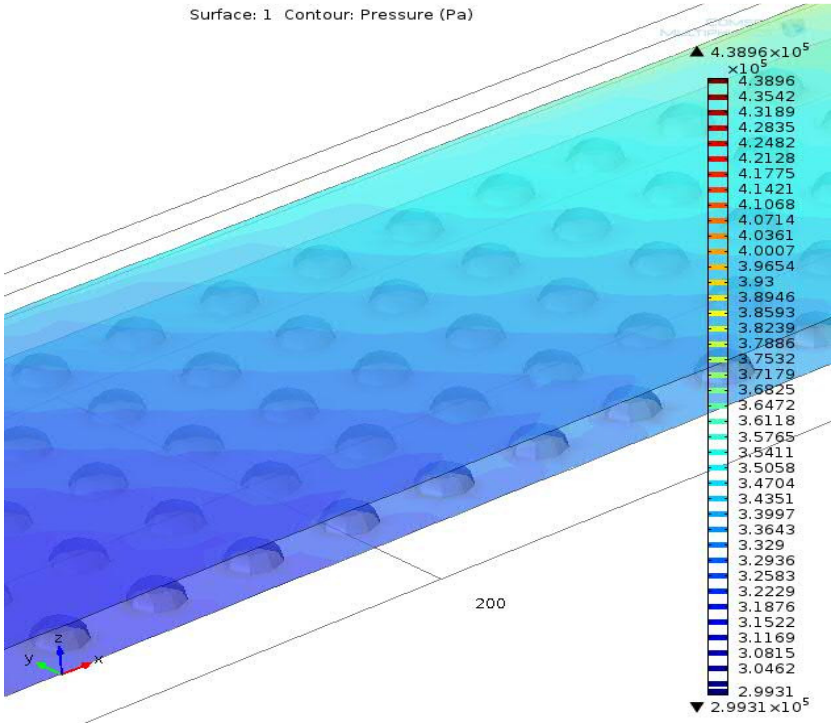

Figure 4: The air pressure distribution obtained from the NS equations for L=2

Initially 3 different lattice sizes have been examined (L=2, 3, 4), for a specific area which remains constant for all three models. The results show the smaller the L is, the higher pressure observed. (Figure 5, 6, 7)

Appendix A

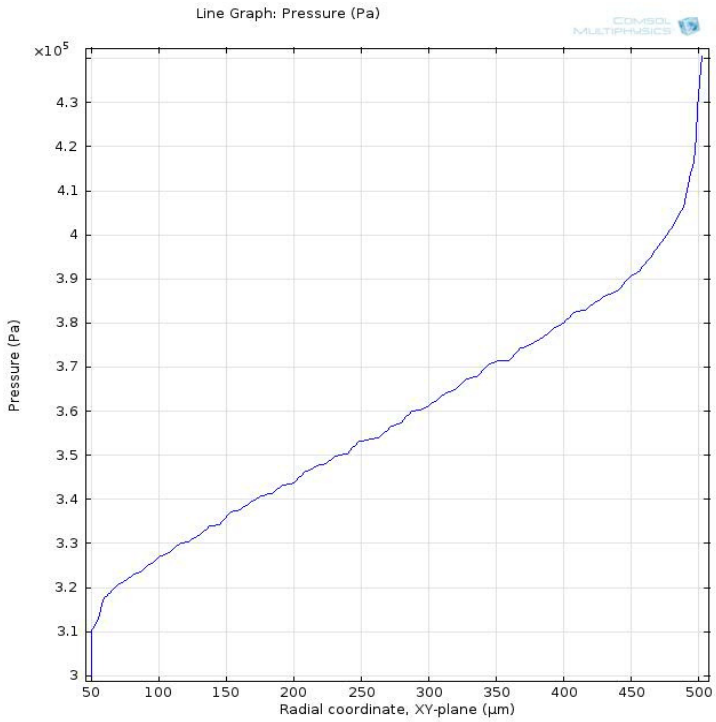

Figure 5: Pressure distribution on the boundary of the moving wall for L=2

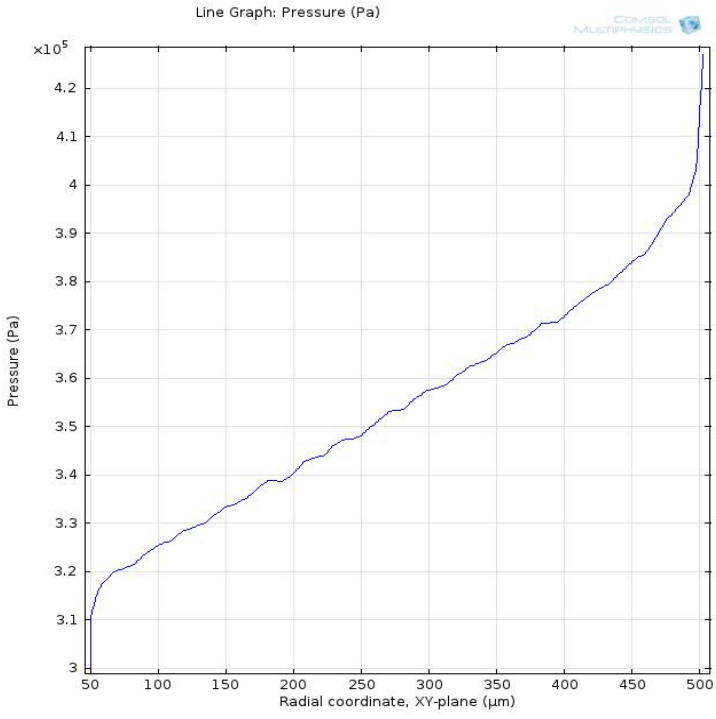

Figure 6: Pressure distribution on the boundary of the moving wall for L=3

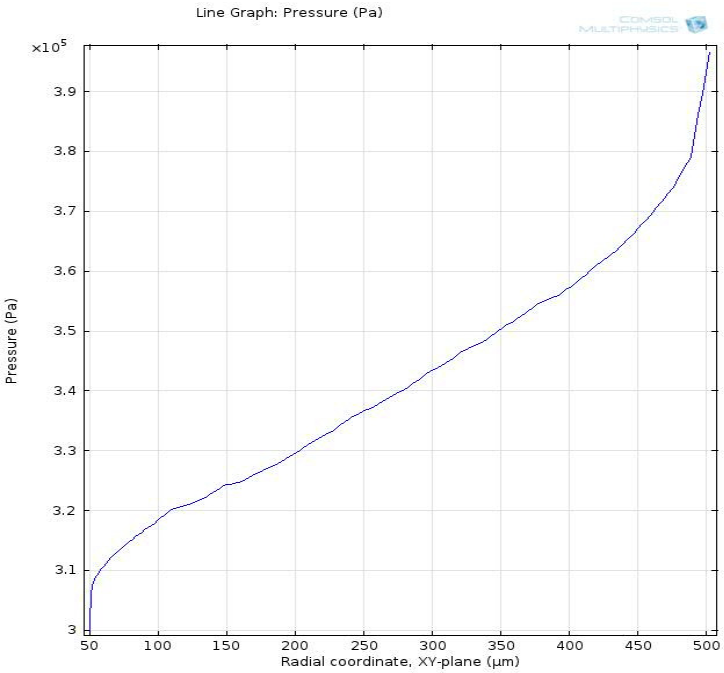

Figure 7: Pressure distribution on the boundary of the moving wall for L=4

Parameter optimization should be continued until all the important factors, such as the slip of the wedge, lattice sizes, clusters and configuration are fully investigated. After gaining a deeper understanding of these design elements, a completed model of the air bearing is ready for experiment. In addition, this investigation includes the hydrodynamic solutions. The primary modelling for this type of bearing shows the changes in the pressure distribution; but increasing the load capacity in the hydrodynamic study for air bearings needs a more complicated geometry design.

A.5 Conclusions

First, design and modelling of μ-textured functional surfaces carried out based on 2D and 3D surface characterisations. The μ-features modelled and designed regarding their shapes and density and their impacts on the performance of components (i.e. pressure distribution). Three different dimples' shapes have been examined; and the results demonstrate that the dimples with circle shape have higher pressure variation. To continue this part of project, in the design of high precision air bearing, the sizes and configuration (location) of μ-features or μ-texturing on bearing pads should be modelled and analysed by tribology theory and Navier Stokes equation.

Appendix B

Uncertainty analysis

B.1 General background

Measurement systems consist of the instrumentation, the procedures for data acquisition and reduction, and the operational environment. Measurements are made of individual variables, *xi*, to obtain a result, *R*, which is calculated by combining the data for various individual variables through data reduction equations as follows:

$$R = R(x_1, x_2, x_3, \dots \dots, x_n) \tag{1}$$

Each of the measurement systems used to measure the value of an individual variable, *xi*, is influenced by various elemental error sources. The effects of these elemental errors are manifested as bias errors, *Bi*, and precision errors, *Pi*, in the measured values of the variable, *xi*. These errors in the measured values then propagate through the data reduction equation, thereby generating the bias and precision errors in the experimental results. The effect of an uncertainty on any individual variable on the experimental result, *R*, may be estimated by considering the derivative of the data reduction equation (Coleman and Steele, 1999). A variation d*xi* (in *xi*) would cause *R* to vary according to:

$$\delta R_i = \frac{\partial R}{\partial x_i} \delta x_i \tag{2}$$

Eqn. (B2) can be normalized by *R* to obtain:

$$\frac{\delta R_i}{R} = \frac{1}{R} \frac{\partial R}{\partial x_i} \delta x_i \tag{3}$$

where ∂*R* / ∂*xi* are the sensitivity coefficients. Eqn. (B3) can be re-written as follows:

$$\frac{\delta R_i}{R} = \frac{x_i}{R} \frac{\partial R}{\partial x_i} \frac{\delta x_i}{x_i} \tag{4}$$

Appendix B

The estimation of the uncertainty interval in the experimental result due to any variation in *xi* can be obtained using eqn. (4) as follows:

$$\frac{U_{R_i}}{R} = \frac{x_i}{R}\frac{\partial R}{\partial x_i}\frac{U_{x_i}}{x_i} \tag{5}$$

Applying Taylor's expansion to eqn. (B5) yields

$$\frac{U_R}{R} = \left[\left(\frac{x_1}{R}\frac{\partial R}{\partial x_1}\frac{U_{x_1}}{x_1}\right)^2 + \left(\frac{x_2}{R}\frac{\partial R}{\partial x_2}\frac{U_{x_2}}{x_2}\right)^2 + \cdots + \left(\frac{x_n}{R}\frac{\partial R}{\partial x_n}\frac{U_{x_n}}{x_n}\right)^2\right]^{1/2} \tag{6}$$

For a measured variable, *xi*, the uncertainty estimate is given by

$$U_{x_i} = \left(B_{x_i}^2 + P_{x_i}^2\right)^{\frac{1}{2}} \tag{7}$$

B.2 Uncertainty estimate in the free-stream velocity

In order to estimate the 95% precision and bias confidence limits, the procedure given by Coleman and Steele (1999) was adopted. The uncertainty estimate in the free-stream velocity is determined from its data reduction equation as follows:

$$U_e = \sqrt{\frac{2\Delta P}{\rho}} \tag{8}$$

where D*P* is the dynamic pressure and r is the air density. The bias and precision errors of the dynamics pressure were given by the manufacturer in the pressure transducer manual as follows: $B_{\Delta p}^2$ = 0.30 % and $P_{\Delta p}^2$ = 0.95 %. The uncertainty estimate is the dynamic pressure is

$$U_{\Delta P}^c = (B_{\Delta P}^2 + P_{\Delta P}^2)^{\frac{1}{2}} = \pm 1.25\% \tag{9}$$

Assuming the equation of state of an ideal gas holds for the measurement conditions, and then the air density can be determined as

$$\rho = \frac{Pa}{RT} \tag{10}$$

where *Pa* is the absolute pressure, *R* is the gas constant, and *T* is the temperature. The uncertainty estimate in the air density is calculated from

$$\frac{U_\rho}{\rho} = \left(\left(\frac{U_{Pa}}{Pa}\right)^2 + \left(\frac{U_T}{T}\right)^2\right)^{1/2} \tag{11}$$

Appendix B

The uncertainty estimates in the absolute pressure and temperature are ±0.01 % and ±0.33 %, respectively. The uncertainty estimate in air density is

$$\frac{U_\rho}{\rho} = (0.01^2 + 0.33^2)^{1/2} = \pm 0.33\% \quad (12)$$

Using the values of the uncertainty estimates for the dynamic pressure and air density, the uncertainty estimate in *Ue* becomes

$$\frac{U_{U_e}^c}{U_e} = \left(\left(\frac{1}{2}\frac{U_{\Delta p}^c}{\Delta P}\right)^2 + \left(\frac{1}{2}\frac{U_\rho^c}{\rho}\right)^2\right)^{1/2} = \pm 1.5\% \quad (13)$$

Appendix C

Shear stress distributions

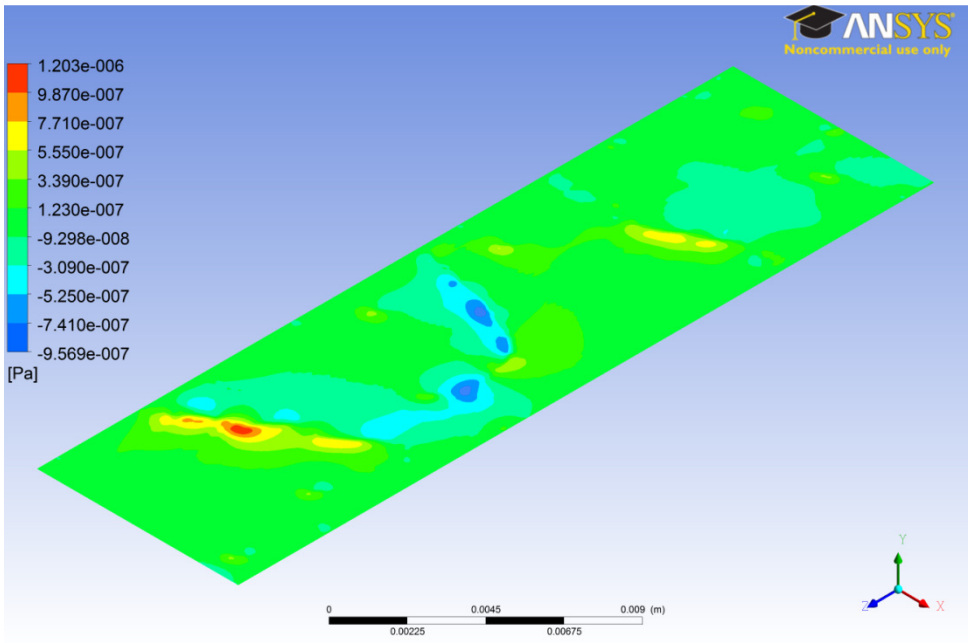

Figure 1: Shear stress distribution on span-wise direction for flat plate

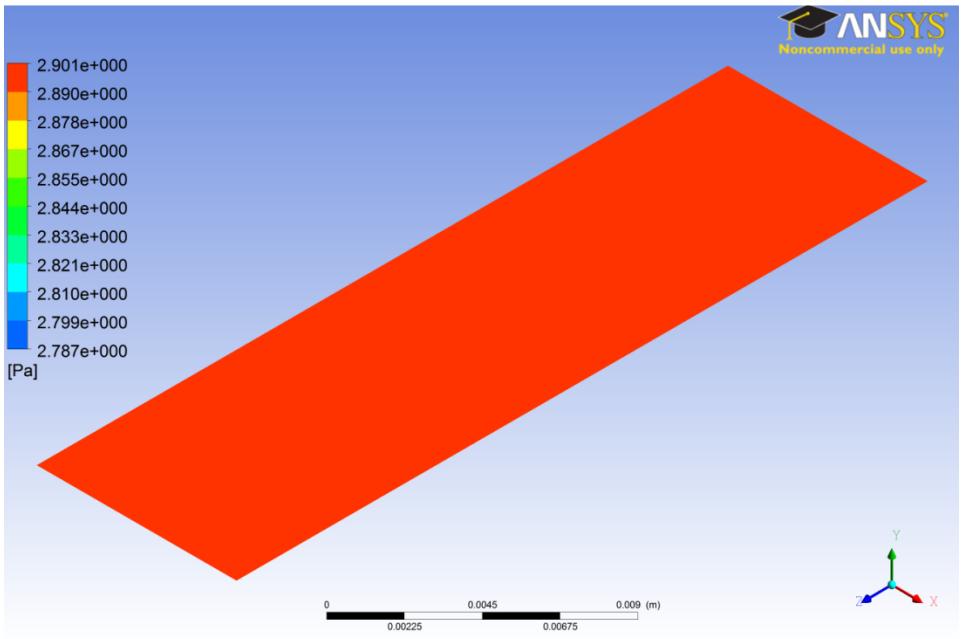

Figure 2: Shear stress distribution on stream-wise direction for flat plate

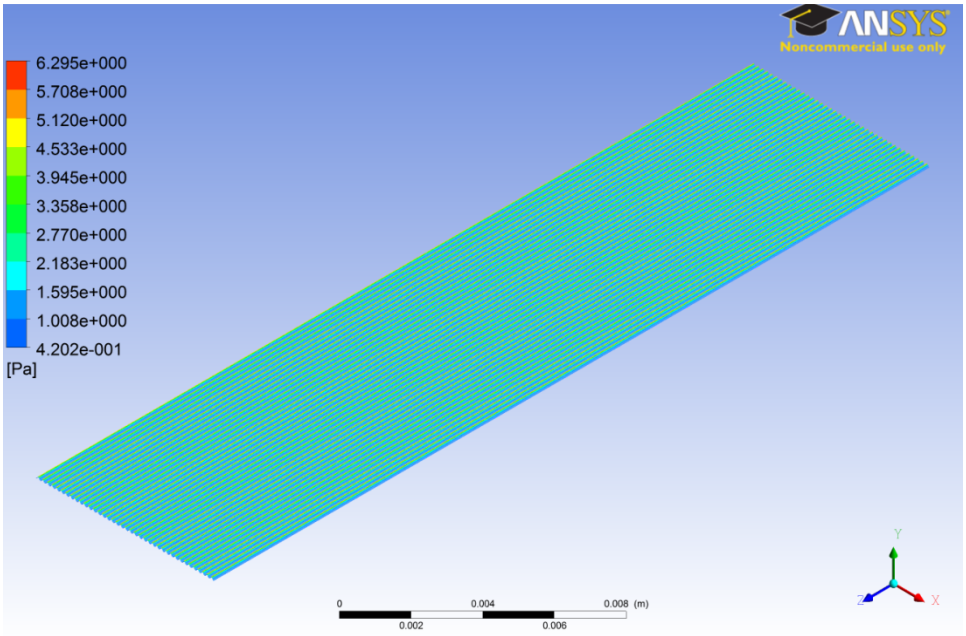

Figure 3: Shear stress distribution for M.5

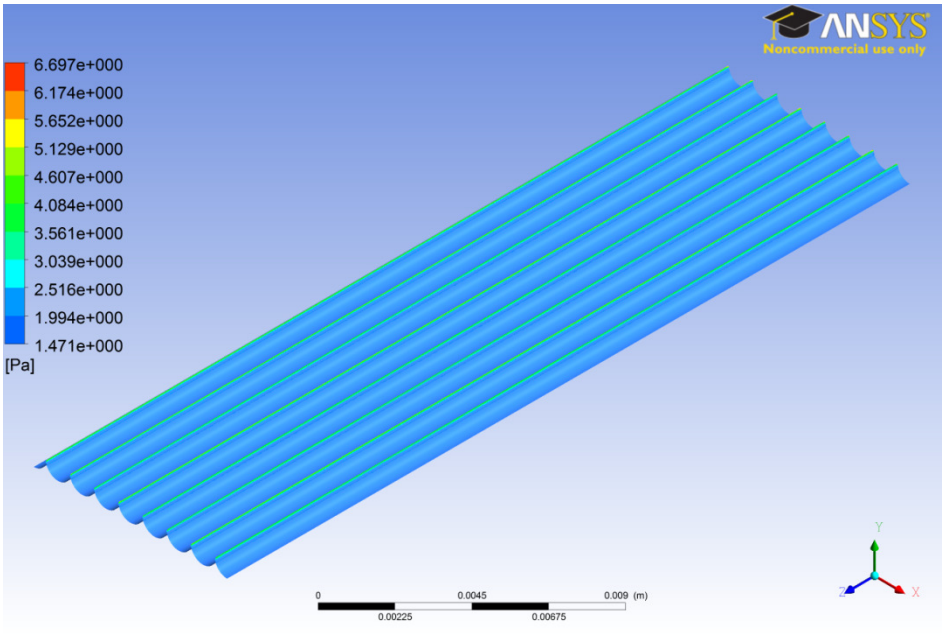

Figure 4: Shear stress distribution for M.3

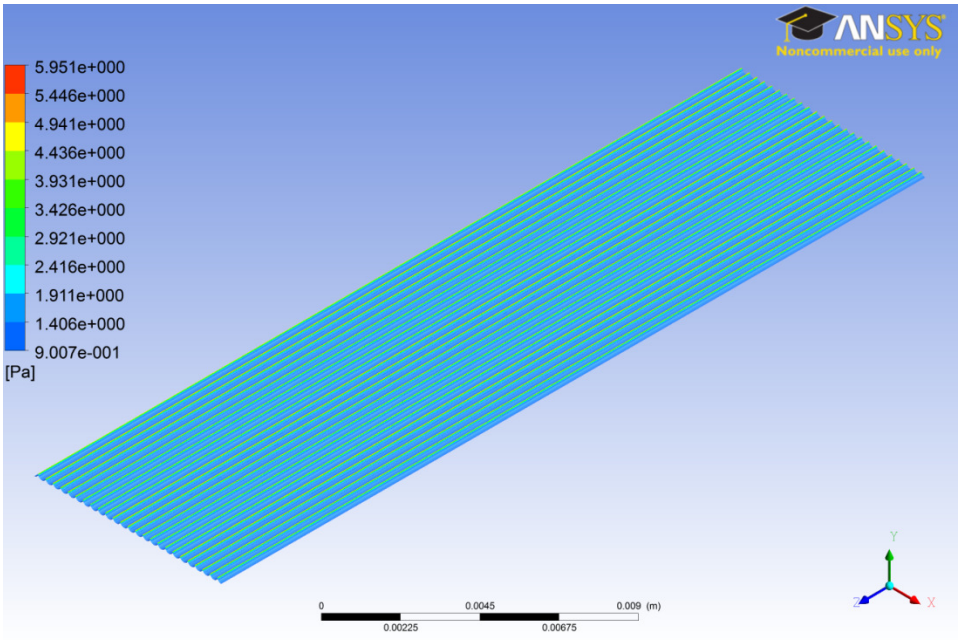

Figure 5: Shear stress distribution for M.1

Appendix D

Surface measurments and CAD design

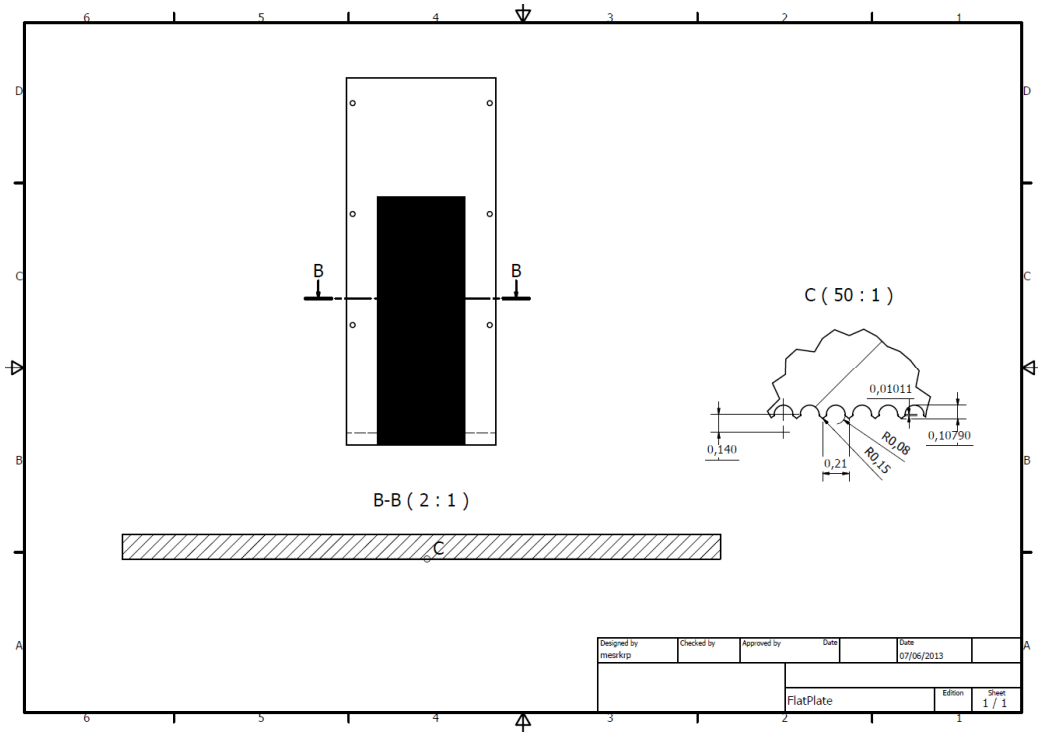

Figure 1: 3D CAD design of riblet's plate

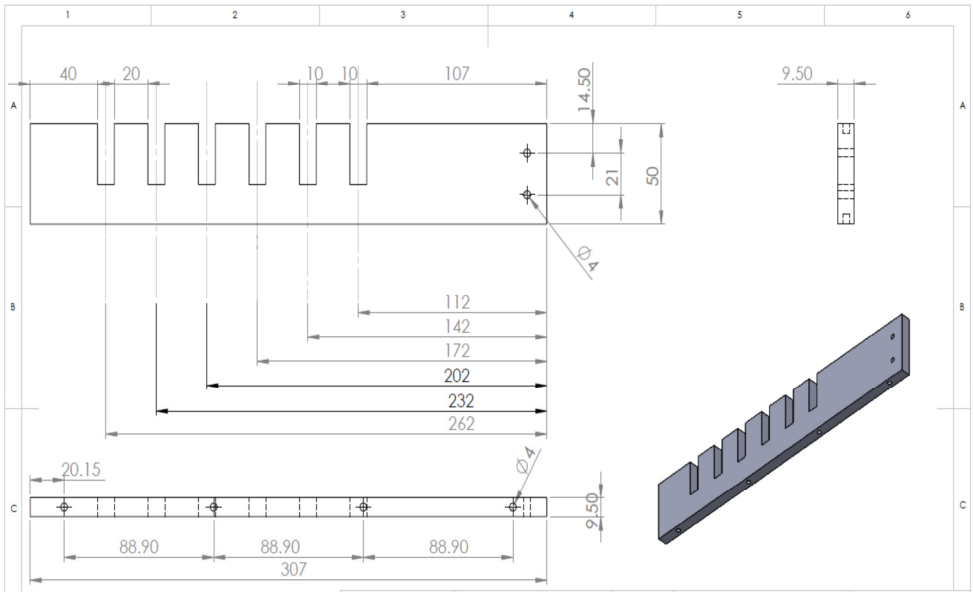

Figure 2: 3D CAD design of side wall for workbench

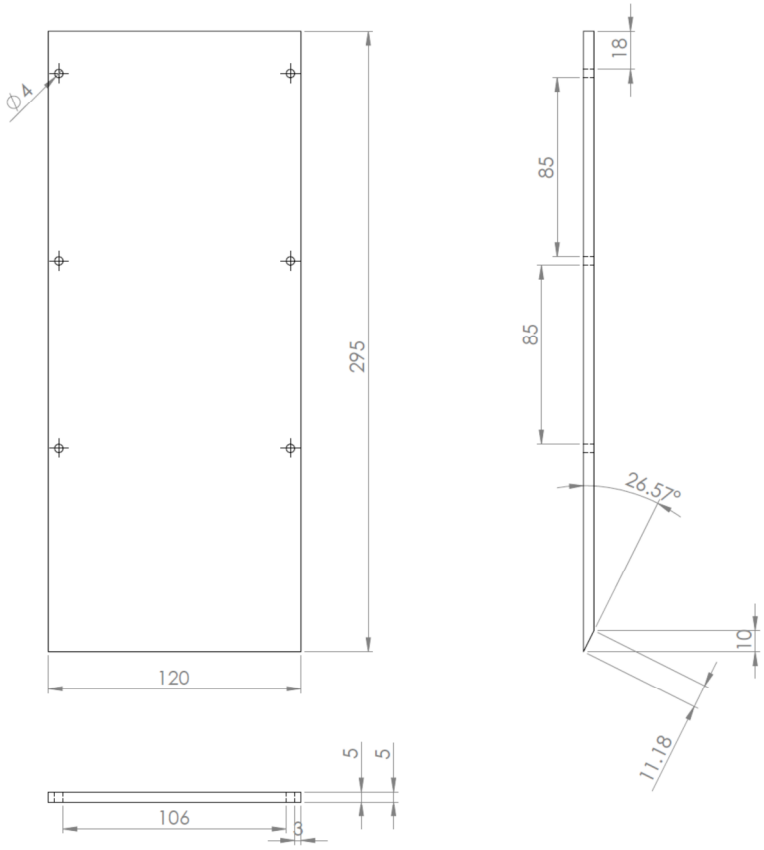

Figure 3: 3D CAD design of flat plate

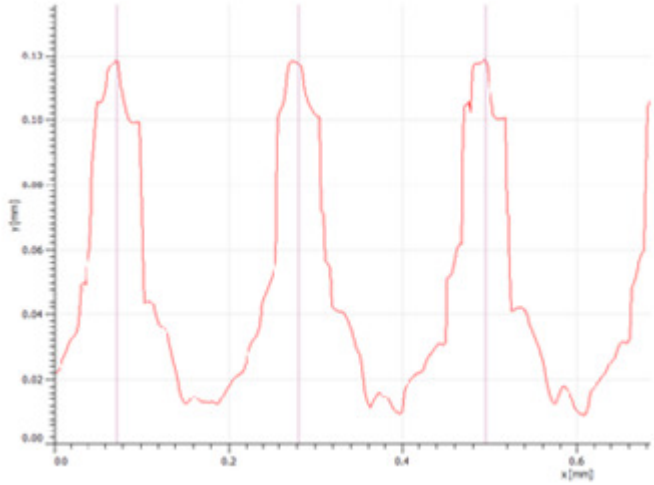

Figure 4: Profile of machined riblets as measured with Alicona

Appendix D

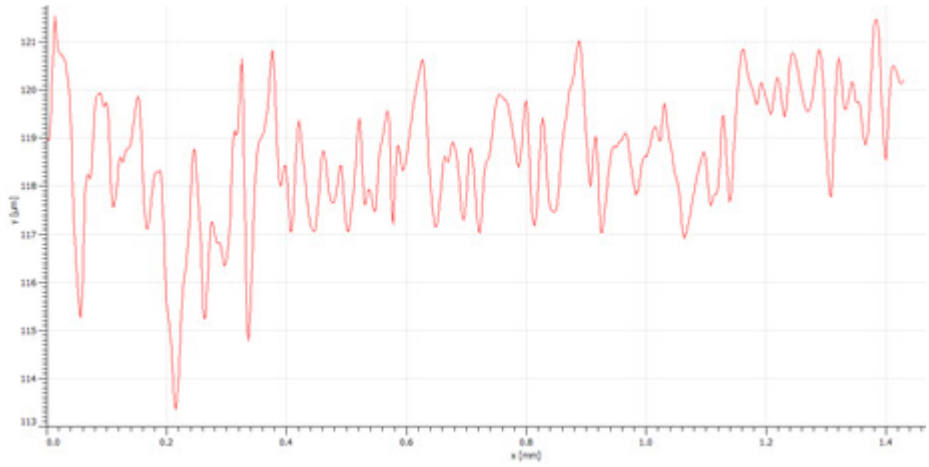

Figure 5: Riblets profile along groove bottom as measured with Alicona

	Amplitude	
R_a	Roughness average	1.0 µm
R_q	Root mean square roughness	1.3 µm
R_t	Maximum height of the roughness	8.2 µm
R_v	Maximum roughness valley depth	5.4 µm
R_p	Maximum roughness peak height	2.8 µm
R_{tm}	Average maximum height of the roughness	5.1 µm
R_{vm}	Average maximum roughness valley depth	2.7 µm
R_{pm}	Average maximum roughness peak height	2.4 µm
R_{3z}	Average third highest peak to third lowest valley height	5.8 µm
$R_{3z\ ISO}$	Average third highest peak to third lowest valley height	2.7 µm
R_z	Average maximum height of the profile	4.8 µm
$R_{z\ ISO}$	Average maximum height of the roughness	5.1 µm
R_{sk}	Skewness	-0.835
R_{ku}	Kurtosis	4.144
W_a	Waviness average	118.7 µm
W_q	Root mean square waviness	118.7 µm
$W_y=W_{max}$	Waviness maximum height	118.7 µm
P_t	Maximum height of the profile	121.5 µm

Figure 6: Measurement characteristics from 3D riblets profile as measured with Alicona

Appendix E

Velocity profiles

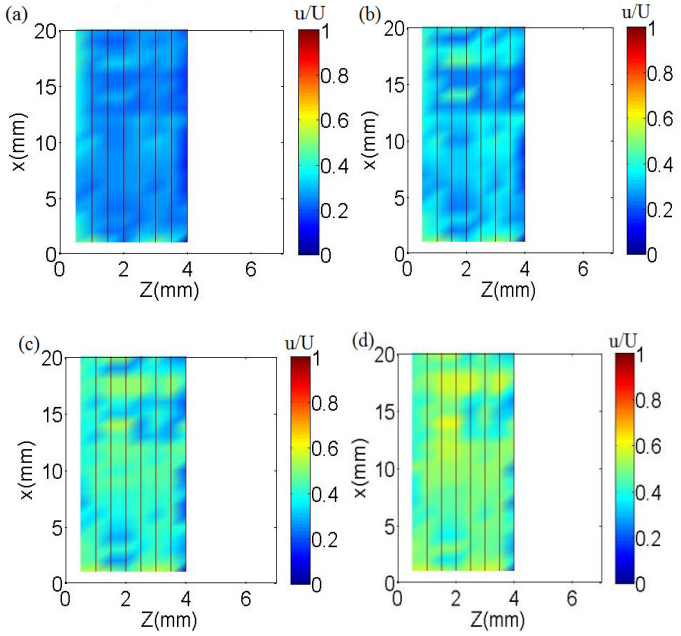

Figure 1: Boundary layer mean velocity profiles contour plots normal to the plate over the smooth surface (U_m), X: stream-wise (25 positions) and Z: span-wise (13 positions), a) y=0.1mm b) y=0.15mm c) y=0.2mm d) y=0.3mm

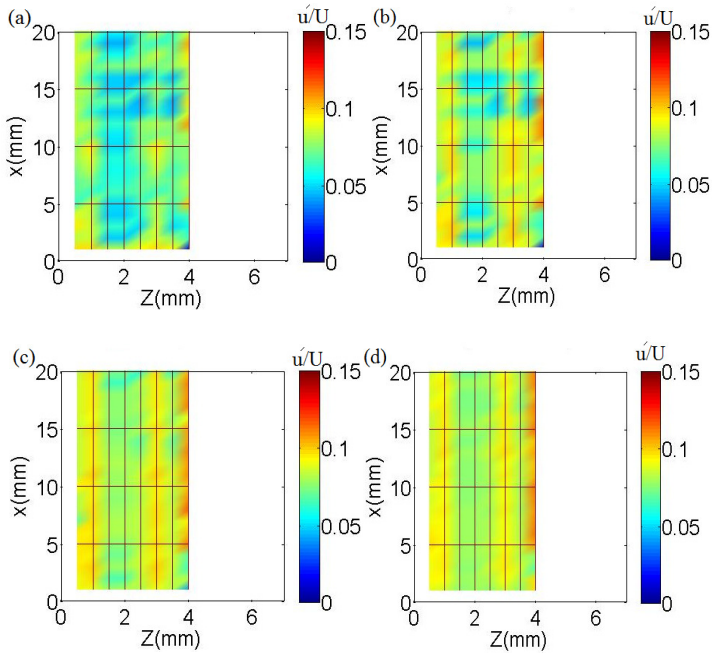

Figure 2: Boundary layer root-mean-square velocity profiles contour plots normal to the plate over the smooth surface (U_{rms}), X: stream-wise (25 positions) and Z: span-wise (13 positions), a) y=0.1mm b) y=0.15mm c) y=0.2mm d) y=0.3mm

Appendix E

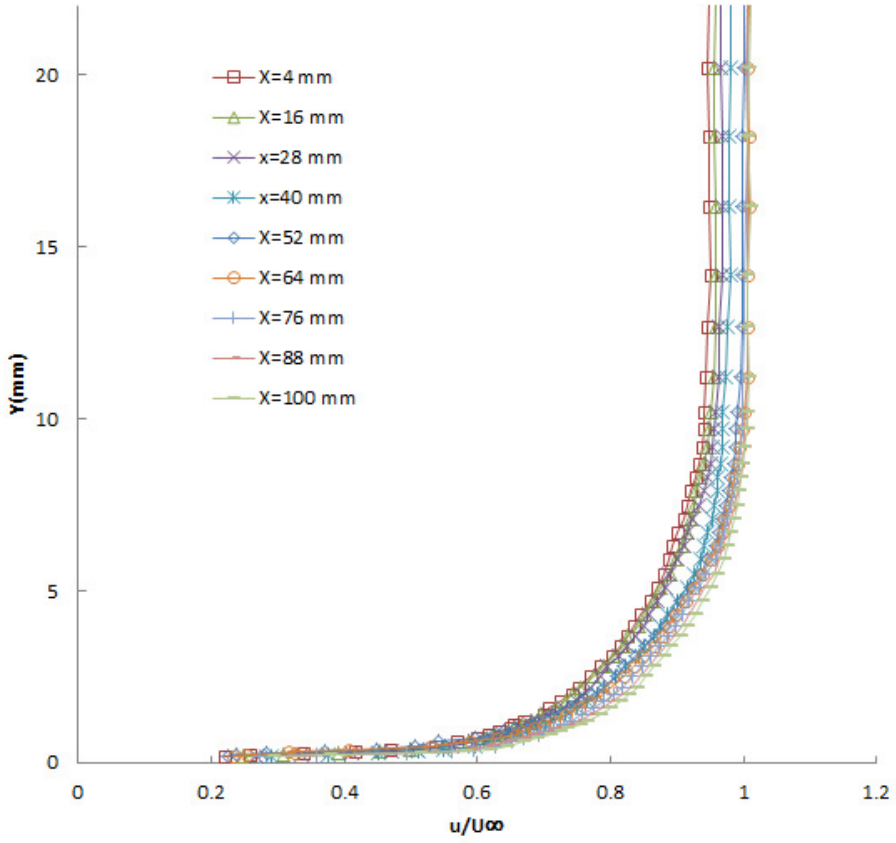

Figure 3: Boundary layer mean velocity profiles at nine different stream-wise positions in one span-wise position over the smooth surface

Appendix F

MATLAB programming for experimental data analysis

F.1 Single hot wire analysis:

F.1.1 Data reduction:

```
COR1=((190-19.5)/(190-22)).^(0.5); %Temperature Correction; Insert
Values of (Tw-Tcalib)/(Tw-Tacquisition)
    A=1.1167;          % Variables for polynomial function
    B=-9.271;
    C=31.814;
    D=-52.358;
    E=33.62;
    %data reduction
for i = 1:93
    if i < 10
        data1=load(strcat('RIBSP3.B000',num2str(i)))*COR1;
    elseif i < 100
        data1=load(strcat('RIBSP3.B00',num2str(i)))*COR1;
    elseif i < 1000
        data1=load(strcat('RIBSP3.B0',num2str(i)))*COR1;
    end
    u=A.*data1(:,2).^4  +  B.*data1(:,2).^3  +  C.*data1(:,2).^2  +
D.*data1(:,2)+ E;
 Volmean(i)=mean(data1(:,2));
 Umean(i)=mean(u);
 Urms(i)=std(u);
end
save VolmeanRIB232.txt Volmean -ascii -tabs -double;
Sz=horzcat(Umean',Urms')
save RIB232.txt Sz -ascii -tabs -double;

%-----------------------------------------------------------------------

clc
close all
clear all
Q=46 %boundary profile length
load RIB232.txt
S= RIB232
num_of_files=ceil(length(S)/(Q+1))
for i=0:num_of_files
    if i<10
count=i+1;
y=num2str(count)
z=strcat('RIBooo',y)
```

```
final=strcat(z,'.txt')
al=S((1+i)+Q*i:i+Q*(i+1),:);
save(final,'al','-ASCII')
figure;
plot(al)
     elseif i < 20
count=i+1;
y=num2str(count)
z=strcat('RIBoo',y)
final=strcat(z,'.txt')
al=S((i)+Q*i:i-1+Q*(i+1),:);
save(final,'al','-ASCII')
figure;
plot(al)

    else
count=i+1;
y=num2str(count)
z=strcat('RIBoo',y)
final=strcat(z,'.txt')
al=S((i-1)+Q*i:i-2+Q*(i+1),:);
save(final,'al','-ASCII')
figure;
plot(al)
    end
end
```

F.1.2 Mean velocity and root-mean-square velocity:

```
function xzcontour_plot6(serration1,serration2,y)
    serration1 = 1;
    length1 = 8;
    width1 = 20;
    dx1=1;
    dz1=1;
for i = 1 : length1
    for j = 1 : width1
        if j <10
umean_temp=load(strcat('S',num2str(serration1),'Po',num2str(i),'o'
,num2str(j),'.txt'))';
        else
umean_temp=load(strcat('S',num2str(serration1),'Po',num2str(i),num
2str(j),'.txt'))';
        end
        umean1(i,j)=umean_temp(1,y);
        Umean1(i,j)=umean1(i,j)/umean_temp(1,mean(44:46));  %scaled
mean velocity
        urms1(i,j) =umean_temp(2,y);
        Urms1(i,j)           =urms1(i,j)/umean_temp(1,mean(44:46));
%turbulence intensity
        z1(j)= dz1*j;
    end
    x1(i)= dx1*i;
end
[X1 Z1] = meshgrid(x1,z1);

%figure 1 is to plot and compare the umean
figure;
```

```
pcolor(X1,Z1,Umean1')
shading interp
caxis([0 1])
set(gca,'plotboxaspectratio',[1 1 1],'fontsize',20)
title(sprintf('u_m at y = %0.3g',y))
caxis([0 1])
axis([0 20 0 20])
colorbar
hold
contour(X1,Z1,X1)
ser_geo=-4.71*x1+18.84;
plot (ser_geo,'k-','linewidth',2);
ser_geo2=4.71*x1-18.84;
plot (ser_geo2,'k-','linewidth',2);

%figure 2 is to plot and compare the urms
figure;
pcolor(X1,Z1,Urms1')
shading interp
set(gca,'plotboxaspectratio',[1 1 1],'fontsize',20)
title(sprintf('u_{rms} at y = %0.3g',y))
caxis([0 0.15])
colorbar
hold
contour(X1,Z1,Z1)
contour(X1,Z1,X1)
axis([1 20 0 20])
plot (ser_geo,'k-','linewidth',2);
plot (ser_geo2,'k-','linewidth',2);
```

F.1.3 Skin Friction:

```
for i=1:2:48
figure (1)
semilogx(M02(:,i), M02(:,i+1)) %clauser curves from xlx
hold all
end
Ufs=mean(FP1Po925(42:45,1));%type in file name
Yc=((Y+0.05)/1000)*Ufs/(1.49*(10^(-5)))
Curve=FP1Po925/Ufs %type in file name
figure (2)
semilogx((Yc),Curve)
```

F.2 Cross correlation:

```
%input parameters
num = 46;                              %number of sampled files
Fs = 40049;                             %sampling frequency
prms_lim = 1.5;                               %threshold factor for +/-
pressure peaks
resolution = 4;                          %resolution of +/- peaks to be
averaged
I = 72;                                   %number of points at one side
of the surface pressure peak
Npt4Uo = 46;                             %choose which experiment point
to represent the freestream value
nfft=1024*4;                            %number of points in FFT
```

Appendix F

```
choice = 1;
load('y.txt')
name = 'FPXM8A1';
    f_temp = load(strcat(name,'_46.txt'));
    Uinf = mean(f_temp(:,1)); clear f_temp
        for iTrv = 1 : num
            iTrv
            f = load(strcat(name,'_',num2str(iTrv),'.txt'));

            %-------------------------------------------------
            %locate +/- surface pressure peaks
            prms(iTrv) = std(f(:,3));
            plus_prms  = prms_lim * prms(iTrv);
            minus_prms = -plus_prms;
            %find  pressure  data  that  exceed  the  +/-  Prms
thresholds
            plus_value  = find(f(:,3) >= plus_prms);
            minus_value = find(f(:,3) <= minus_prms);
            %find the start and end of plus_value and minus_value
            m = 1;
            for i = 2:length(plus_value)
                if plus_value(i) - plus_value(i-1) > 2
                    plus_start(m+1) = plus_value(i);
                    plus_end(m)     = plus_value(i-1);
                    m = m + 1;
                end
            end
            n = 1;
            for j = 2:length(minus_value)
                if abs(minus_value(j) - minus_value(j-1)) > 2
                    minus_start(n+1) = minus_value(j);
                    minus_end(n)     = minus_value(j-1);
                    n = n + 1;
                end
            end
            %re-arrange start and end of +/- values
            positive_temp(:,1)  =  plus_start(3:length(plus_start)-
3);
            positive_temp(:,2) = plus_end(3:length(plus_end)-2);
            negative_temp(:,1)                                    =
minus_start(4:length(minus_start)-3);
            negative_temp(:,2) = minus_end(4:length(minus_end)-2);
            %de-select +/- values with low resolutions and locate
the +/- peaks
            k = 1;
            for i = 1:length(positive_temp)
                if  positive_temp(i,2)  -  positive_temp(i,1)  >
resolution
                    positive(k,1) = positive_temp(i,1);
                    positive(k,2) = positive_temp(i,2);
                    xx(positive(k,1):positive(k,2))               =
f(positive(k,1):positive(k,2),3);
                    peak          =          find(xx          ==
max(f(positive(k,1):positive(k,2),3)));
                    plus_peak(k) = peak(1);
                    clear xx
                    dx1(k) = plus_peak(k) - positive(k,1);
                    dx2(k) = positive(k,2) - plus_peak(k);
                    k = k + 1;
                end
            end
```

```
            l = 1;
            for j = 1:length(negative_temp)
                if   negative_temp(j,2)   -   negative_temp(j,1)   >
resolution
                    negative(l,1) = negative_temp(j,1);
                    negative(l,2) = negative_temp(j,2);
                    yy(negative(l,1):negative(l,2))               =
f(negative(l,1):negative(l,2),3);
                    peak          =          find(yy          ==
min(f(negative(l,1):negative(l,2),3)));
                    minus_peak(l) = peak(1);
                    clear yy
                    dy1(l) = minus_peak(l) - negative(l,1);
                    dy2(l) = negative(l,2) - minus_peak(l);
                    l = l + 1;
                end
            end
            clear positive_temp negative_temp plus_start plus_end
minus_start minus_end
            clear positive negative xx yy

            % ---------------------------------------------
            U = f(:,1);     U_bar(iTrv) = mean(U); U_rms(iTrv) =
std(U);
            V = -f(:,2);    V_bar(iTrv) = mean(V); V_rms(iTrv) =
std(V);
            P = f(:,3);
            clear f
            plus_P_peak(1:length(plus_peak))   = P(plus_peak(:));
            plus_U_peak(1:length(plus_peak))   = U(plus_peak(:));
            plus_V_peak(1:length(plus_peak))   = V(plus_peak(:));
            minus_P_peak(1:length(minus_peak)) = P(minus_peak(:));
            minus_U_peak(1:length(minus_peak)) = U(minus_peak(:));
            minus_V_peak(1:length(minus_peak)) = V(minus_peak(:));
            plus_P(1:length(plus_peak),I+1)   = plus_P_peak;
            plus_U(1:length(plus_peak),I+1)   = plus_U_peak;
            plus_V(1:length(plus_peak),I+1)   = plus_V_peak;
            minus_P(1:length(minus_peak),I+1) = minus_P_peak;
            minus_U(1:length(minus_peak),I+1) = minus_U_peak;
            minus_V(1:length(minus_peak),I+1) = minus_V_peak;
            if plus_peak(1) <= I
                plus_peak(1)=plus_peak(2);
            elseif minus_peak(1) <= I
                minus_peak(1)=minus_peak(2);
            elseif plus_peak(end)+I > length(P)
                plus_peak(end)=plus_peak(end-1);
            elseif minus_peak(end)+I > length(P)
                minus_peak(end)=minus_peak(end-1);
            end
            for i = 1 : I
                plus_P(1:length(plus_peak),I-i+1)    = P(plus_peak-
i);
                plus_P(1:length(plus_peak),I+i+1)                 =
P(plus_peak+i);
                plus_U(1:length(plus_peak),I-i+1)    = U(plus_peak-
i);
                plus_U(1:length(plus_peak),I+i+1)                 =
U(plus_peak+i);
                plus_V(1:length(plus_peak),I-i+1)    = V(plus_peak-
i);
```

```
                plus_V(1:length(plus_peak),I+i+1)                =
V(plus_peak+i);
                minus_P(1:length(minus_peak),I-i+1)              =
P(minus_peak-i);
                minus_P(1:length(minus_peak),I+i+1)              =
P(minus_peak+i);
                minus_U(1:length(minus_peak),I-i+1)              =
U(minus_peak-i);
                minus_U(1:length(minus_peak),I+i+1)              =
U(minus_peak+i);
                minus_V(1:length(minus_peak),I-i+1)              =
V(minus_peak-i);
                minus_V(1:length(minus_peak),I+i+1)              =
V(minus_peak+i);
            end
            %calculate   the   ensamble-averaged   +/-   velocities
relatives to the +/- pressure peaks
            P_plus(iTrv,:)  = mean(plus_P);
            U_plus(iTrv,:)  = mean(plus_U);
            V_plus(iTrv,:)  = mean(plus_V);
            P_minus(iTrv,:) = mean(minus_P);
            U_minus(iTrv,:) = mean(minus_U);
            V_minus(iTrv,:) = mean(minus_V);
            %calculate the rms velocity fluctuations and Reynolds
stress relative to the +/- pressure peaks
            for i = 1 : length(plus_U)
                p_plus(i,:)            =      ((plus_P(i,:)      -
P_plus(iTrv,:)).^2);
                u_plus(i,:)            =      ((plus_U(i,:)      -
U_plus(iTrv,:)).^2);
                uu_plus(i,:) = plus_U(i,:) - U_plus(iTrv,:);
                u8_plus(i,:) = plus_U(i,:) - 0.8*Uinf;
                u6_plus(i,:) = plus_U(i,:) - 0.6*Uinf;
                u4_plus(i,:) = plus_U(i,:) - 0.4*Uinf;
                v_plus(i,:)            =      ((plus_V(i,:)      -
V_plus(iTrv,:)).^2);
                vv_plus(i,:) = plus_V(i,:) - V_plus(iTrv,:);
                v8_plus(i,:) = plus_V(i,:) - 0.8*Uinf;
                v6_plus(i,:) = plus_V(i,:) - 0.6*Uinf;
                v4_plus(i,:) = plus_V(i,:) - 0.4*Uinf;
                uv_plus(i,:)        =        (plus_U(i,:)       -
U_plus(iTrv,:)).*(plus_V(i,:) - V_plus(iTrv,:));
            end
            for i = 1 : length(minus_U)
                p_minus(i,:)           =      ((minus_P(i,:)     -
P_minus(iTrv,:)).^2);
                u_minus(i,:)           =      ((minus_U(i,:)     -
U_minus(iTrv,:)).^2);
                uu_minus(i,:) = minus_U(i,:) - U_minus(iTrv,:);
                u8_minus(i,:) = minus_U(i,:) - 0.8*Uinf;
                u6_minus(i,:) = minus_U(i,:) - 0.6*Uinf;
                u4_minus(i,:) = minus_U(i,:) - 0.4*Uinf;
                v_minus(i,:)           =      ((minus_V(i,:)     -
V_minus(iTrv,:)).^2);
                vv_minus(i,:) = minus_V(i,:) - V_minus(iTrv,:);
                v8_minus(i,:) = minus_V(i,:) - 0.8*Uinf;
                v6_minus(i,:) = minus_V(i,:) - 0.6*Uinf;
                v4_minus(i,:) = minus_V(i,:) - 0.4*Uinf;
                uv_minus(i,:)       =       (minus_U(i,:)      -
U_minus(iTrv,:)).*(minus_V(i,:) - V_minus(iTrv,:));
            end
```

```
            prms_plus(iTrv,:)    = sqrt(mean(p_plus));
            urms_plus(iTrv,:)    = sqrt(mean(u_plus));
            uprime_plus(iTrv,:)                                    =
mean(uu_plus);u8prime_plus(iTrv,:)=mean(u8_plus);u6prime_plus(iTrv
,:)=mean(u6_plus);u4prime_plus(iTrv,:)=mean(u4_plus);
            vrms_plus(iTrv,:)    = sqrt(mean(v_plus));
            vprime_plus(iTrv,:)                                    =
mean(vv_plus);v8prime_plus(iTrv,:)=mean(v8_plus);v6prime_plus(iTrv
,:)=mean(v6_plus);v4prime_plus(iTrv,:)=mean(v4_plus);
            uvmean_plus(iTrv,:)  = mean(uv_plus);
            prms_minus(iTrv,:)   = sqrt(mean(p_minus));
            urms_minus(iTrv,:)   = sqrt(mean(u_minus));
            uprime_minus(iTrv,:)                                   =
mean(uu_minus);u8prime_minus(iTrv,:)=mean(u8_minus);u6prime_minus(
iTrv,:)=mean(u6_minus);u4prime_minus(iTrv,:)=mean(u4_minus);
            vrms_minus(iTrv,:)   = sqrt(mean(v_minus));
            vprime_minus(iTrv,:)                                   =
mean(vv_minus);v8prime_minus(iTrv,:)=mean(v8_minus);v6prime_minus(
iTrv,:)=mean(v6_minus);v4prime_minus(iTrv,:)=mean(v4_minus);
            uvmean_minus(iTrv,:) = mean(uv_minus);
            clear positive_temp negative_temp plus_start plus_end
minus_start minus_end positive negative
            clear plus_P_peak plus_U_peak plus_V_peak minus_P_peak
minus_U_peak minus_V_peak
            clear plus_U plus_V plus_P minus_U minus_V minus_P
u_plus v_plus p_plus u_minus v_minus p_minus
            clear plus_peak minus_peak plus_value minus_value
uv_plus uv_minus
            clear Npt4Uo Patm Tatm R rho_h20 g
            clear uu_plus u8_plus u6_plus u4_plus uu_minus
u8_minus u6_minus u4_minus
            clear vv_plus v8_plus v6_plus v4_plus vv_minus
v8_minus v6_minus v4_minus
        end
        save(sprintf(strcat('Conditioned2_uvp_',name,'.mat')))

%-----------------------------------------------------------------

close all
fP = 56;          %fP is needed when the chosen fN are spectra,
xcorr, conditioned_uvp and quadrant
Fs = 40049;                          %sampling frequency
Npt4Uo = 46;
%choose which experimental point to represent the freestream valu
%(Npt4Uo=46 for both single and cross wire)
fname_smooth  =  'Conditioned_uvp_FPXM8B';  %THE  FILENAME  TO  THE
SMOOTH ONE
fname_rib      =  'Conditioned_uvp_RIBXM8B';  %THE  FILENAME  TO  THE
RIBLET ONE
Npt4bl=1;

%-----------------------------------------------------------------

     load(strcat(fname_rib,'.mat'))
     [a b] = size(P_plus);
       V=-V;
       urms_plus_P           =           urms_plus./U_bar(Npt4Uo);
urms_minus_P = urms_minus./U_bar(Npt4Uo);
       vrms_plus_P           =           vrms_plus./U_bar(Npt4Uo);
vrms_minus_P = vrms_minus./U_bar(Npt4Uo);
```

```
          U_plus_P             =             U_plus./U_bar(Npt4Uo);
U_minus_P = U_minus./U_bar(Npt4Uo);
          V_plus_P             =             V_plus./U_bar(Npt4Uo);
V_minus_P = V_minus./U_bar(Npt4Uo);
          for i = 1 : length(U_plus_P)
              for j = 1 : 46
                  UP_pert_P(j,i)           =           (U_plus(j,i)-
U_bar(j))/U_bar(Npt4Uo);
                  VP_pert_P(j,i)           =           (V_plus(j,i)-
V_bar(j))/U_bar(Npt4Uo);
                  UM_pert_P(j,i)          =          (U_minus(j,i)-
U_bar(j))/U_bar(Npt4Uo);
                  VM_pert_P(j,i)          =          (V_minus(j,i)-
V_bar(j))/U_bar(Npt4Uo);
              end
          end
     uvmean_plus_P      =      uvmean_plus./U_bar(Npt4Uo)^2      ;
uvmean_minus_P = uvmean_minus./U_bar(Npt4Uo)^2;
     t = 0 : 1/Fs : (length(P)-1)/Fs;
         dt_P(I : -1 : 1)  = -t(2:I+1)*1000;
         dt_P(I+1 : 2*I+1) = t(1:I+1)*1000;
         y_del_star_P = y;
     [dT_P Y_P]   = meshgrid(dt_P,y_del_star_P);

%-----------------------------------------------------------------

     load(strcat(fname_smooth,'.mat'))
     [a b] = size(P_plus);
     %      y_temp=load('y.txt');
          V=-V;
       urms_plus_F            =            urms_plus./U_bar(Npt4Uo);
urms_minus_F = urms_minus./U_bar(Npt4Uo);
       vrms_plus_F            =            vrms_plus./U_bar(Npt4Uo);
vrms_minus_F = vrms_minus./U_bar(Npt4Uo);
          U_plus_F             =             U_plus./U_bar(Npt4Uo);
U_minus_F = U_minus./U_bar(Npt4Uo);
          V_plus_F             =             V_plus./U_bar(Npt4Uo);
V_minus_F = V_minus./U_bar(Npt4Uo);
       for i = 1 : length(U_plus_P)
          for j = 1 : 46
              UP_pert_F(j,i)            =            (U_plus(j,i)-
U_bar(j))/U_bar(Npt4Uo);
              VP_pert_F(j,i)            =            (V_plus(j,i)-
V_bar(j))/U_bar(Npt4Uo);
              UM_pert_F(j,i)           =           (U_minus(j,i)-
U_bar(j))/U_bar(Npt4Uo);
              VM_pert_F(j,i)           =           (V_minus(j,i)-
V_bar(j))/U_bar(Npt4Uo);
          end
       end
     uvmean_plus_F      =      uvmean_plus./U_bar(Npt4Uo)^2      ;
uvmean_minus_F = uvmean_minus./U_bar(Npt4Uo)^2;
         dt_F(I : -1 : 1)  = -t(2:I+1)*1000;
         dt_F(I+1 : 2*I+1) = t(1:I+1)*1000;
         y_del_star_F = y;
     [dT_F Y_F]   = meshgrid(dt_F,y_del_star_F);
         a = 0; b = 10;
         iXlabel = '\Deltat (ms)';
         iYlabel = 'y (mm)';
     aa = 1;  bb = 1;  cc = 1;
     iurms_a = 0.06;  iurms_b = 0.08;
```

```
     ivrms_a = 0.04;  ivrms_b = 0.06;
     iU_a    = 0.55;  iU_b    = 1;
     iV_a    = -0.05; iV_b    = 0.01;
     iuv_a   = 0;     iuv_b   = 1.5*10^-3;
     iuper_a_pp = 0;          iuper_b_pp = 0.08;       iuper_a_pm =
-0.08;     iuper_b_pm = 0;
     ivper_a_pp = -16/1000;  ivper_b_pp = 0;          ivper_a_pm =
0;         ivper_b_pm = 16/1000;
     iN = 'jet';
     iBright = 0;
     figure
subplot(221),pcolor(dT_P,Y_P,urms_plus_P(Npt4bl:Npt4Uo,:));shading
interp,hold on
     title(sprintf('Riblet:u_{rms}/U_o       corresponds       to
+P'),'fontsize',16),colorbar,set(gca,'fontsize',14,'linewidth',2,'
plotboxaspectratio',[aa bb cc])
     ylim([a b])
     xlabel(iXlabel,'fontsize',16),ylabel(iYlabel,'fontsize',16)
     caxis([iurms_a iurms_b])
     colormap(iN), brighten(iBright)
```

F.3 Microphones (Wall pressure):

```
function analyse_all_draft
    Fs   = 40049;
    nfft = 1024*2;
    fname= 'FMSTRG.B0001';
    f = load(fname);
    A = f(:,2);
    B = f(:,3);
    for k = 1 : 1
        [Pxx(:,k),F] = pwelch(A,hamming(nfft),[],nfft,Fs);
        [Pyy(:,k),F] = pwelch(B,hamming(nfft),[],nfft,Fs);
        [Pxy(:,k),F] = cpsd(A,B,hamming(nfft),[],nfft,Fs);
        H1(:,k) = Pxy(:,k)./Pxx(:,k);
        H2(:,k) = Pyy(:,k)./Pxy(:,k);
        Hv(:,k)                                                    =
1./(Pxy(:,k)./abs(Pxy(:,k)).*sqrt(Pyy(:,k)./Pxx(:,k)));
        Cu(:,k) = abs(H1(:,k)./H2(:,k));
        figure(k)
        subplot(221),semilogx(F,10*log10(Pxx(:,k))),xlim([100
10000]),xlabel('Frequency,  Hz'),title('power  spectral  density  of
Mic A')
        subplot(222),semilogx(F,10*log10(Pyy(:,k))),xlim([100
10000]),xlabel('Frequency,  Hz'),title('power  spectral  density  of
Mic B')
        subplot(223),semilogx(F,Cu(:,k)),axis([100      10000      0
1]),xlabel('Frequency, Hz'),title('Coherence of Mics A&B')
        subplot(224),semilogx(F,angle(Hv)),axis([100    10000    -4
4]),xlabel('Frequency,          Hz'),ylabel('phase          angle,
radian'),title('Phase angle between Mics A&B')

    end
```

Appendix G

List of publications arising from this research

Journals:

Sayad Saravi, S., Cheng, K., and Chong, T. P., 2014. A simulation-based investigation on effect of serration inside riblets with the application to drag reduction. *Proceeding of the Institution of mechanical Engineering,* part G: Journal of Aerospace Engineering. (submitted)

Sayad Saravi, S., Cheng, K., Chong, T. P., and Vathylakis, A., 2014. Design of Serrate-Semi-Circular Riblets with Application to Skin Friction Reduction on Engineering Surfaces. *International Journal of Flow Control*. (submitted)

Sayad Saravi, S., Jiao, F., and Cheng, K., 2014. Design and manufacturing of ribleted surface through fly cutting on a micro-milling machine. *Proceeding of the Institution of mechanical Engineering,* part B: Journal of Engineering Manufacture. (submitted)

Sayad Saravi, S. and Cheng, K., 2013. A review of drag reduction by riblets and micro texturing in the turbulent boundary layers. *European Scientific Journal* (*ESJ)*, Vol.9 (33), pp. 62-81.

Conferences:

Vathylakis, A., Chong, T. P., Sayad Saravi, S., Cheng, K., 2014. Investigation of the broadband noise radiated from a flat plate with micro-scale surface textures. The American Institute of Aeronautics and Astronautics (*AIAA)*. (Accepted)

Sayad Saravi, S. and Cheng, K., 2012. A CFD-based investigation on boundary layer behaviour with micro ribbed and textured surfaces. Euspen Conference on Structured and Freeform Surfaces, *National Physical Laboratory (NPL)*, London, UK.